Electrochemical Carbon Dioxide Reduction for Renewable Carbonaceous Fuels and Chemicals

Xue Han

Dissertation submitted to the faculty of the Virginia Polytechnic Institute and State University in partial fulfillment of the requirements for the degree of

Doctor of Philosophy
In
Chemical Engineering

Huiyuan Zhu
Hongliang Xin
Rong Tong
Feng Lin

February 13, 2022
Blacksburg, Virginia

Nanomaterials, catalysis, electrochemistry, sustainable energy and chemical conversion

Electrochemical Carbon Dioxide Reduction for Renewable Carbonaceous Fuels and Chemicals

Xue Han

ABSTRACT

Electrochemical CO_2 reduction reaction (ECO_2RR) powered by renewable electricity possesses the potential to store intermittent energy in chemical bonds while producing sustainable chemicals and fuels. Unfortunately, it is hard to achieve low overpotential, high selectivity, and activity simultaneously of ECO_2RR. Developing efficient electrocatalysts is the most promising strategy to enhance electrocatalytic activity in CO_2 reduction. Herein, we designed novel Bi-Cu_2S heterostructures by a one-pot wet-chemistry method. The epitaxial growth of Cu_2S on Bi results in abundant interfacial sites and these heterostructured nanocrystals demonstrated high electrocatalytic performance of ECO_2RR with high current density, largely reduced overpotential, near-unity FE for formate production (Chapter 2). Meanwhile, we see a lot of opportunities for catalysis in a confined space due to their tunable microenvironment and active sites on the surface, leading to a broad spectrum of electrochemical conversion schemes. Herein, we reveal fundamental concepts of confined catalysis by summarizing recent experimental investigations. We mainly focus on carbon nanotubes (CNTs) encapsulated metal-based materials and summarize their applications in emerging electrochemical reactions, including ECO_2RR and more (Chapter 3). Although we were able to obtain high activity and selectivity toward C_1 products, it is more attractive to go beyond C_1 chemicals to produce C_2 products due to their high industrial value. Herein, we designed Ag-modified Cu alloy catalysts that can

create a CO-rich local environment for enhancing C-C coupling on Cu for C_2 formation. Moreover, Ag corporate in Cu can chemically improve the structural stability of Cu lattice. (Chapter 4) Nevertheless, advanced electrocatalytic platforms cannot be developed without a fundamental understanding of binding configurations of the surface-adsorbed intermediates and adsorbate-adsorbate interaction on the local environment in electrochemical CO_2 reduction. In this case, we make discussions of recent developments of machine learning based models of adsorbate-adsorbate interactions, including the oversimplified linear analytic relationships, the cluster expansion models parameterized by machine learning algorithms, and the highly nonlinear deep learning models. We also discuss the challenges of the field, particularly overcoming the limitations of pure data driven models with the integration of computational theory and machine learning of lateral interactions for catalyst materials design. (Chapter 5).

Electrochemical Carbon Dioxide Reduction for Renewable Carbonaceous Fuels and Chemicals

Xue Han

GENERAL AUDIENCE ABSTRACT

Excessive CO_2 emissions into the atmosphere have had severe environmental impacts and pose an urgent and potentially irreversible threat to human activity. Fossil fuels, including coal, oil, and natural gas, have continued to play a dominant role in the global energy system. However, fossil fuels produce substantial greenhouse gases, which are the main contributor to global warming. This year, the global average CO_2 level is increasing to 413.6 parts per million, higher than at any point in the past hundred years. To address this global warming issue, we see lots of opportunities to use alternative energy sources to convert atmospheric CO_2 into value-added products through the electrochemical reduction of CO_2. Nevertheless, advanced electrocatalytic platforms cannot be developed without efficient electrocatalysts in the reaction system. Therefore, we have been working on the design of catalysts with various features that improve the electrochemical reduction of CO_2. The interface plays an important role as the reactions are happening at the active sites which mostly locate at the interface of electrocatalysts. We designed a novel Bi-Cu_2S hetero-structured catalyst, which has abundant interfacial sites between Bi and Cu_2S, demonstrating the improved catalytic performance of ECO_2RR toward formate production (Chapter 2). Catalysis in a confined space offers another opportunity for tuning the catalytic performance, where carbon nanotubes (CNTs) encapsulated metal-based materials have been shown to increase the reactivity of electrochemical reactions, including ECO_2RR and more (Chapter 3). Interfaces in alloys provide multifunctional environments

which have been shown to have reactivity toward complicated reactions. To produce more value-added C_2 chemicals, Ag-modified Cu alloy catalysts are developed, which can create a CO-rich local environment for enhancing C-C coupling on Cu to enhance C_2 formation (Chapter 4). To develop advanced electrocatalytic platforms for CO_2 electroreduction, it is essential to have a fundamental understanding of the binding configurations of surface-adsorbed intermediates and the adsorbate-adsorbate interaction within the local environment. In this regard, we discussed recent developments in machine learning-based models of adsorbate-adsorbate interactions for multiple electrochemical reactions (Chapter 5).

ACKNOWLEDGEMENTS

I would like to express my sincere thanks to my advisor, Dr. Huiyuan zhu, for her invaluable patience and wholehearted support. She has always provided me with valuable guidance and feedback, challenging me to grow as a scientist. I'm incredibly fortunate to be a member of Zhu lab. At the same time, I would like to appreciate my co-advisor, Dr. Hongliang Xin, who gave me lots of guidance and support during my final year of Ph.D.

Besides, I would also like to thank my committee members, Dr. Rong Tong and Dr. Feng Lin, for their brilliant comments and suggestions. Thank you to all academics who helped me get to this stage.

I also like to give special thanks to my friends, Mengxia Ji, Xiaoqian Wang, who are always by my side to cheer me up when I break down emotionally. I absolutely appreciate my group members, Qiang Gao, Zihao Yan, Bokki Min, and Yuanqi Liu. Besides, I would like to thank all undergraduate students who helped me with my experiments in the lab.

Most importantly, none of this would happen without my family - my parents, my husband Tianyou Mou and our sweet dog Yuanqiu Han. Their love and understanding have made me a better person.

Wishing us a bright future where all dreams come true.

Table of contents

CHAPTER 1

Introduction

1.1 Background

The excessive emission of carbon dioxide (CO_2) into the atmosphere has resulted in severe environmental consequences and poses an urgent and potentially irreversible threat to human activities.[1] According to the U.S. energy administration, fossil fuels, including coal, oil, and natural gas, have continued to play a dominant role in the global energy system.[2-4] However, fossil fuels produce substantial greenhouse gases, which are the main contributor to global warming. In 2022, the global average CO_2 level was increasing to 417.3 parts per million,[5] higher than at any time in the past hundred years. To address the global warming issue, we see lots of opportunities to use alternative energy sources to convert atmospheric CO_2 into value-added products. However, energy derived from renewable sources is limited to 30% due to their intermittent nature.[1, 6] Therefore, it is more feasible to capture CO_2 from point sources such as power plants and convert it into chemical feedstocks and fuels as an alternative. Electrochemical CO_2 reduction reaction (ECO_2RR) is an elegant long-term solution for converting renewable electricity into synthetic fuels and chemicals, reducing our dependence on fossil fuels.[7-10] As schematically illustrated in **Figure 1.1**, the electrochemical electrolyzer converts excessive CO_2 into value-added chemicals and fuels powered by renewable electricity. The resulting products can be used as raw materials for more complex chemical synthesis, forming a carbon-neutral cycle.

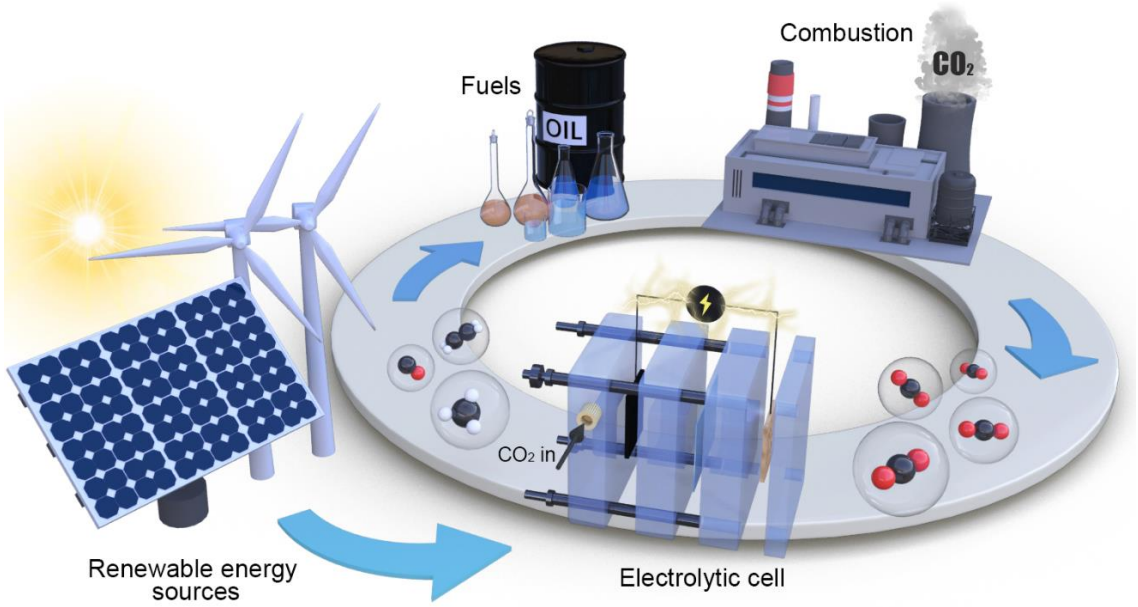

Figure 1.1 Schematic illustration of carbon cycling powered by sustainable energy sources such as solar and wind energy.

However, ECO_2RR usually suffers from significant overpotential because CO_2 is a very stable gas. In this case, high energy is required to break the C=O bond, leading to significant overpotential.[1, 11-12] CO_2 reduction reaction can generate various products, such as carbon monoxide (CO), formic acid (HCOOH), methane (CH_4), ethylene (C_2H_4), alcohol (CH_3CH_2OH) and so on. This is because CO_2 reduction involves multi-proton and electron transfer steps that result in a number of possible reaction intermediates and products in aqueous media.[1, 13-15] **Table 1.1** summarized the half-reactions of the main ECO_2RR products and their corresponding thermodynamic redox potentials (V *vs.* standard hydrogen electrode (SHE)) in an aqueous solution. In fact, in CO_2 reduction reaction, it prefers to generate a mixture compound of gaseous products and liquid products rather than

a single product in ECO_2RR.[7] This brings a number of serious technological hurdles, including low efficiency, low product selectivity, and high cost for liquid product separation. Particularly, due to the limiting selectivity and stability of existing electrocatalysts, current techniques are hard to reach the standard requirements for the industrial level. In the past decades, numerous efforts have been made to develop electrocatalysts and optimize reaction conditions in order to overcome the aforementioned obstacles. In recent years, as the global demand for clean energy has increased, CO_2 reduction research has made remarkable progress.[16-20] In this regard, a comprehensive understanding includes various aspects, such as reaction mechanism, electrocatalyst development, as well as challenges and perspectives, is necessary for promoting the further development in the advanced electrocatalysis field.

Table 1.1. Half electrochemical thermodynamic reactions of ECO_2RR, corresponding with their standard redox potentials (V vs. SHE). Reproduced with permission from John Wiley and Sons.

Possible half-reactions of electrochemical CO_2 reduction	Electrode potentials (V vs SHE) at pH 7
$CO_2\ (g) + e^- \rightarrow {}^*COO^-$	–1.90
$CO_2\ (g) + 2H^+ + 2e^- \rightarrow HCOOH\ (l)$	–0.61
$CO_2\ (g) + H_2O\ (l) + 2e^- \rightarrow HCOO^-\ (aq) + OH^-$	–0.43
$CO_2\ (g) + 2H^+ + 2e^- \rightarrow CO\ (g) + H_2O\ (l)$	–0.53
$CO_2\ (g) + H_2O\ (l) + 2e^- \rightarrow CO\ (g) + 2OH^-$	–0.52
$CO_2\ (g) + 4H^+ + 2e^- \rightarrow HCHO\ (l) + H_2O\ (l)$	–0.48
$CO_2\ (g) + 3H_2O\ (l) + 4e^- \rightarrow HCHO\ (l) + 4OH^-$	–0.89
$CO_2\ (g) + 6H^+\ (l) + 6e^- \rightarrow CH_3OH\ (l) + H_2O\ (l)$	–0.38
$CO_2\ (g) + 5H_2O\ (l) + 6e^- \rightarrow CH_3OH\ (l) + 6OH^-$	–0.81
$CO_2\ (g) + 8H^+ + 8e^- \rightarrow CH_4\ (g) + 2H_2O\ (l)$	–0.24
$CO_2\ (g) + 6H_2O\ (l) + 8e^- \rightarrow CH_4\ (g) + 8OH^-$	–0.25
$2CO_2\ (g) + 12H^+ + 12e^- \rightarrow C_2H_4\ (g) + 4H_2O\ (l)$	0.06
$2CO_2\ (g) + 8H_2O\ (l) + 12e^- \rightarrow C_2H_4\ (g) + 12OH^-$	–0.34
$2CO_2\ (g) + 12H^+ + 12e^- \rightarrow CH_3CH_2OH\ (l) + 3H_2O\ (l)$	0.08
$2CO_2\ (g) + 9H_2O\ (l) + 12e^- \rightarrow CH_3CH_2OH\ (l) + 12OH^-\ (l)$	–0.33

1.2 Electrocatalyst categories

1.2.1 Metals

Metal catalysts for ECO_2RR can be classified into three groups based on their major products.[7] According to previous studies, Sn and Pb catalysts are excellent candidates for formate production since $CO_2^{\cdot-}$ intermediates can be desorbed easily from the metal surface.[21] Ag, Au, Zn, and Pd catalysts are in favor of binding *COOH intermediates while having weak binding of *CO species; therefore, those metals catalysts are used for CO production.[22-24] Cu is the only single metal that can be able to produce C_{2+} products.[25] Because of their particularity, Cu and Cu-based materials have received considerable attention in the field of electrocatalysis. In **Figure 1.2**,[26] we classified metal catalysts for ECO_2RR by their major products, using the periodic table with different colors.

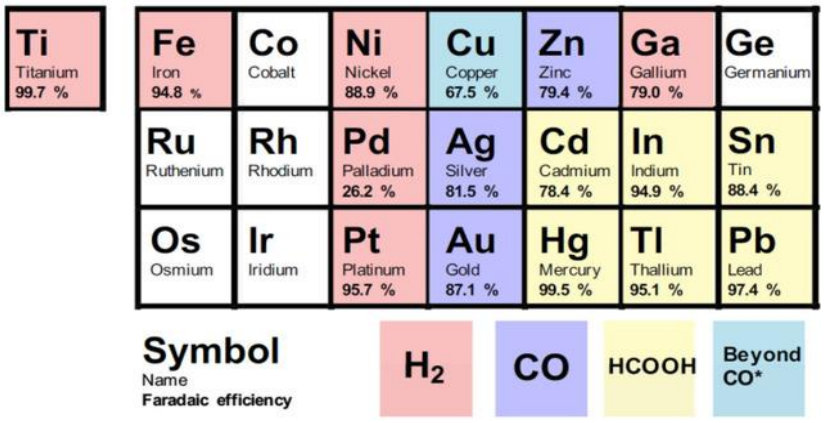

Figure 1.2 Major product categories of metal catalysts for CO_2 electroreduction, shown in a periodic table with colors. Reproduced with permission from John Wiley and Sons.

1.2.2 Metal alloys

Metal alloys have gradually attracted more attention since they can improve CO_2 catalytic performance by tuning the binding capability of CO_2 intermediates.[7] One promising strategy is to introduce non-precious metals into the metal catalysts to form alloys that can lower the overpotential and minimize the cost. Wen et al. designed novel materials of Sn nanosheets decorated with Bi nanoparticles. These Bi-Sn bimetallic electrocatalysts have abundant interfacial sites that could efficiently convert CO_2 to formate. Besides, Bi-Sn showed excellent stability under 100 h operation.[27] Xing et al. reported Bi@Sn core-shell catalysts with high activity and selectivity toward formate in CO_2 reduction.[28] They found that Bi@Sn could achieve 92% of FE on formate production at a steady-state current of -250 mA cm^{-2}, outstanding than most of the state-of-art catalysts. Recently, studies have focused on Cu-based alloys to enhance electrocatalytic performance in C_2 production. Compared to the Au and Cu metal catalysts, Shen et al. designed AuCu alloy nanoparticles embedded Cu submicrocone arrays (AuCu/Cu-SCA) (**Figure 1.3 a,b**) for ECO_2RR by a two-step synthesis method.[29] This electrocatalyst demonstrated an enhanced faradic efficiency toward ethanol in comparison with the C_2H_4. Meanwhile, AuCu/Cu-SCA alloy showed outstanding stability after 24 h reaction. In details, AuCu/Cu-SCA alloy shows a high current density of -4.9 mA cm^{-2} at -0.8 V *vs.* RHE, which is higher than its single compartment, indicating that AuCu/Cu-SCA electrocatalyst has high activity toward CO_2RR (**Figure 1.3c**). The faradic efficiency toward ethanol on AuCu/Cu-SCA can reach to 25% at all applied potentials. By contrast, the FE toward ethanol on Cu-SCA can only reach 8% (**Figure 1.3d**), suggesting that AuCu/Cu-SCA catalyst could efficiently improve the selectivity of ethanol production in ECO_2RR. In conclusion, the study

demonstrated the feasibility of producing inexpensive and highly active alloy electrocatalysts for scalable CO_2 electroreduction.

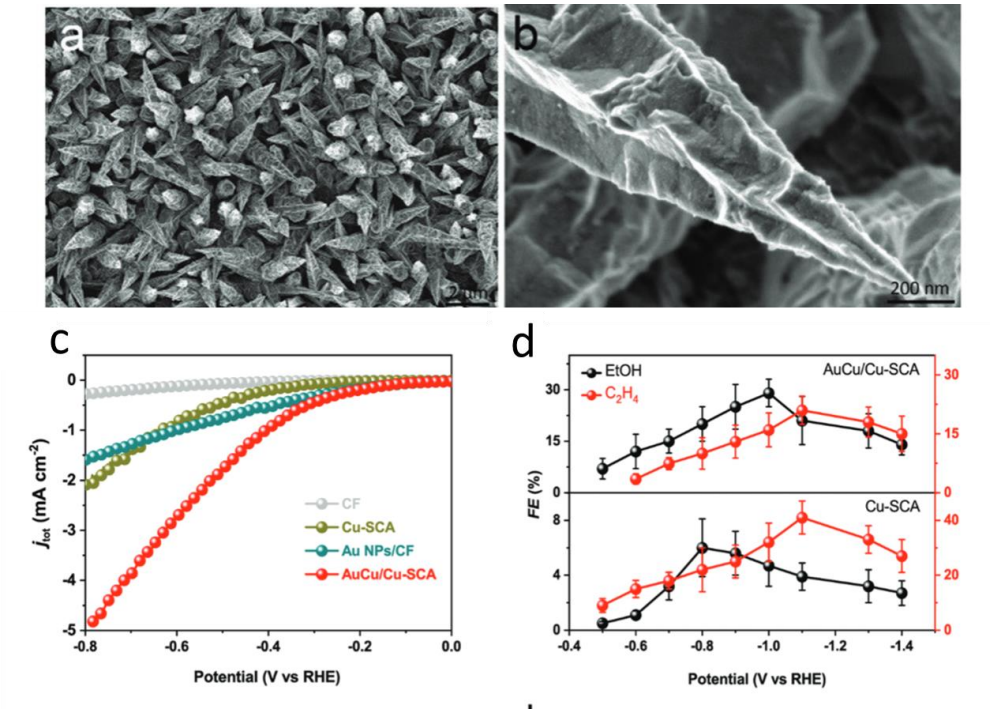

Figure 1.3 a), b) Scanning electron microscopy (SEM) images of AuCu/Cu-SCA. ECO_2RR performance: c) LSV curves measured in CO_2-saturated 0.5 M $KHCO_3$ aqueous solution; d) FEs of ethanol and ethylene at various applied potentials. Reproduced with permission from John Wiley and Sons.

1.2.3 Metal oxides

Metal oxides have achieved attention due to their superior energy efficiency and improved catalytic activity in ECO_2RR. Especially, researchers are more focused on non-precious metals, such as Sn, Ni, and Co, because of their non-toxicity properties and low market price. Zhang et al. reported ultrathin SnO_x nanosheets doped into the surface of commercial multiwalled carbon nanotubes (MWCNTs).[30] The catalyst shows the high performance of ECO_2RR with near-unity selectivity toward C_1 products (formate and CO). Another work reported by Yang et al. uses Cu/Ni oxide composites (CuNiOCs) electrocatalysts for efficient CO_2 reduction toward formate in aqueous media.[31] CuNiOCs catalysts demonstrated low overpotential, near unity FE of formate, high energy efficiency as well as excellent stability. Moreover, another research group synthesized a partially oxidized Co 4-atom-layer with a high FE of 90.1% toward formate over 40 h. They also hypothesized a reaction pathway of formate on partially oxidized Co catalyst surface as below:

$$CO_2(g) + * \rightarrow *CO_2$$

$$*CO_2 + e^- \rightarrow *COO^-$$

$$*COO^- + H^+ + e^- \rightarrow *HCOO^-$$

$$*HCOO^- \rightarrow HCOO^- + *$$

Based on the proposed reaction pathway, the partially oxidized Co 4-atom-layer has great capability for CO_2 activation that enables the stabilization of *COOH intermediates. These works identified that introducing oxygen states into certain metallic metals can tune catalyst active sites, therefore improving the CO_2 reduction performance.

1.2.4 Metal chalcogenides

More recently, studies showed that transition metal chalcogenides (TMC) electrocatalysts performed efficiently in CO_2RR. The CO_2 intermediates can be adsorbed to various active sites on the catalyst surface, breaking the limitation of linear-scale relations between the binding energies of reaction intermediates and specific metals.[7] Shinagawa et al. reported the sulfur-modified Cu electrocatalysts for efficient CO_2 reduction to formate.[32] The faradic efficiency can reach approximately 80% on formate at the potential of -0.8 V *vs.* RHE, outperforming most of the non-precious electrocatalysts reported to date for formate production in ECO_2RR. Another interesting work published by Sun group synthesized a new class of molybdenum-bismuth chalcogenide nanosheets.[33] This electrocatalyst demonstrated high performance of CO_2 reduction to methanol with the faradic efficiency of 71.2% and current density of -12.1 mA cm^{-2}. Therefore, we see lots of opportunities for metal chalcogenides to be utilized in the electrocatalysis field.

1.3 Mechanistic pathways of electrochemical CO_2 reduction

Although the mechanistic pathways of ECO_2RR are not fully elucidated yet, several possible reaction pathways have been proposed based on the combination of theoretical calculations and experimental studies.[34-35] The electrolysis process produces several major products, such as CO, formate, CH_4, $C2H_4$, and alcohols. Herein, we mainly discuss reaction pathways for these most significant products and reaction intermediates.

1.3.1 Selectivity production of C_1 products

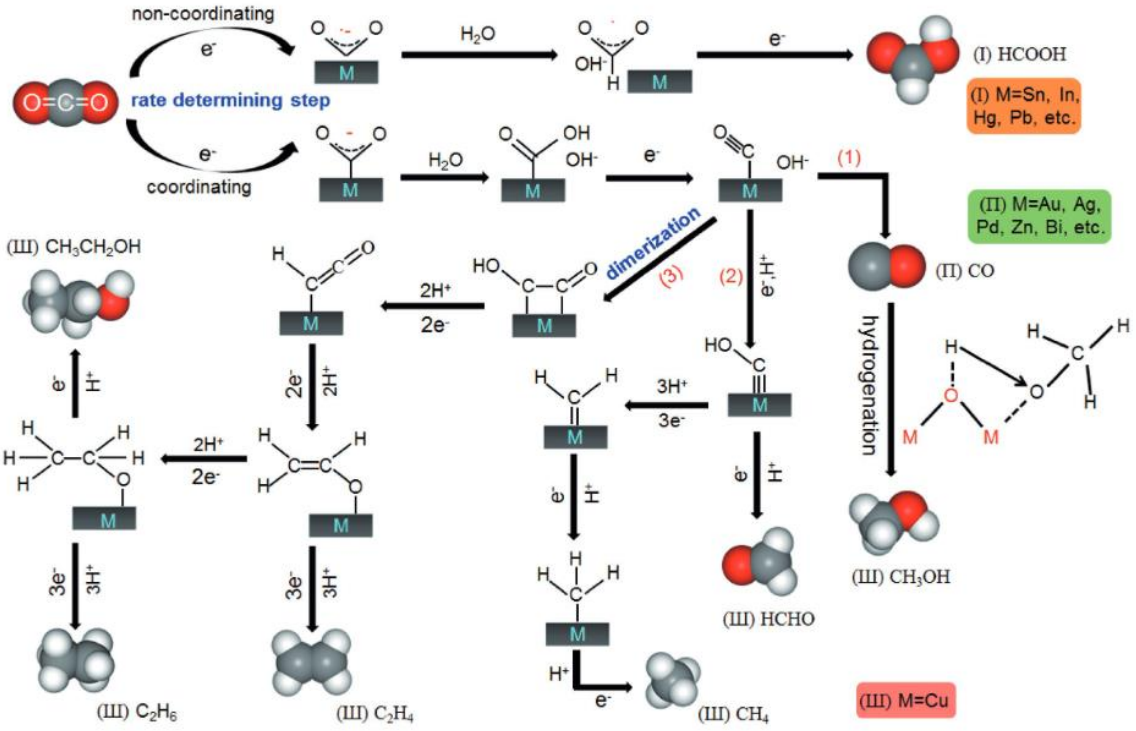

Figure 1.4 Schematic mechanism of different metal electrocatalysts for CO_2 reduction in aqueous solution. Reproduced with permission from John Wiley and Sons.

1.3.1.1 Formate or formic acid

Formic acid is the simplest carboxylic acid, and its chemical formula is HCOOH. It is one of the most significant products of ECO2RR as well as an important intermediate in chemical synthesis. [36-37]

One proposed reaction pathway of ECO_2RR to formate initiates with the formation of radial anion $CO_2^{\cdot-}$ via activating CO_2 with one electron transfer; another proton from water is subsequently involved in forming either carboxyl intermediate *COOH or formate intermediate *OCHO on the catalyst surface. Then, the second electron involves and results

in the formate product (**Figure 1.4**).[7, 38] Recently, theoretical calculations have proposed another possible reaction pathway for formate production.[34, 39-40] The reaction occurs through proton-electron coupled transfer (PECT) on the catalyst surface. In this route, *COOH or *OCHO intermediates form by combining CO_2 and a proton-electron pair on the metal surface, and another proton-electron pair then transfers to the intermediates to produce formate.

1.3.1.2 Carbon monoxide

Carbon monoxide (CO) as another important CO_2 reduction product has attracted much attention because it is an essential feedstock for water-shift reaction and the Fisher-Tropsch process.[41-42] Different from formate formation, CO production requires *COOH tightly adsorbed on the catalyst surface while simultaneously possessing a low binding affinity for *CO intermediate in order to release CO.[34, 43-44] Transition metals including Au, Ag, and Pd demonstrate weak binding of *CO intermediate, thus they are excellent candidates for CO production.[9, 45-47]

1.3.1.3 Methane

Methane (CH_4) is the main component of natural gas. It can be used as the raw material in many chemical synthetics process.[44] There are two possible reaction pathways which have been proposed in previous studies. Peterson et al. reported that *CO species is formed first. After PECT process, *OCH_3 is formed and bonded on the catalyst surface. With another PECT occurring on *OCH_3 intermediate, methane is formed while the surface absorbed oxygen is quenched by protonation process.[34] The second proposed pathway suggests that *COH intermediate could turn into *C species at very negative potential. *C species can be further reduced to *CH, *CH_2, *CH_3, and then methane.[48] However, the

energy barrier to form *C is high, it can occur only at very negative potentials. From previous studies, Cu and Cu-based electrocatalysts demonstrate its excellent performance on hydrocarbon (CH_4) production.[49-51]

1.3.1.4 Methanol

Methanol is a promising product in ECO_2RR, which can be used as a solvent, pesticide, and alternative fuel source.[44, 52] There are many proposed reaction pathways of methanol formation, but the detailed reaction mechanism is still unclear. One probable route suggests that *CO species is formed first.[34] Then, *OCH_3 species is formed via the competition between the desorption of HCHO and the PECT to HCHO bonded on the surface, followed by another PECT and bonded on the catalyst surface. Afterward, another PECT process occurring on *OCH_3 intermediate results in methanol.

1.3.2 Selectivity production of C_2 and C_{2+} products

C_2 products (e.g., C_2H_4, CH_3COOH, C_2H_5OH) are more attractive due to their high value and energy density compared to C_1 products. However, C_2 product formation usually needs enough negative overpotential to overcome the high energy barrier, and they always form simultaneously in the reduction reaction.[53-57] Therefore, the reaction pathway for C_2 products is complicated and still unclear. Many possible reaction pathways have been proposed with the efforts of theoretical calculation and experimental studies. Ethylene may form through the dimerization of *CH_2 species or form the ethylene oxide (*$OCHCH_2$) species via the dimerization of *CO on the catalyst surface.[58] Meanwhile, by inserting of

*CO species into *CH_2 or PECT to oxygen site of *$OCHCH_2$, ethanol can be achieved in ECO_2RR.

The most challenging thing for the formation of C_2 and C_{2+} products is the scaling relation between the activation and binding energies of intermediates. The catalyst active sites need to bind those intermediates tightly enough to provide sufficient coverage for the C-C coupling step but not so tightly to poison the catalyst surface.[44] Additionally, Cu and Cu-based catalysts are the most promising catalysts to generate C_2 products due to their appropriate affinity for *CO intermediates.[59-62]

1.4 Scope and outline

ECO_2RR powered by renewable electricity holds promise to store intermittent energy in chemical bonds while producing sustainable chemicals and fuels. Unfortunately, it remains grand challenges:

- The reaction usually suffers from sluggish kinetic during the CO_2 reduction, leading to low energy efficiency and high overpotential.
- ECO_2RR has broad product distribution due to multi-electron and -proton transfer steps. The products are usually a mixture compound of gaseous products (CO, H_2) and liquid products (formate, ethanol); thus, product separation is another issue.
- The activity degradation of catalysts during the reaction originated from the instability of catalysts, particularly non-precious metals.
- A complete system of comprehensive theoretical and experimental research system has not been fully developed.

On the basis of these challenges, we report novel Bi-Cu_2S heterostructures by a one-pot wet-chemistry method. The epitaxial growth of Cu_2S on Bi results in abundant interfacial sites, and these heterostructured nanocrystals demonstrated high electrocatalytic performance of ECO_2RR with high current density, largely reduced overpotential, near-unity FE for formate production (Chapter 2). Meanwhile, we see a lot of opportunities for catalysis in a confined space due to their tunable microenvironment and active sites on the surface, leading to a broad spectrum of electrochemical conversion schemes. Herein, we reveal fundamental concepts of confined catalysis by summarizing recent experimental investigations. We mainly focus on carbon nanotubes (CNTs) encapsulated metal-based materials and summarize their applications in emerging electrochemical reactions, including ECO_2RR and more (Chapter 3). Although we were able to obtain high activity and selectivity toward C_1 products, it is more attractive to go beyond C_1 chemicals to produce C_2 products due to their high industrial value. Herein, we designed Ag-modified Cu alloy catalysts that can create a CO-rich local environment for enhancing C-C coupling on Cu for C_2 formation. Moreover, Ag corporate in Cu can chemically improve the structural stability of Cu lattice. (Chapter 4) Nevertheless, advanced electrocatalytic platforms cannot be developed without a fundamental understanding of binding configurations of the surface-adsorbed intermediates and adsorbate-adsorbate interaction on the local environment in CO_2 electroreduction. In this case, we make discussions of recent developments of machine learning based models of adsorbate-adsorbate interactions, including the oversimplified linear analytic relationships, the cluster expansion models parameterized by machine learning algorithms, and the highly nonlinear deep learning models. We also discuss the challenges of the field, particularly to overcome the limitations

of pure data driven models with the integration of computational theory and machine learning of lateral interactions for catalyst materials design. (Chapter 5).

References

1. Fan, L.; Xia, C.; Yang, F.; Wang, J.; Wang, H.; Lu, Y., Strategies in catalysts and electrolyzer design for electrochemical CO_2 reduction toward C_2 products. *Sci. Adv.* **2020,** *6* (8), eaay3111.

2. Whipple, D. T.; Kenis, P. J. A., Prospects of CO_2 Utilization via Direct Heterogeneous Electrochemical Reduction. *J. Phys. Chem. Lett.* **2010,** *1* (24), 3451-3458.

3. Maginn, E. J., What to Do with CO_2. *J. Phys. Chem. Lett.* **2010,** *1* (24), 3478-3479.

4. Hernández, S.; Farkhondehfal, M. A.; Sastre, F.; Makkee, M.; Saracco, G.; Russo, N., Syngas production from electrochemical reduction of CO_2: current status and prospective implementation. *Green Chemistry* **2017,** *19* (10), 2326-2346.

5. Lindsey, R. Climate Change: Atmospheric Carbon Dioxide. https://www.climate.gov/news-features/understanding-climate/climate-change-atmospheric-carbon-dioxide (accessed 8/7).

6. Jhong, H.-R. M.; Ma, S.; Kenis, P. J. A., Electrochemical conversion of CO_2 to useful chemicals: current status, remaining challenges, and future opportunities. *Curr. Opin. Chem. Eng.* **2013,** *2* (2), 191-199.

7. Zhang, W.; Hu, Y.; Ma, L.; Zhu, G.; Wang, Y.; Xue, X.; Chen, R.; Yang, S.; Jin, Z., Progress and Perspective of Electrocatalytic CO_2 Reduction for Renewable Carbonaceous Fuels and Chemicals. *Adv. Sci* **2018,** *5* (1), 1700275.

8. Chen, Y.; Chen, K.; Fu, J.; Yamaguchi, A.; Li, H.; Pan, H.; Hu, J.; Miyauchi, M.; Liu, M., Recent advances in the utilization of copper sulfide compounds for electrochemical CO_2 reduction. *Nano Materials Science* **2020,** *2* (3), 235-247.

9. Zhang, Z.; Chi, M.; Veith, G. M.; Zhang, P.; Lutterman, D. A.; Rosenthal, J.; Overbury, S. H.; Dai, S.; Zhu, H., Rational Design of Bi Nanoparticles for Efficient Electrochemical CO_2 Reduction: The Elucidation of Size and Surface Condition Effects. *ACS Catal.* **2016,** *6* (9), 6255-6264.

10. Quan, W.; Lin, Y.; Luo, Y.; Huang, Y., Electrochemical CO_2 Reduction on Cu: Synthesis-Controlled Structure Preference and Selectivity. *Adv. Sci.* **2021,** *8* (23), 2101597.

11. Li, K.; Peng, B.; Peng, T., Recent Advances in Heterogeneous Photocatalytic CO_2 Conversion to Solar Fuels. *ACS Catal.* **2016,** *6* (11), 7485-7527.

12. Verma, S.; Kim, B.; Jhong, H.-R. M.; Ma, S.; Kenis, P. J. A., A Gross-Margin Model for Defining Technoeconomic Benchmarks in the Electroreduction of CO_2. *ChemSusChem* **2016,** *9* (15), 1972-1979.

13. Vasileff, A.; Xu, C.; Jiao, Y.; Zheng, Y.; Qiao, S.-Z., Surface and Interface Engineering in Copper-Based Bimetallic Materials for Selective CO_2 Electroreduction. *Chem* **2018,** *4* (8), 1809-1831.

14. Zhao, Q.; Martirez, J. M. P.; Carter, E. A., Revisiting Understanding of Electrochemical CO_2 Reduction on Cu(111): Competing Proton-Coupled Electron Transfer Reaction Mechanisms Revealed by Embedded Correlated Wavefunction Theory. *J. Am. Chem. Soc.* **2021,** *143* (16), 6152-6164.

15. Barton Cole, E.; Lakkaraju, P. S.; Rampulla, D. M.; Morris, A. J.; Abelev, E.; Bocarsly, A. B., Using a One-Electron Shuttle for the Multielectron Reduction of CO_2 to Methanol: Kinetic, Mechanistic, and Structural Insights. *J. Am. Chem. Soc.* **2010,** *132* (33), 11539-11551.

16. Chen, C.; Khosrowabadi Kotyk, J. F.; Sheehan, S. W., Progress toward Commercial Application of Electrochemical Carbon Dioxide Reduction. *Chem* **2018,** *4* (11), 2571-2586.

17. Nitopi, S.; Bertheussen, E.; Scott, S. B.; Liu, X.; Engstfeld, A. K.; Horch, S.; Seger, B.; Stephens, I. E. L.; Chan, K.; Hahn, C.; Nørskov, J. K.; Jaramillo, T. F.; Chorkendorff, I., Progress and Perspectives of Electrochemical CO2 Reduction on Copper in Aqueous Electrolyte. *Chem. Rev.* **2019,** *119* (12), 7610-7672.

18. Zhang, B.; Jiang, Y.; Gao, M.; Ma, T.; Sun, W.; Pan, H., Recent progress on hybrid electrocatalysts for efficient electrochemical CO_2 reduction. *Nano Energy* **2021,** *80*, 105504.

19. Kibria, M. G.; Edwards, J. P.; Gabardo, C. M.; Dinh, C.-T.; Seifitokaldani, A.; Sinton, D.; Sargent, E. H., Electrochemical CO_2 Reduction into Chemical Feedstocks: From Mechanistic Electrocatalysis Models to System Design. *Adv. Mater.* **2019,** *31* (31), 1807166.

20. Li, X.; Wang, S.; Li, L.; Sun, Y.; Xie, Y., Progress and Perspective for In Situ Studies of CO_2 Reduction. *J. Am. Chem. Soc.* **2020,** *142* (21), 9567-9581.

21. Li, H.; Oloman, C., Development of a continuous reactor for the electro-reduction of carbon dioxide to formate–Part 1: Process variables. *Energy Environ. Sci.* **2006,** *36* (10), 1105-1115.

22. Zhu, D. D.; Liu, J. L.; Qiao, S. Z., Recent advances in inorganic heterogeneous electrocatalysts for reduction of carbon dioxide. *Adv. Mater.* **2016,** *28* (18), 3423-3452.

23. Buckley, A. K.; Cheng, T.; Oh, M. H.; Su, G. M.; Garrison, J.; Utan, S. W.; Zhu, C.; Toste, F. D.; Goddard, W. A.; Toma, F. M., Approaching 100% Selectivity at Low Potential on Ag for Electrochemical CO_2 Reduction to CO Using a Surface Additive. *ACS Catal.* **2021,** *11* (15), 9034-9042.

24. Rosen, J.; Hutchings, G. S.; Lu, Q.; Rivera, S.; Zhou, Y.; Vlachos, D. G.; Jiao, F., Mechanistic Insights into the Electrochemical Reduction of CO_2 to CO on Nanostructured Ag Surfaces. *ACS Catal.* **2015,** *5* (7), 4293-4299.

25. Ma, S.; Sadakiyo, M.; Heima, M.; Luo, R.; Haasch, R. T.; Gold, J. I.; Yamauchi, M.; Kenis, P. J. A., Electroreduction of Carbon Dioxide to Hydrocarbons Using Bimetallic Cu–Pd Catalysts with Different Mixing Patterns. *J. Am. Chem. Soc.* **2017,** *139* (1), 47-50.

26. Bagger, A.; Ju, W.;. Varela, A. S.; Strasser,P.; Rossmeisl, J., Electrochemical CO_2 Reduction: A Classification Problem. *ChemPhysChem.* **2017**, 18, 3266.

27. Wen, G.; Lee, D. U.; Ren, B.; Hassan, F. M.; Jiang, G.; Cano, Z. P.; Gostick, J.; Croiset, E.; Bai, Z.; Yang, L.; Chen, Z., Orbital Interactions in Bi-Sn Bimetallic Electrocatalysts for Highly Selective Electrochemical CO_2 Reduction toward Formate Production. *Adv. Energy Mater.* **2018,** *8* (31), 1802427.

28. Xing, Y.; Kong, X.; Guo, X.; Liu, Y.; Li, Q.; Zhang, Y.; Sheng, Y.; Yang, X.; Geng, Z.; Zeng, J., Bi@Sn Core–Shell Structure with Compressive Strain Boosts the Electroreduction of CO_2 into Formic Acid. *Adv. Sci.* **2020,** *7* (22), 1902989.

29. Shen, S.; Peng, X.; Song, L.; Qiu, Y.; Li, C.; Zhuo, L.; He, J.; Ren, J.; Liu, X.; Luo, J., AuCu Alloy Nanoparticle Embedded Cu Submicrocone Arrays for Selective Conversion of CO_2 to Ethanol. *Small* **2019,** *15* (37), 1902229.

30. Zhang, Q.; Zhang, Y.; Mao, J.; Liu, J.; Zhou, Y.; Guay, D.; Qiao, J., Electrochemical reduction of CO_2 by SnO_x nanosheets anchored on multiwalled carbon nanotubes with tunable functional groups. *ChemSusChem* **2019,** *12* (7), 1443-1450.

31. Yang, D.; Zhu, Q.; Sun, X.; Chen, C.; Lu, L.; Guo, W.; Liu, Z.; Han, B., Nanoporous Cu/Ni oxide composites: efficient catalysts for electrochemical reduction of CO_2 in aqueous electrolytes. *Green Chem.* **2018,** *20* (16), 3705-3710.

32. Shinagawa, T.; Larrazábal, G. O.; Martín, A. J.; Krumeich, F.; Pérez-Ramírez, J., Sulfur-modified copper catalysts for the electrochemical reduction of carbon dioxide to formate. *ACS Catal.* **2018,** *8* (2), 837-844.

33. Sun, X.; Zhu, Q.; Kang, X.; Liu, H.; Qian, Q.; Zhang, Z.; Han, B., Molybdenum–Bismuth Bimetallic Chalcogenide Nanosheets for Highly Efficient Electrocatalytic Reduction of Carbon Dioxide to Methanol. *Angew. Chem. Int. Ed.* **2016,** *55* (23), 6771-6775.

34. Peterson, A. A.; Abild-Pedersen, F.; Studt, F.; Rossmeisl, J.; Nørskov, J. K., How copper catalyzes the electroreduction of carbon dioxide into hydrocarbon fuels. *Energy Environ. Sci.* **2010,** *3* (9), 1311-1315.

35. Liu, X.; Xiao, J.; Peng, H.; Hong, X.; Chan, K.; Nørskov, J. K., Understanding trends in electrochemical carbon dioxide reduction rates. *Nat. Commun.* **2017,** *8* (1), 15438.

36. Jiang, X.; Wang, X.; Liu, Z.; Wang, Q.; Xiao, X.; Pan, H.; Li, M.; Wang, J.; Shao, Y.; Peng, Z.; Shen, Y.; Wang, M., A highly selective tin-copper bimetallic electrocatalyst for the electrochemical reduction of aqueous CO_2 to formate. *Appl. Catal. B* **2019,** *259*, 118040.

37. Han, N.; Ding, P.; He, L.; Li, Y.; Li, Y., Promises of Main Group Metal–Based Nanostructured Materials for Electrochemical CO_2 Reduction to Formate. *Adv. Energy Mater.* **2020,** *10* (11), 1902338.

38. Genovese, C.; Ampelli, C.; Perathoner, S.; Centi, G., Mechanism of C–C bond formation in the electrocatalytic reduction of CO_2 to acetic acid. A challenging reaction to use renewable energy with chemistry. *Green Chem.* **2017,** *19* (10), 2406-2415.

39. Yoo, J. S.; Christensen, R.; Vegge, T.; Nørskov, J. K.; Studt, F., Theoretical insight into the trends that guide the electrochemical reduction of carbon dioxide to formic acid. *ChemSusChem* **2016,** *9* (4), 358-363.

40. Feaster, J. T.; Shi, C.; Cave, E. R.; Hatsukade, T.; Abram, D. N.; Kuhl, K. P.; Hahn, C.; Nørskov, J. K.; Jaramillo, T. F., Understanding selectivity for the electrochemical reduction of carbon dioxide to formic acid and carbon monoxide on metal electrodes. *ACS Catal.* **2017,** *7* (7), 4822-4827.

41. Navarro, V.; Van Spronsen, M. A.; Frenken, J. W., In situ observation of self-assembled hydrocarbon Fischer–Tropsch products on a cobalt catalyst. *Nat. Chem* **2016,** *8* (10), 929-934.

42. Gokhale, A. A.; Dumesic, J. A.; Mavrikakis, M., On the mechanism of low-temperature water gas shift reaction on copper. *J. Am. Chem. Soc.* **2008,** *130* (4), 1402-1414.

43. Hansen, H. A.; Varley, J. B.; Peterson, A. A.; Nørskov, J. K., Understanding trends in the electrocatalytic activity of metals and enzymes for CO_2 reduction to CO. *J. Phys. Chem. Lett*. **2013,** *4* (3), 388-392.

44. Long, C.; Li, X.; Guo, J.; Shi, Y.; Liu, S.; Tang, Z., Electrochemical Reduction of CO_2 over Heterogeneous Catalysts in Aqueous Solution: Recent Progress and Perspectives. *Small Methods* **2019,** *3* (3), 1800369.

45. Liu, S.; Tao, H.; Zeng, L.; Liu, Q.; Xu, Z.; Liu, Q.; Luo, J.-L., Shape-dependent electrocatalytic reduction of CO2 to CO on triangular silver nanoplates. *J. Am. Chem. Soc.* **2017,** *139* (6), 2160-2163.

46. Rogers, C.; Perkins, W. S.; Veber, G.; Williams, T. E.; Cloke, R. R.; Fischer, F. R., Synergistic enhancement of electrocatalytic CO_2 reduction with gold nanoparticles embedded in functional graphene nanoribbon composite electrodes. *J. Am. Chem. Soc.* **2017,** *139* (11), 4052-4061.

47. Geng, Z.; Kong, X.; Chen, W.; Su, H.; Liu, Y.; Cai, F.; Wang, G.; Zeng, J., Oxygen vacancies in ZnO nanosheets enhance CO_2 electrochemical reduction to CO. *Angewandte Chemie* **2018,** *130* (21), 6162-6167.

48. Nie, X.; Esopi, M. R.; Janik, M. J.; Asthagiri, A., Selectivity of CO_2 reduction on copper electrodes: the role of the kinetics of elementary steps. *Angewandte Chemie* **2013,** *125* (9), 2519-2522.

49. Wang, Y.; Chen, Z.; Han, P.; Du, Y.; Gu, Z.; Xu, X.; Zheng, G., Single-atomic Cu with multiple oxygen vacancies on ceria for electrocatalytic CO_2 reduction to CH_4. *ACS Catal.* **2018,** *8* (8), 7113-7119.

50. Weng, Z.; Wu, Y.; Wang, M.; Jiang, J.; Yang, K.; Huo, S.; Wang, X.-F.; Ma, Q.; Brudvig, G. W.; Batista, V. S., Active sites of copper-complex catalytic materials for electrochemical carbon dioxide reduction. *Nat. Commun.* **2018,** *9* (1), 1-9.

51. Li, Y.; Cui, F.; Ross, M. B.; Kim, D.; Sun, Y.; Yang, P., Structure-sensitive CO_2 electroreduction to hydrocarbons on ultrathin 5-fold twinned copper nanowires. *Nano Lett.* **2017,** *17* (2), 1312-1317.

52. Chang, J.; Feng, L.; Jiang, K.; Xue, H.; Cai, W.-B.; Liu, C.; Xing, W., Pt–CoP/C as an alternative PtRu/C catalyst for direct methanol fuel cells. *J. Mater. Chem. A* **2016,** *4* (47), 18607-18613.

53. Jiang, K.; Sandberg, R. B.; Akey, A. J.; Liu, X.; Bell, D. C.; Nørskov, J. K.; Chan, K.; Wang, H., Metal ion cycling of Cu foil for selective C–C coupling in electrochemical CO_2 reduction. *Nat. Catal* **2018,** *1* (2), 111-119.

54. De Luna, P.; Quintero-Bermudez, R.; Dinh, C.-T.; Ross, M. B.; Bushuyev, O. S.; Todorović, P.; Regier, T.; Kelley, S. O.; Yang, P.; Sargent, E. H., Catalyst electro-redeposition controls morphology and oxidation state for selective carbon dioxide reduction. *Nat. Catal* **2018,** *1* (2), 103-110.

55. Zhuang, T.-T.; Liang, Z.-Q.; Seifitokaldani, A.; Li, Y.; De Luna, P.; Burdyny, T.; Che, F.; Meng, F.; Min, Y.; Quintero-Bermudez, R., Steering post-C–C coupling selectivity enables high efficiency electroreduction of carbon dioxide to multi-carbon alcohols. *Nat. Catal* **2018,** *1* (6), 421-428.

56. Dinh, C.-T.; Burdyny, T.; Kibria, M. G.; Seifitokaldani, A.; Gabardo, C. M.; García de Arquer, F. P.; Kiani, A.; Edwards, J. P.; De Luna, P.; Bushuyev, O. S., CO_2 electroreduction to ethylene via hydroxide-mediated copper catalysis at an abrupt interface. *Science* **2018,** *360* (6390), 783-787.

57. Kim, D.; Kley, C. S.; Li, Y.; Yang, P., Copper nanoparticle ensembles for selective electroreduction of CO_2 to C_2–C_3 products. *Proc. Natl. Acad. Sci.* **2017,** *114* (40), 10560-10565.

58. Schouten, K. J. P.; Qin, Z.; Pérez Gallent, E.; Koper, M. T., Two pathways for the formation of ethylene in CO reduction on single-crystal copper electrodes. *J. Am. Chem. Soc.* **2012,** *134* (24), 9864-9867.

59. Xue, Y.; Guo, Y.; Cui, H.; Zhou, Z., Catalyst Design for Electrochemical Reduction of CO_2 to Multicarbon Products. *Small Methods* **2021,** *5* (10), 2100736.

60. Wang, Z.; Yuan, Q.; Shan, J.; Jiang, Z.; Xu, P.; Hu, Y.; Zhou, J.; Wu, L.; Niu, Z.; Sun, J.; Cheng, T.; Goddard, W. A., Highly Selective Electrocatalytic Reduction of CO_2 into Methane on Cu–Bi Nanoalloys. *The Journal of Physical Chemistry Letters* **2020,** *11* (17), 7261-7266.

61. Yang, D.; Zhu, Q.; Chen, C.; Liu, H.; Liu, Z.; Zhao, Z.; Zhang, X.; Liu, S.; Han, B., Selective electroreduction of carbon dioxide to methanol on copper selenide nanocatalysts. *Nat. Commun.* **2019,** *10* (1), 677.

62. Ma, W.; Xie, S.; Liu, T.; Fan, Q.; Ye, J.; Sun, F.; Jiang, Z.; Zhang, Q.; Cheng, J.; Wang, Y., Electrocatalytic reduction of CO_2 to ethylene and ethanol through hydrogen-assisted C–C coupling over fluorine-modified copper. *Nat. Catal* **2020,** *3* (6), 478-487.

CHAPTER 2

Bi-Cu_2S heterostructures for CO_2 electroreduction to formate

2.1 Introduction

Electrochemical CO_2 reduction reaction (ECO_2RR) is considered a promising strategy to sustainably recycle CO_2 into the anthropogenic carbon cycle, paving the road to a clean-energy future.[1-10] Despite its promise, ECO_2RR usually suffers from: i) significant overpotential, leading to low energy efficiency; ii) broad product distribution in aqueous electrolytes resulting from the multi-proton/electron transfer steps, and iii) the competition with the hydrogen evolution reaction (HER) and, thus, limited selectivity.[1, 11-12]

Metal and metal-based catalysts have been commonly used for the ECO_2RR to CO, formate, and C_{2+} products.[1, 3, 7, 13-14] Among those catalysts, nanostructured *p*-block metals such as Pb, In, and Bi demonstrate high selectivity toward formate production due to their passivation of HER.[11-12, 15-16] Bi becomes especially attractive because of its low cost and non-toxicity.[17] However, monometallic Bi usually suffers from high overpotential (>800 mV) as well as a low current density (<10 mA cm^{-2}).[18-19] This can be attributed to the relatively weak binding of ECO_2RR intermediates (*e.g.*, *OCHO, *COOH) on Bi surfaces. Thus, a more reductive potential is required to stabilize those intermediates to enable electron and proton transfer steps. Alloying Bi with other transition metals is a common approach to tune the stability of reaction intermediate, as shown in the Bi-Sn,[11, 20-22] Bi-Cu,[23-25] and Bi-Mo[26] systems. Nevertheless, a trade-off among overpotentials, Faradaic efficiencies (FEs), and current densities is commonly observed due to adsorption-energy scaling relations of alloy surfaces that impose constraints on attainable catalytic

performances.[27-29] To achieve this goal, constructing interfacial sites that can selectively stabilize relevant ECO_2RR intermediates on Bi surfaces could be a viable solution to improve electrokinetics while maintaining the high FE toward formate. To design an efficient interfacial site with Bi for ECO_2RR, transition metal chalcogenides (TMCs), especially cuprasulfide (Cu_2S), is promising as it demonstrates stronger binding of ECO_2RR intermediates thus a lower overpotential and higher current density than Bi.[30-31] However, HER is inevitable in Cu_2S systems.

Herein, we report proof-of-concept experimental and theoretical design of interfacial sites with a selectivity-governing and HER-suppressing domain (Bi) in concomitant with an electrokinetic-promoting domain (Cu_2S) for efficient ECO_2RR to formate. We developed a one-pot solution-phase synthesis method for preparing a new class of heterostructured Bi-Cu_2S nanocrystals with a microphone-like morphology. In 0.1 M $KHCO_3$, the Bi-Cu_2S catalyst manifests a much higher current density, lower overpotential, and higher FE toward formate production than its single component (Bi, Cu_2S) counterparts for ECO_2RR. Compared with Bi nanoparticles (NPs), the ECO_2RR onset potential on Bi-Cu_2S is positively shifted by 240 mV. By controlling the synthesis conditions, *e.g.*, the reaction temperature, the amount of reducing agent, and degassing temperature, the optimal Bi-Cu_2S catalyst can achieve near-unity formate selectivity at -1.2 V (*vs.* reversible hydrogen electrode, RHE) with a high current density of 18.2 mA cm^{-2}, outperforming many previously reported catalysts.[32-34] Density functional theory (DFT) calculations showed that the interfacial site preferentially stabilizes the formate-evolution intermediate *OCHO compared with the *COOH intermediate toward CO formation and the *H

intermediate toward H_2 generation. The stabilization of key intermediates was attributed to the electron transfer from Bi to Cu_2S moieties at the interface.

2.2 Materials and methods

2.2.1 Synthesis of heterostructured Bi-Cu_2S nanocrystals

To fabricate Bi-Cu_2S heterostructure, 1 mmol of $Bi(ac)_3$, 1 mmol $Cu(acac)_2$, and 9.5 ml OAm were added into a 50 mL four-necked flask under magnetic stirring. The mixture was heated to 140 °C and kept at this temperature for 2 h under nitrogen (N_2) flow to remove dissolved moisture and oxygen. Then the mixture was heated to 220 °C at a ramping rate of 7 °C min^{-1}, while 0.5 mL OAm and 0.24 mL DDT were well-mixed and injected into the solution to induce the formation of sulfide. The reaction solution was kept at this temperature for 30 min. After being cooled to room temperature, the product was collected and purified by excessive ethanol by centrifuging at 800 rpm for 1 min to remove the remaining precursor and impurities. The product was further centrifuged at 5500 rpm for 5 min and washed twice with ethanol and redispersed in hexane for further use.

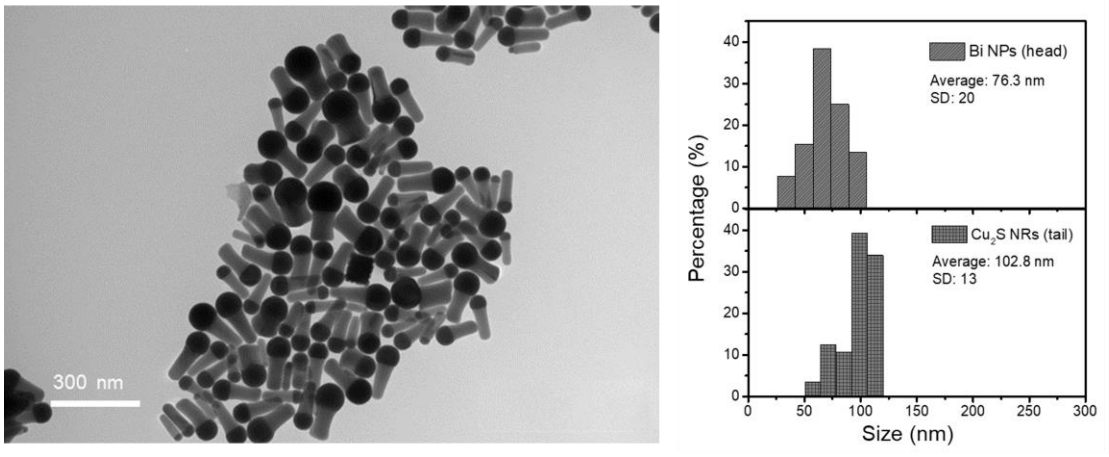

Figure 2.1. The low magnification TEM image and size distribution with average size and standard deviation (SD) of Bi-Cu_2S nanocrystals.

2.2.2 Synthesis of Bi NPs

The synthesis procedure of Bi NPs was similar to a previously reported method.[35] Typically, 1 mmol bismuth neodecanoate was mixed with 10 mL Tetralin and heated to 110 °C and incubated for 30 min under the N_2 flow. The solution then cooled down to 80 °C, while 0.24 mL DDT was injected into the solution. After the DDT injection, 1 mL TOP was injected into the solution and the system was further cooled down to 70 °C and kept at this temperature for 30 min. The final products were collected and centrifuged, followed by washing with ethanol for 3 times.

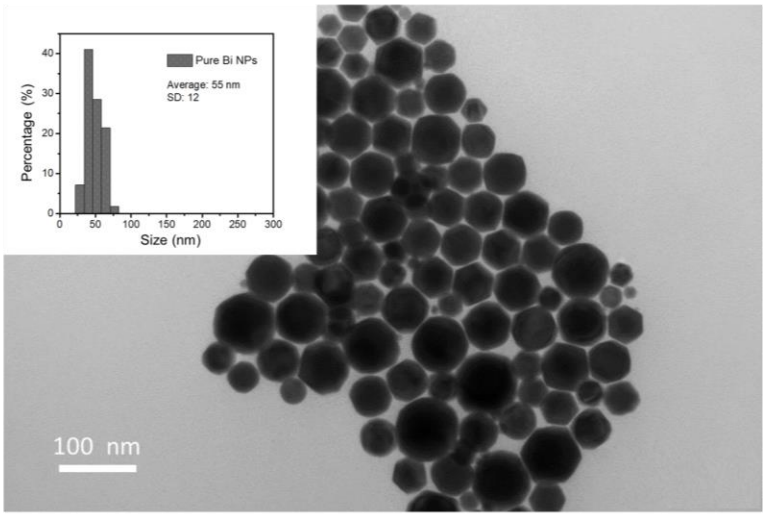

Figure 2.2. TEM images and size distribution with average size and standard deviation (SD) of Bi NPs.

2.2.3 Synthesis of Cu_2S NRs

The synthesis procedure of Cu_2S NRs was similar to a previously reported method.[36] 0.5 mmol $Cu(acac)_2$, 2.5 mmol TOPO were mixed with 10 mL ODE and heated up to 80 °C

and kept there for 30 min under the N_2 flow. Then, the mixture was heated up to 180 °C in 5 min while 2.5 mL t-DDT was injected at 120 °C. The reaction solution was kept at 180 °C for 15 min. The final products were collected and centrifuged, followed by washing with ethanol for 3 times.

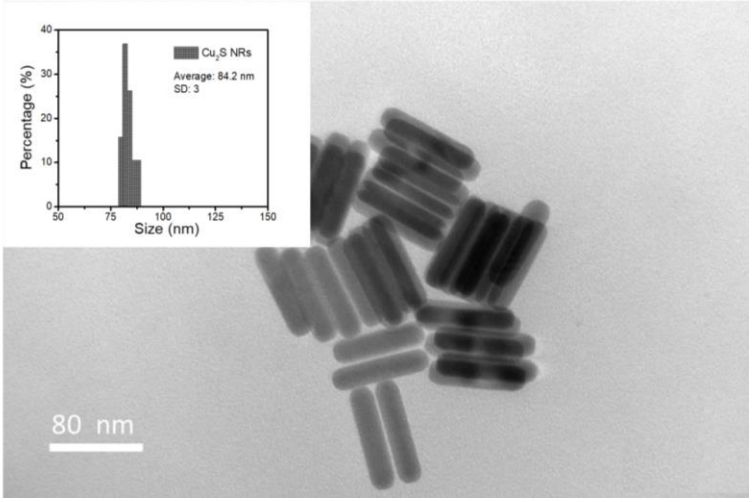

Figure 2.3. TEM images and size distribution with average size and standard deviation (SD) of Cu_2S nanorods.

2.2.4 The physical mixture of Bi NPs and Cu_2S NRs

7.5 mg Bi NPs and 2.5 mg Cu_2S NRs were weighed and mixed in the hexane. The mixture was sonicated for 2 h and then stirred overnight to achieve a homogeneous solution. The product was then centrifuged and redispersed in hexane for further use.

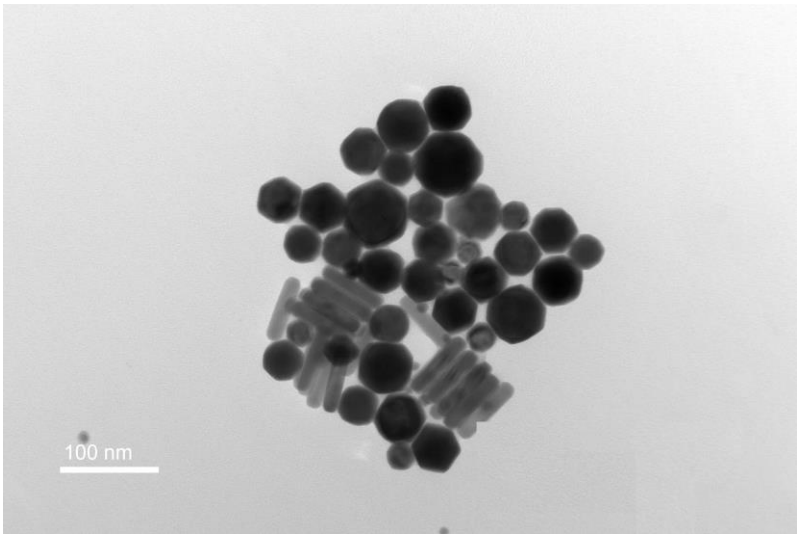

Figure 2.4. The TEM image of the physical mixture of Bi NPs and Cu_2S NRs.

2.2.5 Characterization

The morphology and sizes of the Bi-Cu_2S heterostructures, Bi NPs, and Cu_2S NRs were characterized by the transmission electron microscopy (TEM) on Philips EM420 operated at 120 kV. High-resolution TEM (HRTEM), high-angle annular dark-field scanning TEM (STEM-HAADF), X-ray energy dispersive spectroscopy (X-EDS) and EDS mapping were conducted on a JEOL ARM 200CF equipped with an Oxford Instrument X-ray Energy Dispersive Spectrometer. X-ray diffraction (XRD) patterns were collected by a Philips X'Pert Pro Super with Cu Kα (λ=1.5406 Å). The X-ray photoelectron spectroscopy (XPS) was collected on a PHI Versa probe III microscopy with Al Kα monochromatic energy source at 1486.6 eV. Inductively coupled plasma optical emission spectroscopy (ICP-OES) was performed for the quantitative analysis of the elemental contents on a SPECTRO GENESIS ICP spectrometer.

2.2.6 Catalyst preparation and surfactant removal

To load Bi-Cu_2S on carbon (Bi-Cu_2S/C), 10 mg as-synthesized Bi-Cu_2S heterostructures were sonicated with 40 mg activated carbon (Vulcan XC-72R) in hexane for 2 h. The products were then collected by centrifugation at 8500 rpm for 5 min. The removal of organic ligands was achieved by immersing the catalysts in a mixture of 1.5 mL hydrazine and 18.5 mL ethanol overnight and washing with excessive ethanol twice. The final products were dried for 4 h in the vacuum oven at 50 °C. The Bi/C, Cu_2S/C, and Bi+Cu_2S/C were also prepared following the same procedure.

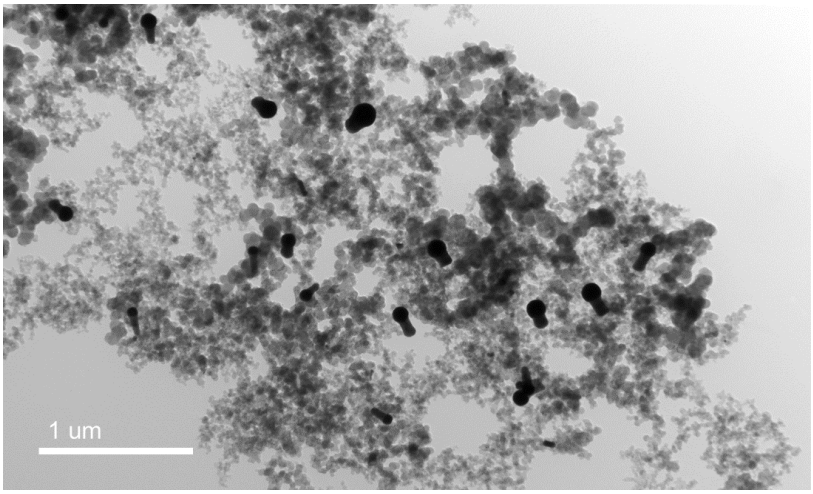

Figure 2.5. The TEM image of Bi-Cu_2S loaded on carbon black.

2.2.7 Electrochemical measurements and product analysis

Electrochemical measurements were all carried out in 0.1 M $KHCO_3$. To prepare the working electrode, 10 mg of Bi-Cu_2S/C catalyst powder was mixed with 2 mL isopropanol and 40 μL of Nafion solution (5 wt%, Sigma-Aldrich) by sonicating for 30 min to achieve a homogeneous catalyst ink. This catalyst ink was then airbrushed onto a carbon paper with an area of 1x1 cm^2 and was naturally dried before use. The loading amount was calculated

by weighing the carbon paper before and after the airbrushing, achieving the Bi-Cu_2S/C loading of 1 mg cm^{-2}. All the potentials were controlled via a Biologic electrochemical workstation. The H-type gas-tight cell was separated by a Nafion (117) membrane, and each compartment contained a 40 mL electrolyte. The cathodic compartment was housed the working electrode and the reference electrode (Ag/AgCl, 3.5 M KCl), while the anodic compartment contained a platinum foil as the counter electrode. Cyclic voltammograms (CVs) were recorded in Ar-saturated 0.1 M $KHCO_3$ between -1.8 V and -0.6 V vs. Ag/AgCl after 10 cycles with a scan rate of 20 mV s^{-1} at room temperature and then recorded in CO_2-saturated electrolyte under the same condition. Linear sweep voltammograms (LSVs) were measured from -0.6 V to -1.8 V vs. Ag/AgCl with a scan rate of 20 mV s^{-1} in CO_2-saturated 0.1 M $KHCO_3$. Chronoamperometry (CA) measurements were performed at each potential from -1.4 V to -1.8 V vs. Ag/AgCl for 1 h in the H-type cell system. All the potentials were then converted to the reversible hydrogen electrode (RHE) reference scale by the following equation:

$$E(vs.RHE) = E(vs.Ag/AgCl) + 0.21\,V + 0.0591 \times pH$$

Before the test, the catholyte was purged with CO_2 for 30 min to remove residual air. Then, a consistent CO_2 flow was introduced to the cathodic compartment at a flow rate of 10 sccm during the electrolysis. The gaseous products were analyzed *via* online gas chromatography (GC, Agilent 7890 B). After the electrochemical reactions, the cathodic electrolyte was collected to analyze the liquid products by nuclear magnetic resonance spectroscopy (NMR, Bruker Avance II 500Hz).

2.2.8 The calculation of Faradic efficiency

The Faradic efficiency (FE) of gas products were calculated by:

$$J_{CO} = \frac{A}{\alpha} \times V_{CO_2} \times \frac{2Fp_0}{RT} \times (Electrode\ area)^{-1}$$

$$J_{H_2} = \frac{B}{\beta} \times V_{CO_2} \times \frac{2Fp_0}{RT} \times (Electrode\ area)^{-1}$$

where α and β are the conversion factors based on the calibration of the GC with the standard samples of CO and H_2, respectively. V_{CO_2} is the flow rate of CO_2 (10 sccm); F is the Faradic constant (96485 C mol^{-1}); p_0 is the pressure (1 atm); T is the temperature (273 K); R is the gas constant (82.1 mL atm K^{-1} mol^{-1}); A and B are the peak areas of CO and H_2 obtained from GC. FE for the various gas products was obtained by dividing the partial current density by the total current density. [37-38]

The liquid product was analyzed by NMR. To prepare the NMR sample, 0.5 mL electrolyte containing the liquid product ($HCOO^-$) was mixed with 0.1 mL D_2O and 0.1 mL 0.1 M 3-(trimethylsilyl) propionic-2,2,3,3-d_4 acid sodium salt (internal standard). The FE of liquid-phase product was calculated by:

$$FE_{HCOO^-}(\%) = \frac{2nF}{It} \times 100$$

where n is the moles of formate, calculating from the calibration curve of the NMR. F is the Faradic constant (96485 C mol^{-1}). I is the applied current (A) and t is the electrolysis time (s). The error bars in the figures are based on the average value of three repeated experiments. The production rate of formate over Bi-Cu_2S and Bi was calculated after 1 h electrolysis at each given potential.

2.3 Results and discussion

2.3.1 Heterostructured Bi-Cu_2S nanocrystals

Heterostructured Bi-Cu_2S nanocrystals were synthesized *via* a one-pot wet chemical approach**.** The TEM images of the as-synthesized Bi-Cu_2S (**Figure 2.1, and Figure 2.6a, 6b**) show that the Bi 'head' with a size of 76 nm and the 103 nm Cu_2S 'body' is well-connected, forming a heterostructure interface. A clear interfacial boundary was observed in a bright-field (BF) STEM image (**Figure 2.6d**), suggesting the epitaxial growth between Cu_2S and Bi. From the STEM image, we can observe an interplanar distance of 3.3 Å in the Bi domain, corresponding to the (012) crystalline plane of rhombohedral Bi. The lattice spacing of Cu_2S is 3.4 Å, which can be attributed to the (002) plane of hexagonal Cu_2S. High-angle annular dark-field STEM (HAADF-STEM) (**Figure 2.6c**) x-ray energy dispersive spectrometry (X-EDS) mapping (**Figure 2.6e**) suggests the enrichment of Bi at the head while the signal of Cu and S distributes across the entire structure and enriches in the rod, confirming the formation of abundant Bi-Cu_2S interfacial sites.

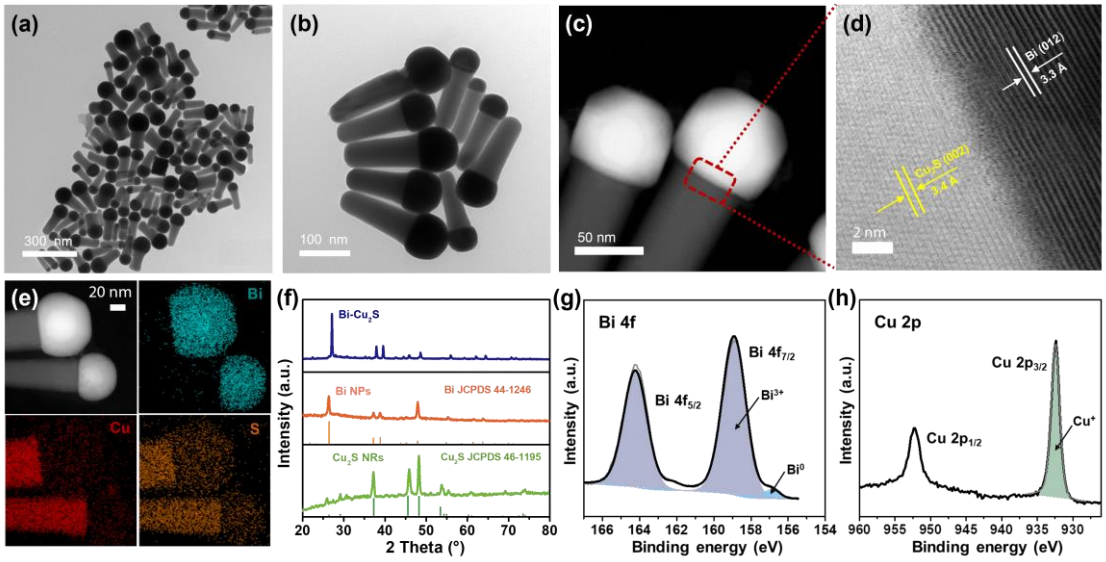

Figure 2.6. Structural characterizations of heterostructured Bi-Cu_2S nanocrystals. (a)-(b) TEM images; (c) STEM-HAADF image and (d) BF-STEM image of Bi-Cu_2S. (e) The STEM-HAADF image and the corresponding X-EDS mappings of Bi-Cu_2S. (f) XRD patterns of Bi NPs, Cu_2S NRs and Bi-Cu_2S. (g) Bi 4f XPS spectrum and (h) Cu 2p XPS spectrum of Bi-Cu_2S.

Figure 2.7a shows a schematic illustration of the nucleation and growth of heterostructured Bi-Cu_2S nanocrystals. The transmission electron microscopy (TEM) images of Bi-Cu_2S along the time sequence after the injection of sulfur-containing surfactants suggest that the Bi nucleates first and serves as seeds for the deposition, nucleation, and growth of Cu_2S domains (**Figure 2.7b**). For comparison, Bi NPs and Cu_2S nanorods (NRs) were also synthesized according to reported methods.[12, 36] A typical rhombohedral crystal structure of Bi-Cu_2S and Bi and a hexagonal structure of Cu_2S in the x-ray diffraction (XRD) patterns were observed (**Figure 2.6f**), consistent with the lattice spacing obtained in **Figure 2.6d**. No obvious Cu_2S peak presents in the Bi-Cu_2S due to the overlapping of diffraction peaks between Bi and Cu_2S.

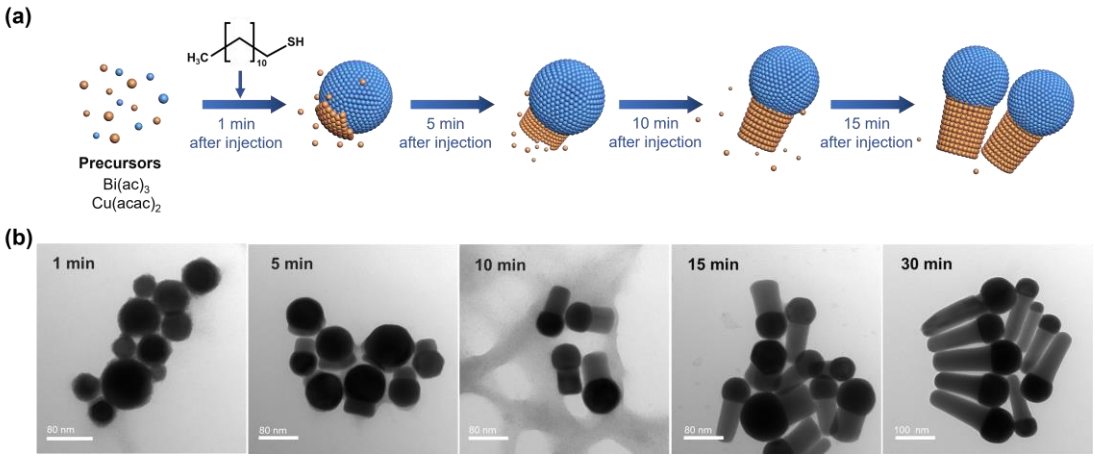

Figure 2.7. (a) Schematic illustration of the nucleation and growth of the heterostructured Bi-Cu_2S nanocrystals. (b) TEM images of Bi-Cu_2S at different time intervals after introducing 1-dodecanethiol at 220 °C.

The x-ray photoelectron spectroscopy (XPS) of Bi 4f spectrum for Bi-Cu_2S (**Figure 2.6g**) shows the peaks at 156.93 and 158.91 eV, which are attributed to Bi^0 and Bi^{3+}, respectively. Compared to the XPS result of pure Bi NPs (**Figure 2.10b**), Bi-Cu_2S has no peak shifted, suggesting the chemical composition and valence state of Bi-Cu_2S in the bulk keep unchanged. The Cu 2p XPS spectrum of Bi-Cu_2S (**Figure 2.6h**) shows a single Cu $2p_{3/2}$ feature at 932.3 eV, which can be assigned to Cu^{1+} or Cu^0. The deconvolution of the Cu LMM spectra (**Figure 2.9**) further distinguishes the existence of Cu^{1+} from Cu^0 in Bi-Cu_2S.

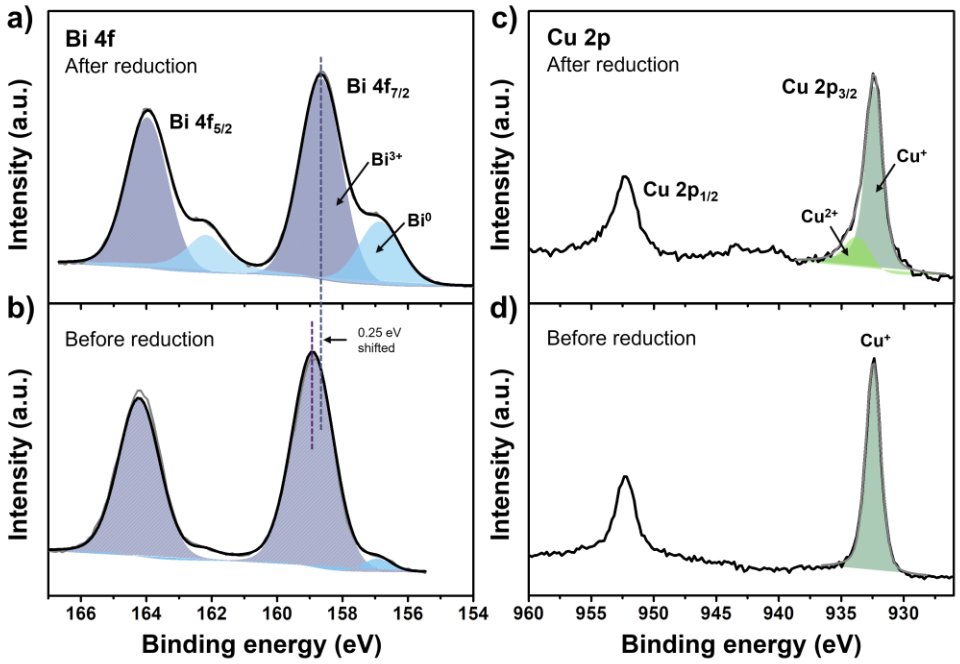

Figure 2.8. Bi 4f XPS spectra of Bi-Cu_2S after (a) and before (b) the ECO_2RR; Cu 2p XPS spectra of Bi-Cu_2S after (c) and before (d) the ECO_2RR.

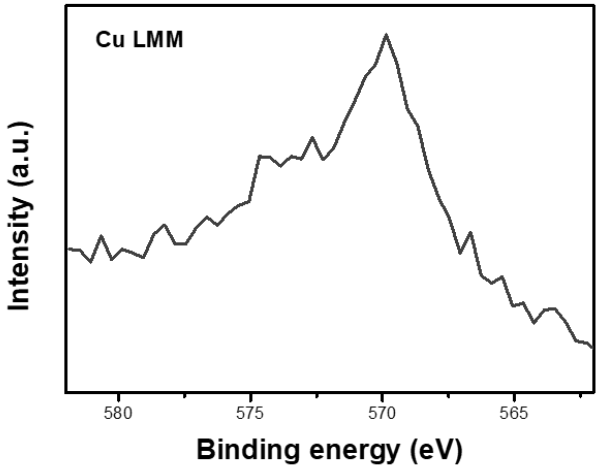

Figure 2.9. XPS Cu LMM Auger spectrum of Bi-Cu_2S.

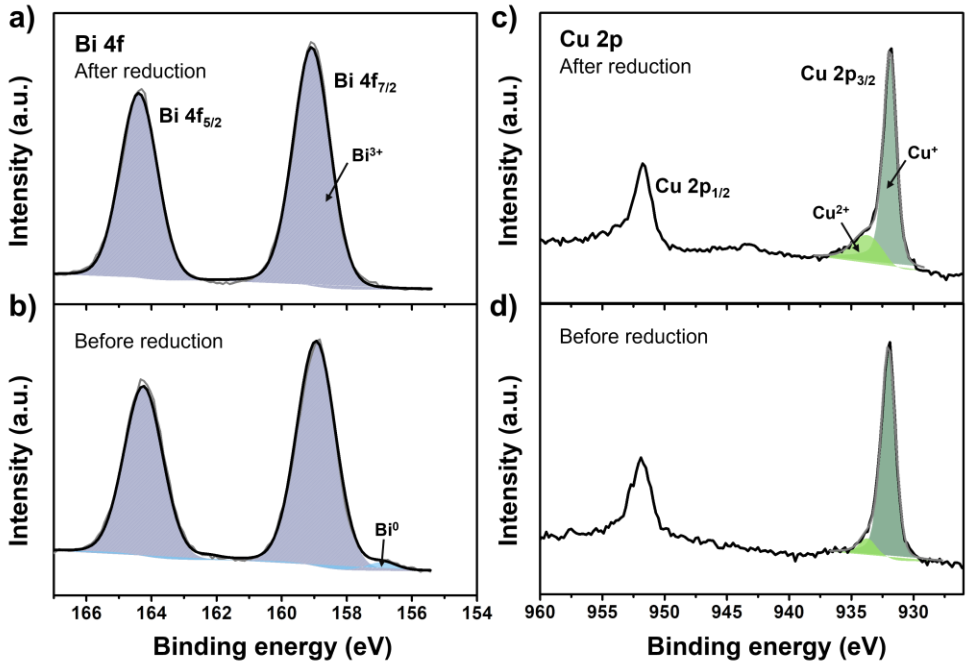

Figure 2.10. Bi 4f XPS spectra of Bi NPs **(a)** after the ECO_2RR measurement and **(b)** before the ECO_2RR measurement; Cu 2p XPS spectra of Cu_2S NRs **(c)** after the ECO_2RR measurement and **(d)** before the ECO_2RR measurement.

2.3.2 Electrocatalytic activity of Bi-Cu_2S in ECO_2RR

The as-synthesized Bi-Cu_2S and control samples of Bi NPs and Cu_2S NRs (**Figure 2.2, 2.3**) were deposited on activated carbon and surface-activated through a ligand-stripping method (**Figure 2.5**). The catalyst ink was prepared and airbrushed onto a carbon paper. The ECO_2RR testing was conducted in CO_2-saturated 0.1 M $KHCO_3$ in a gas-tight H-cell. Before the measurement, all the samples were further activated *via* potential cycling between -1.2 V and 0 V vs. RHE in Ar-saturated solution for 10 cycles at a scan rate of 20 mV s^{-1}. Cyclic voltammograms (CVs) were then recorded first in Ar and then in CO_2-saturated solutions (**Figure 2.11, 2.12, 2.13**).

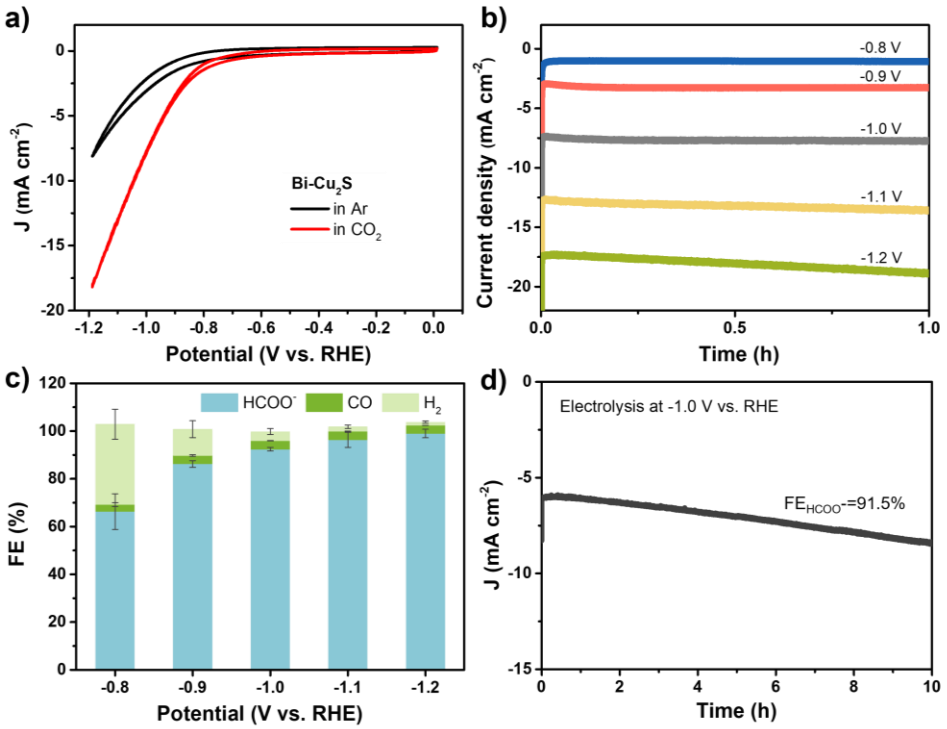

Figure 2.11. The ECO_2RR performance on Bi-Cu_2S catalyst: a) CV curves in Ar-saturated (black line) and CO_2-saturated (red line) 0.1 M $KHCO_3$ normalized to geometric area. b) Current density over 1 h of electrolysis at each given potential (-0.8 to -1.2 V vs. RHE). c) FE for ECO_2RR at various applied potentials. d) Durability test at -1.0 V for 10 h.

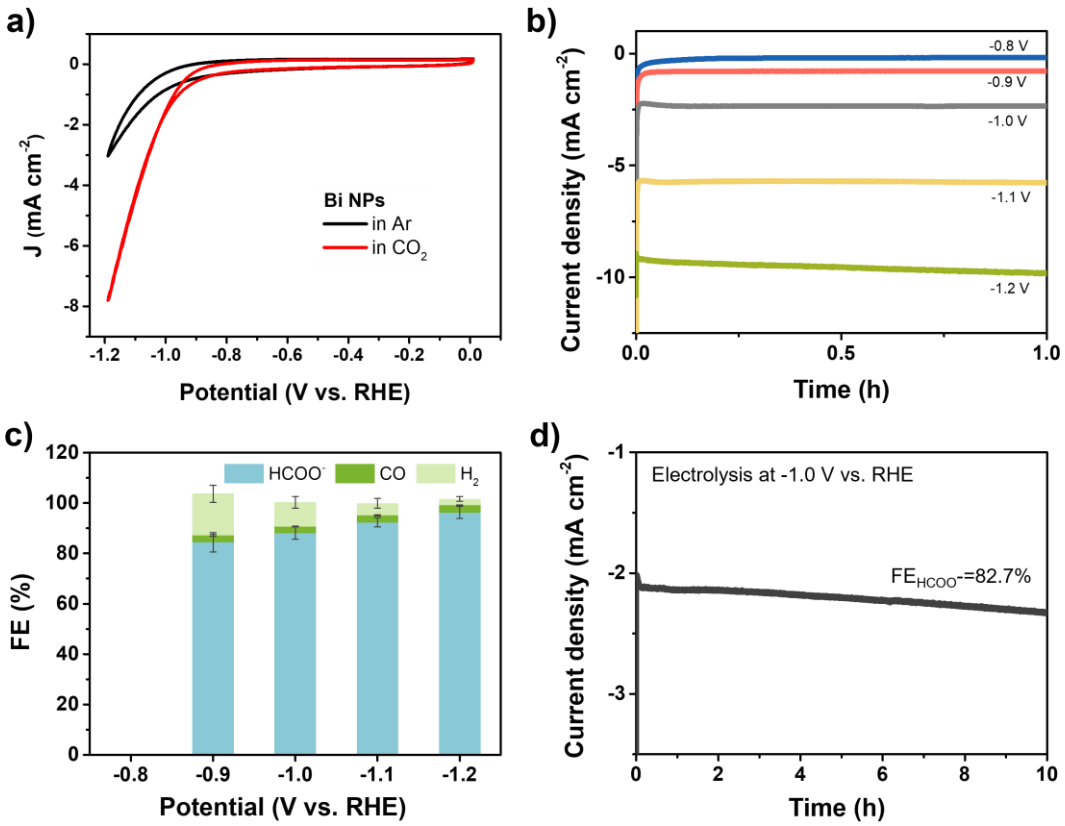

Figure 2.12. The ECO_2RR performance on Bi NPs: **a)** CV curves in Ar-saturated (black line) and CO_2-saturated (red line) 0.1 M $KHCO_3$ normalized to geometric area. **b)** Current density over 1 h of electrolysis at each given potential (-0.8 to -1.2 V vs. RHE). **c)** FE for ECO_2RR at various applied potentials. **d)** Durability test at -1.0 V for 10 h.

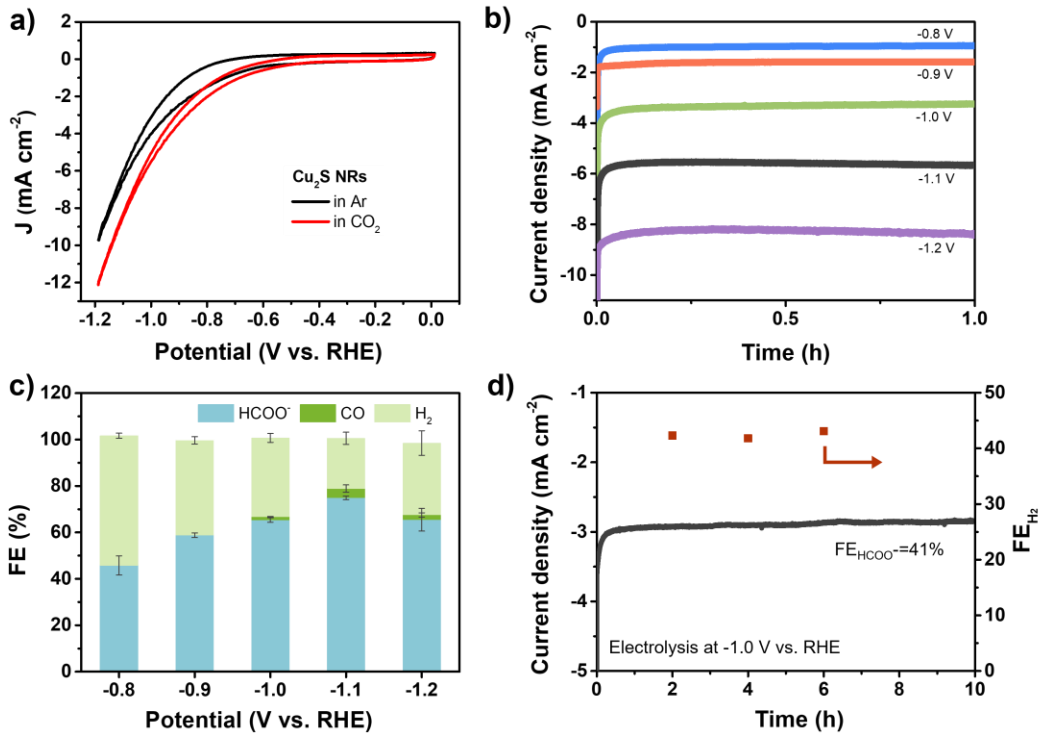

Figure 2.13. The ECO_2RR performance on Cu_2S NRs: **a)** CV curves in Ar-saturated (black line) and CO_2-saturated (red line) 0.1 M $KHCO_3$ normalized to geometric area. **b)** Current density over 1 h of electrolysis at each given potential (-0.8 to -1.2 V vs. RHE). **c)** FE for ECO_2RR at various applied potentials. **d)** Durability test at -1.0 V for 10 h.

To further evaluate the catalytic performance of Bi-Cu_2S, linear sweep voltammetry (LSV) curves were performed. In **Figure 2.15a**, Bi-Cu_2S not only shows a higher current density than the two control samples (Bi NPs and Cu_2S NRs) in a wide range of potential from -0.8 V to -1.2 V *vs.* RHE, but also demonstrates ~240 mV more positive onset potential than Bi. At -1.0 V *vs.* RHE, Bi-Cu_2S demonstrates a 4.9-fold increase of total current density compared with Bi. To probe the product distribution, the electrolysis measurements in a wide range of applied potentials (-0.8 to -1.2 V) were carried out. Gas

chromatography (GC) was used to detect gas products, while ^{1}H nuclear magnetic resonance (NMR) spectrometer was employed to analyze liquid-phase products. The Bi-Cu_2S demonstrated the highest partial current density for formate production (J_{HCOO^-}) at all applied potentials compared with Bi NPs and Cu_2S NRs (**Figure 2.15b**). Meanwhile, the J_{HCOO^-} of Bi-Cu_2S rapidly increased from -0.9 V, exhibiting a striking difference from the control samples. The FE of formate production (FE_{HCOO^-}) on Bi-Cu_2S is shown in **Figure 2.11c**. Over 90% of FE_{HCOO^-} was achieved at the applied potential of -1.0 V. Especially, near-unity $HCOO^-$ selectivity was obtained at the potential of -1.2 V, exceeding most of the state-of-art catalysts for formate production.[7, 19] **Figure 2.15e** shows the FEs over Bi-Cu_2S, Bi, and Cu_2S. The FE_{HCOO^-} of the designed Bi-Cu_2S was higher than the two control samples at all applied potentials. Especially, the FE_{HCOO^-} of Bi-Cu_2S was 92.4% at -1.0 V, which is ~1.4 times higher than the Cu_2S NRs (65% FE_{HCOO^-}). The production rate of formate on Bi-Cu_2S reached 131 μmol cm^{-2} h^{-1} at -1.0 V, which is 3.5 times higher than the Bi NPs (**Figure 2.14**). Furthermore, Bi-Cu_2S showed a much lower FE of H_2 (FE_{H2}), indicating that Bi-Cu_2S preserved the HER-inhabiting property.

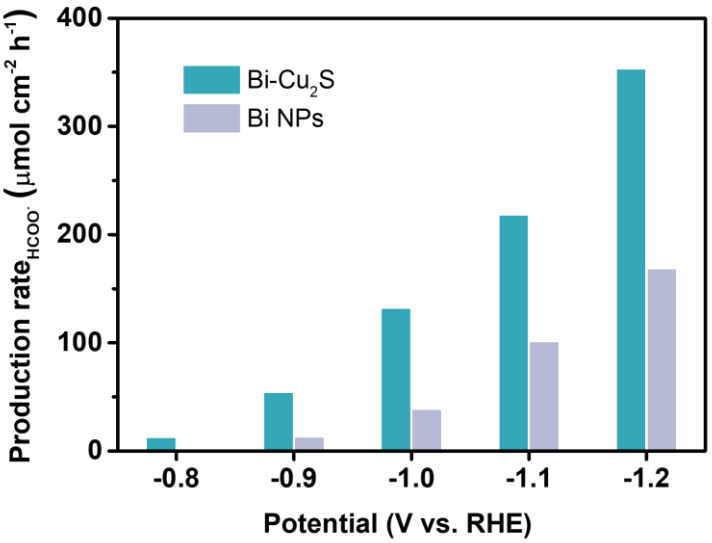

Figure 2.14. The production rate of formate from ECO_2RR on Bi-Cu_2S and Bi at various potentials.

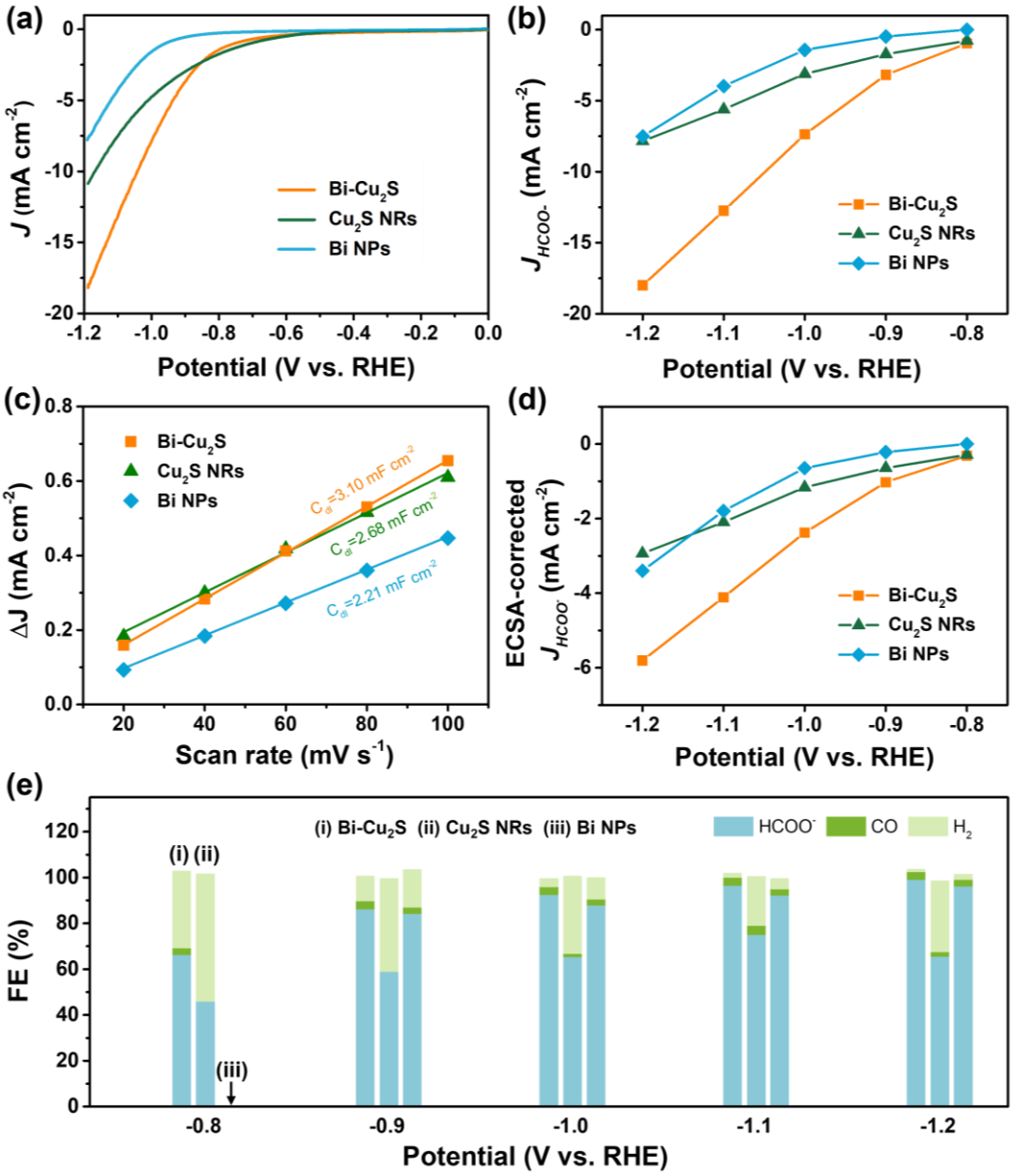

Figure 2.15. ECO_2RR on Bi-Cu_2S, Cu_2S NRs, and Bi NPs in the CO_2-saturated 0.1 M $KHCO_3$ electrolyte: **(a)** LSV curves; **(b)** Partial current density of formate at different potentials. **(c)** ECSAs of Bi-Cu_2S, Cu_2S NRs and Bi NPs. **(d)** ECSA-corrected current densities for formate. **(e)** Comparison of FEs for ECO_2RR on Bi-Cu_2S, Bi and Cu_2S electrodes at various applied potentials.

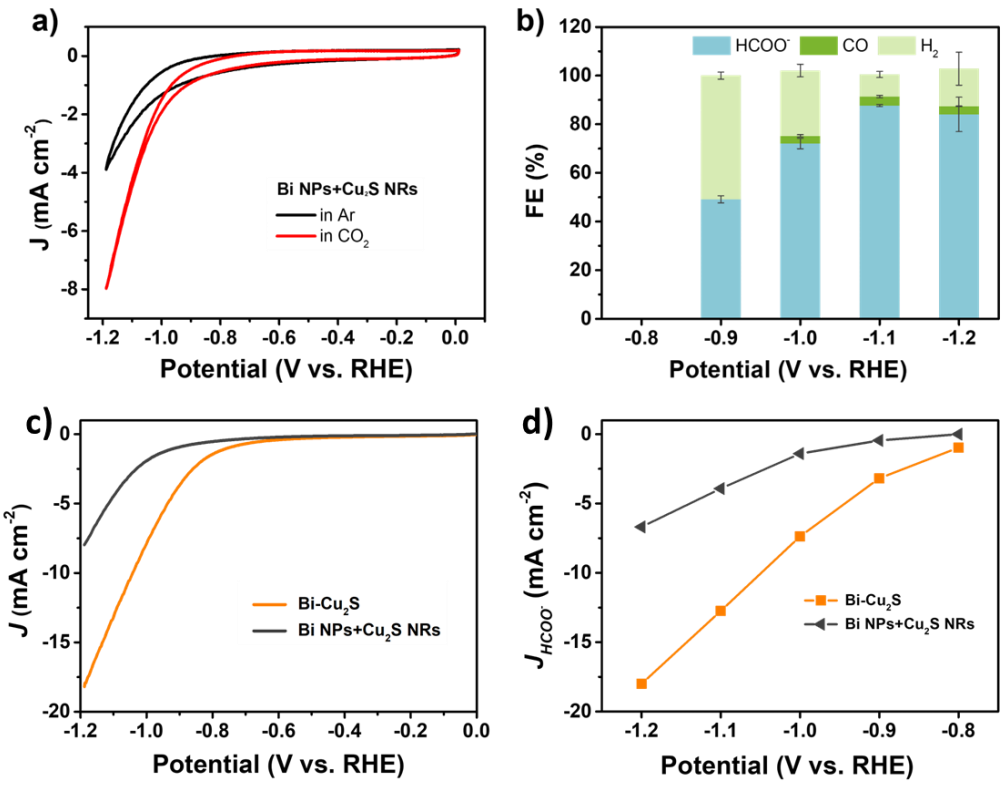

Figure 2.16. The ECO2RR performance on the mixture of Bi NPs and Cu_2S NRs (Bi NPs+Cu_2S NRs): (a) CV curves in Ar-saturated (black line) and CO_2-saturated (red line) 0.1 M $KHCO_3$ normalized to geometric area. (b) Total FE for ECO_2RR at various applied potentials. c) LSV of Bi-Cu_2S, and Bi NPs+Cu_2S NRs mixed sample. d) Partial current density of formate obtained on Bi-Cu_2S and Bi NPs+Cu_2S NRs mixed sample at different potentials.

2.3.3 The role of interficial sites on Bi-Cu_2S

To verify that the interfacial sites of Bi-Cu_2S play a key role in the ECO_2RR, Bi NPs and Cu_2S NRs were physically mixed (Bi NPs+Cu_2S NRs) as a control sample. Compared with the physical mixture of Bi NPs and Cu_2S NRs (**Figure 2.16**), Bi-Cu_2S showed a larger current density and higher FE_{HCOO-}, indicating the importance of a well-connected interface on Bi-Cu_2S in optimizing the ECO_2RR kinetics.

Moreover, we tested the activity of Bi-Cu_2S heterostructures with 5-, 15-, 30-, and 120-minutes reaction time after injecting the sulfur-containing surfactant, denoted as Bi-Cu_2S/5, Bi-Cu_2S/15, Bi-Cu_2S/30 (which is the Bi-Cu_2S catalyst we mentioned in this work), and Bi-Cu_2S/120. The TEM images show that there are many impurities and unreacted precursors in the Bi-Cu_2S/5 and Bi-Cu_2S/15. The reaction is complete and there are no more impurities in the sample when the reaction time is more than 30 min. In **Figure 2.17**, Bi-Cu_2S under complete reaction conditions (Bi-Cu_2S/30 and Bi-Cu_2S/120) demonstrate more positive onset potentials than the incomplete ones (Bi-Cu_2S/5 and Bi-Cu_2S/15). Bi-Cu_2S/30 shows the highest partial current density (J_{HCOO-}) and Faradic efficiency of formate (FE_{HCOO-}) production at the potential from -0.9 to -1.2 V vs. RHE. Especially, Bi-Cu_2S/30 demonstrates a much higher J_{HCOO-} and FE_{HCOO-} than the Bi-Cu_2S/5 and Bi-Cu_2S/15, indicating the negative impact of the incomplete reactants in the CO_2 reduction reaction. Furthermore, both J_{HCOO-} and FE_{HCOO-} on B-Cu_2S/120 catalysts slightly decrease compared to Bi-Cu_2S/30. This can be attributed to the larger size and fewer active sites of Bi-Cu_2S/120. This result provides evidence that the interfacial synergy in Bi-Cu_2S plays an important role in promoting electrocatalysis. Taking cumulatively, Bi-Cu_2S/30 demonstrates an extremely high $HCOO^-$ selectivity, improved current density, and a much

lower overpotential due to the synergistic effect at the interfacial sites of Bi-Cu_2S. The durability test of Bi-Cu_2S (**Figure 2.11d**) showed that the current density and FE stay stable after 10 h electrolysis.

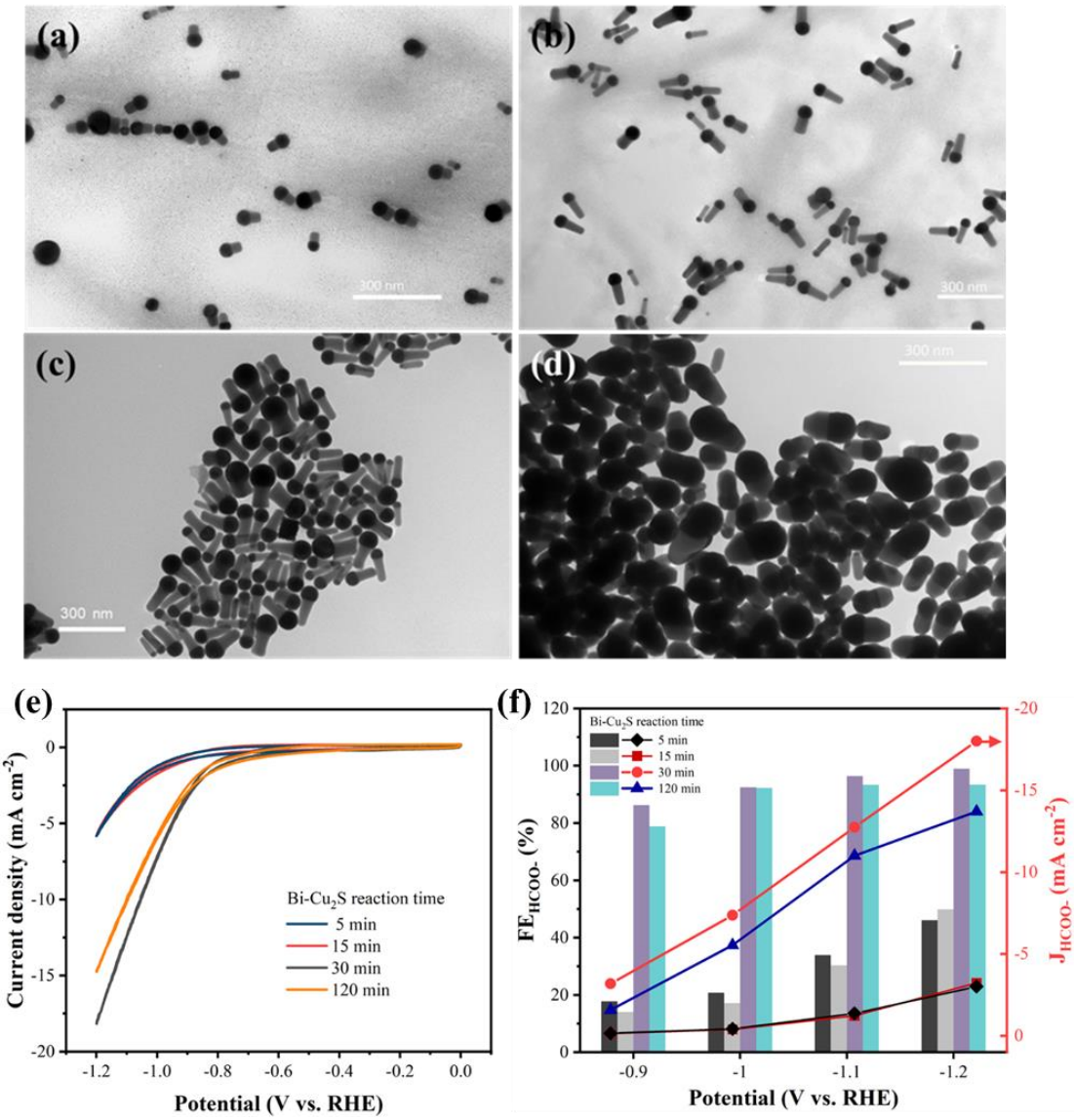

Figure 2.17. TEM images of Bi-Cu_2S heterostructures with different reaction time: a) 5 min; b) 15 min; c) 30 min; d) 120 min. Corresponding electrocatalytic activities of CO_2 reduction with different reaction time in the CO_2-saturated 0.1 M $KHCO_3$ electrolyte: (e) CV curves; (f) Partial current density and FE on formate production at different potentials.

2.3.4 Intrinsic activity of Bi-Cu_2S

To gain insight into the origin of the ECO_2RR enhancement on Bi-Cu_2S, electrochemical surface area (ECSA) was measured by calculating double-layer capacitance (C_{dl}) to evaluate their ECSA-corrected current density (**Figure 2.18, 2.19**). The calculated values of C_{dl} (**Figure 2.15c**) for Bi-Cu_2S, Bi, and Cu_2S are 3.1, 2.675, and 2.11 mF cm^{-2}, respectively, indicating Bi-Cu_2S has more active sites than the controls. Meanwhile, the normalized ECSA current of formate (**Figure 2.15d**) shows that Bi-Cu_2S has higher intrinsic activity than Bi NPs and Cu_2S NRs at all applied potentials. The XPS was performed before and after the ECO_2RR to gain a deeper insight into the valence state and surface composition of the Bi-Cu_2S catalyst. In the Bi 4f XPS spectra of pure Bi NPs (**Figure 2.10**), only Bi^{3+} peak is observed, indicating Bi is surface-oxidized when re-exposure into the air after the CO_2 reduction. On the contrary, the XPS results of Bi-Cu_2S (**Figure 2.8**) reveal that Bi partially keeps the metallic state and the Bi^0/Bi^{3+} ratio increases from 1:26 to 1:3 before and after the ECO_2RR. This observation suggests that the existence of Cu_2S stabilizes metallic Bi and suppresses its surface oxidation upon air exposure to promote ECO_2RR.[12]

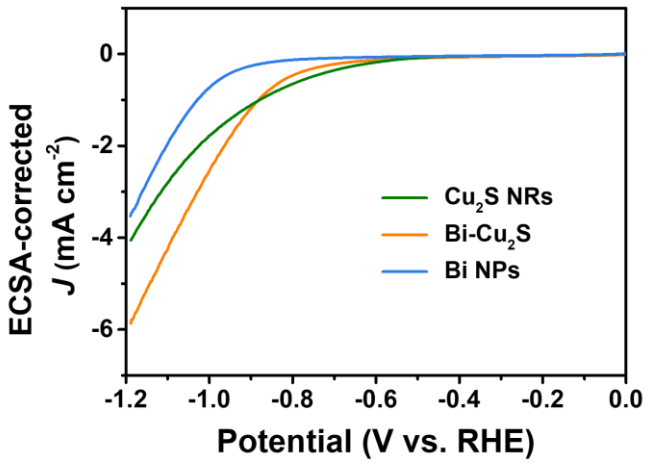

Figure 2.18. ECSA-corrected total current densities on Bi-Cu_2S, Cu_2S NRs, and Bi NPs.

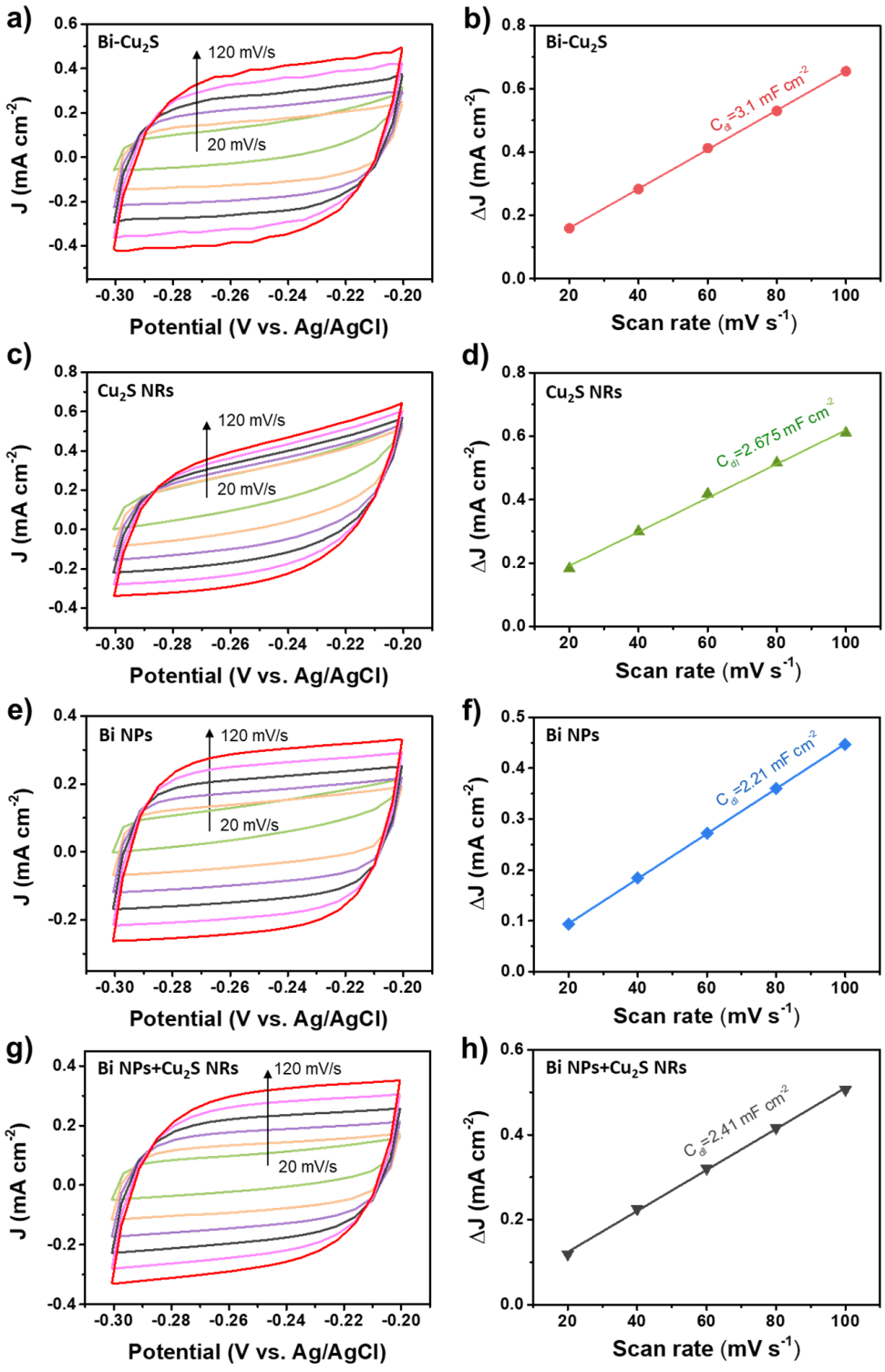

Figure 2.19. Electrochemical surface area (ECSA) measured by CV cycling in Ar-saturated 0.1 M $KHCO_3$, and their linear fitting for **a) b)** Bi-Cu_2S; **c) d)** Cu_2S NRs; **e) f)** Bi NPs; **g) h)** The mixture of Bi NPs and Cu_2S NRs (Bi NPs + Cu_2S NRs).

2.3.5 Theoretical calculation

2.3.5.1 DFT calculation

All density functional theory (DFT) calculations were performed using Vienna Ab initio Simulation Package (VASP), interfaced with the Atomic Simulation Environment. The ion-electron interactions were described by the projector-augmented plane-wave approach. The Perdew-Burke-Ernzerhof generalized gradient approximation was selected as the description of the exchange and correlation interactions. In this work, two model systems including Bi (001) and Bi (001) with a Cu_2S nanorod were constructed. For both systems, Bi (001) was represented by 3 layers of a 3×3 supercell with a lattice parameter of a = b = 4.586 Å. For Bi-Cu_2S interfacial system, 3 layers of a 2×2 supercell of Cu_2S (100) slab with lattice parameters of a = 3.890 Å and c/a = 1.768 Å were used as a nanorod on top of the same Bi (001) substrate (**Figure 2.20**). All lattice parameters agree with experimental results and literature values within 1% error[39-40]. The adsorbates and top two layers including the Cu_2S clusters were fully relaxed until the energy and interatomic forces were minimized down to 1×10^{-5} eV and 0.03 eV/Å, respectively. The bottom four layers were fixed in their bulk positions. The slab was separated with 15 Å of vacuum space to avoid interactions in the periodic calculations in the z direction. The cutoff energy was 420 eV for plane-wave basis sets with Fermi-level smearing of 0.05 eV for slabs and 0.01 eV for gas species. Free formation energies were calculated as:

$$G = E_{DFT} + E_{ZPE} - TS$$

where E_{DFT}, E_{ZPE}, TS were electronic energy, zero-point energy, entropy contribution, respectively. For adsorbates, E_{ZPE} and S were determined by vibrational frequency

calculations, with all 3N degrees of freedom treated as harmonic vibrational motions (<50 cm^{-1} ones are replaced by 50 cm^{-1}). For molecules, all thermodynamic values were taken from the tabulated NIST database. DFT electronic energies for some molecules were corrected by combining with the experimental values since the inaccuracy of the PBE functional in describing these molecules[41-42]. $HCOO^-$(aq) energy is calculated directly from the experimental reduction potential of CO_2 to $HCOO^-$(aq), *i.e.*, -0.43 V vs. SHE at pH=7. The solvation effect on adsorbates was considered as an *ad hoc* effect and taken from literature values[43-44]. All contributions to the Gibbs free energy were provided in **Table 2.1**.

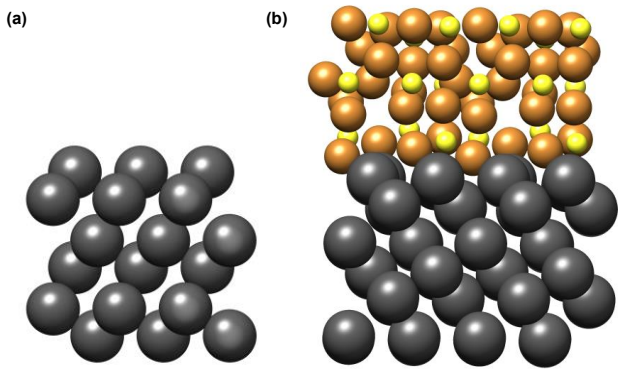

Figure 2.20. Front view of **(a)** Bi (001) surface and **(b)** Bi-Cu_2S interfacial model surface.

Table 2.1. Thermodynamics of free molecules and surface species[a]

Molecules	ZPE	-TS	Gas phase correction	Solvation
H_2(g)	0.27	-0.41	-	-
H_2O(g)	0.56	-0.67	-	-
CO_2 (g)	0.31	-0.66	0.17	-
H_2S (g)	0.40	-0.64	-	-
CO (g)	0.13	-0.61	-0.24	-
*H	0.14	-0.03		0.01
*COOH	0.59	-0.29		-0.29
*OCHO	0.59	-0.33		-0.23

[a]All values are in electronvolt (eV). Temperature was set to 298.15K.

The computational hydrogen electrode (CHE) model was employed to determine the free energy change of electrochemical elementary steps. All proton and electron transfers were assumed to be coupled. At 0 V vs RHE and 298.15 K, protons and electrons are at equilibrium with 1 bar of H_2 at arbitrary pH:

$$H^+ + e^- \rightarrow 1/2H_2$$

At any given potential U, the energy of e^- will be shifted by $-eU$.[45-46] For example, the free energy of the reaction:

$$CO_2 + H^+ + e^- \rightarrow * OCHO$$

would be calculated by:

$$\Delta G = G_{*OCHO} - G_{CO2} - [\frac{1}{2}G_{H2} - eU]$$

2.3.5.2 Cu_2S hypothetical structure

Cu_2S forms multiple phases depending on the reaction conditions. The synthesis temperature in this work is between 103℃ and 450℃, a hexagonal crystal structure also named as high chalcocite is generated. However, this high chalcocite structure is found to have a high mobility of Cu atoms and only sulfur atoms stay at lattice points of the hexagonal lattice. For simplicity of the modeling, a hypothetical structure used in previous studies[47] has been employed to model the nanorod on top of the Bi surface. The property of the hypothetical structure was confirmed to be consistent with the real structure[48]. The coordinates of elements in the Cu_2S unit cell and the crystal information are listed in **Table 2.2**, while the crystal structure is shown in **Figure 2.21**.

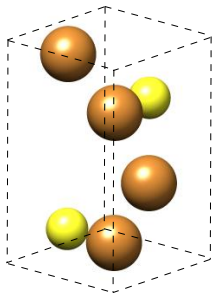

Figure 2.21. Cu_2S unit cell

Table 2.2. Cu_2S atomic coordinates

Elements	Coordinate (relative to unit cell)		
	x	y	z
S	1/3	2/3	1/4
Cu (1)	0	0	1/4
Cu (2)	1/3	2/3	0.578

2.3.5.3 Sulfur vacancy free formation energy

Sulfur vacancy free formation energy is calculated using a 2×2 supercell of Cu_2S (001) surface and is given by,

$$E_v^S = E(Defect\ surface) - E(Pristine\ surface) + E(H_2S) - E(H_2)$$

Where $E(Defect\ surface)$, $E(Pristine\ surface)$, $E(H_2S)$, $E(H_2)$ are the DFT total energies of the defect cell, pristine cell, H_2S molecule and H_2 molecule, respectively. The operating potential U vs. pH was plotted in **Figure 2.23b**. The red line is the potential U at which the vacancy starts to form. When the potential is more negative than the red line, the vacancy formation energy is negative which indicates the feasibility of losing sulfur atoms on the surface. The reaction operating conditions is plotted by the black line, starting from -1.21 V to -1.61 V vs. SHE at pH=7, and at this condition vacancies are formed on the surface.

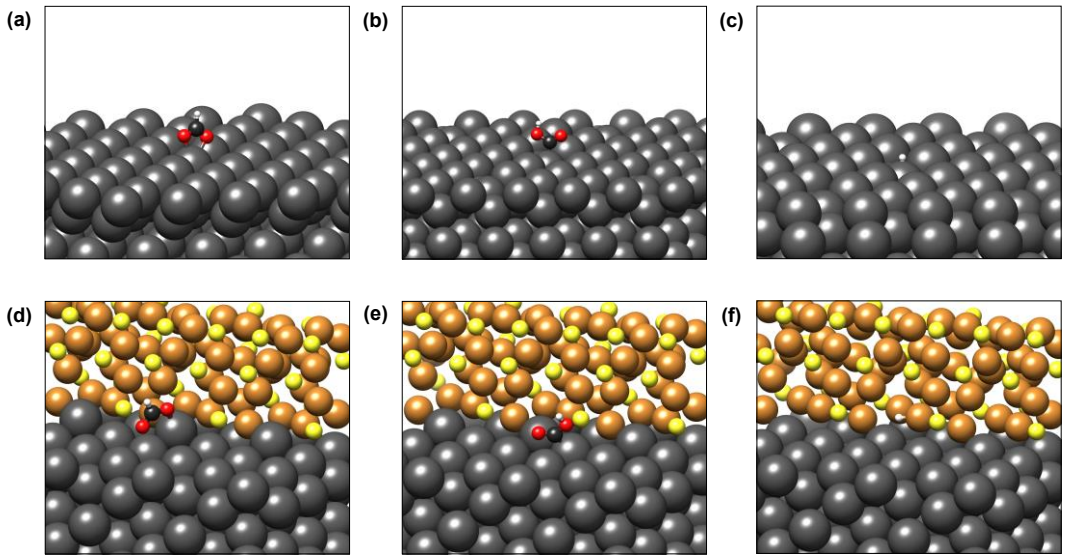

Figure 2.22. Adsorption geometries of **(a)** *OCHO, **(b)** *COOH, and **(c)** *H on Bi (001) surface, and adsorption geometries of **(d)** *OCHO, **(e)** *COOH, and **(f)** *H on Bi-Cu_2S interfacial system.

2.3.5.4 Charge density difference calculation

The charge density differences were generated by the differences for the charge density, ρ, of various systems with adsorbates (*OCHO, *COOH and *H) and two reference systems: a bare surface system and radicals of adsorbates (OCHO, COOH and H)

$$\Delta\rho = \rho_{All} - \rho_{slab} - \rho_{adsorbate}$$

2.3.5.5 Investigation of interfacial synergy

To understand the interfacial synergy, DFT calculations were performed to investigate the energetics of key surface intermediates governing the kinetics of the ECO_2RR and the

competing HER. Motivated by the X-EDS mapping of the synthesized Bi-Cu_2S showing the dispersed Cu_2S moieties on the Bi domain (**Figure 2.6e**), we built an interface model using a rhombohedral Bi (001) surface decorated with hexagonal Cu_2S NRs. Cu_2S NRs were constructed with the sulfur-terminated (001) orientation on all sides (**Figure 2.20**), which allows a stable interface to be formed between the two low-index surfaces. Under relevant ECO_2RR conditions, Cu_2S is partially reduced according to previous reports.[49-51] The sulfur vacancy free formation energy of the stoichiometric Cu_2S (001) surface to generate H_2S(g) is -1.23 eV at potential -1.0 V *vs*. RHE (**Figure 2.21 and Figure 2.23b)** In **Figure 2.23b**, the sulfur vacancy free formation energy was plotted as a function of the operating potential U and pH. The red line is the potential U at which the vacancy starts forming. The vacancy free formation energy is negative below the red line indicating the feasibility of losing sulfur atoms on the surface. The reaction operating conditions were plotted as the black line, starting from -1.21 V to -1.61 V vs. SHE at pH=7, and at this condition, vacancies were formed on the surface. The generation of a second sulfur vacancy is energetically unfavorable, resulting in surface reconstruction. Thus, the interface model of Bi-Cu_2S contains one S vacancy in our model systems. This is consistent with our EDS spectra that the ratio of S/Cu decreases after the electrolysis. Since ECO_2RR on Bi surfaces mainly produces formate and CO with two-electron transfers, we consider the first proton-coupled electron transfer with the protonation of the C atom to form the *OCHO intermediate or O atom to form the *COOH intermediate.[52] The *OCHO and *COOH intermediates can be further reduced to $HCOO^-$ and CO, respectively (**Figure 2.23a**). The HER *via* the *H intermediate is also considered at the interfacial sites. The reaction pathway and the optimized geometries for each intermediate are shown in **Figure 2.23c-e**,

for both Bi and Bi-Cu_2S systems (**Figure 2.22**). The formation of the *COOH intermediate is significantly uphill in free energy than the *OCHO intermediate on both surfaces, leading to a favorable production of $HCOO^-$, consistent with the experimental results of a much higher FE_{HCOO-} than FE_{CO}. The Vomer step of the HER is highly unfavorable since the *H intermediate binds very weakly on Bi sites, resulting in a suppressed HER under CO_2 reduction conditions on Bi.[18, 53]

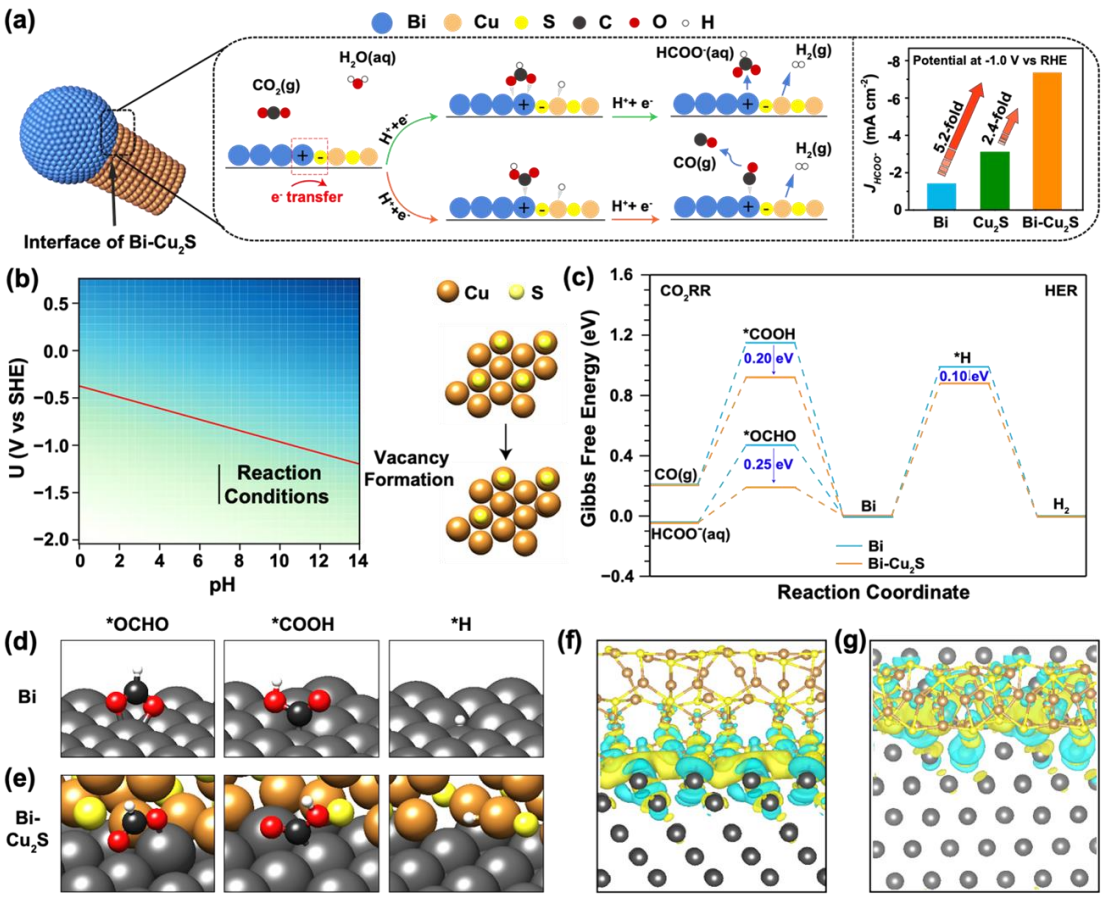

Figure 2.23. (a) Proposed CO_2 reduction mechanism on the Bi-Cu_2S interfacial system. (b) The sulfur vacancy formation pourbaix diagram. (c) Free energy diagrams of the ECO_2RR and HER on Bi (001) and Bi-Cu_2S model systems. Optimized geometry structures of key intermediates (*OCHO, *COOH, *H) on Bi (001) and Bi-Cu_2S systems are shown in (d) and (e), respectively. (Dark grey, brown, yellow, black, red, and white spheres denote Bi, Cu, S, C, O, and H atoms, respectively.) (f) and (g) are the top and front views of the charge density difference for Bi-Cu2S interfacial surface, respectively. Cyan corresponds to an isosurface of −0.001 e $Bohr^{-3}$ and yellow to +0.001 e $Bohr^{-3}$.

While the ECO_2RR is facilitated in both Bi and Bi-Cu_2S systems, the extent of stabilization of the CO- and $HCOO^-$-evolution intermediates varies. Attributed to the interactions between Bi and Cu_2S, *OCHO and *COOH are stabilized by 0.25 eV and 0.20 eV on the Bi-Cu_2S interfacial site, respectively, leading to a reduced overpotential and improved selectivity toward formate production compared with that on pure Bi. The *H intermediate is merely stabilized by 0.10 eV due to its adsorption on the Cu site of Bi-Cu_2S. Therefore, the HER is still inhibited in Bi-Cu_2S, consistent with our experiment results in **Figure 2.15e**. We further analyzed the local electronic structure of the interface and the adsorbates to gain insights into the improved performance. **Figure 2.24-2.25** shows the isosurfaces of the Cu_2S-induced charge density difference, and **Figure 2.26** shows the Bader charge analysis[54], both of which show that Bi is electron-deficit, which is consistent with the fact that a Schottky interface between Bi and Cu_2S could lead to the electron flow from Cu_2S to Bi[55-56]. For a bare Bi-Cu_2S surface (**Figure 2.23f-g**), the Bi substrate is electron-deficit, especially for Bi atoms forming bonds with S atoms, which plays an important role in electrostatically stabilizing the *OCHO and *COOH intermediates since both are negatively charged as shown in **Figure 2.25** of adsorbate-induced charge density difference on Bi (001).

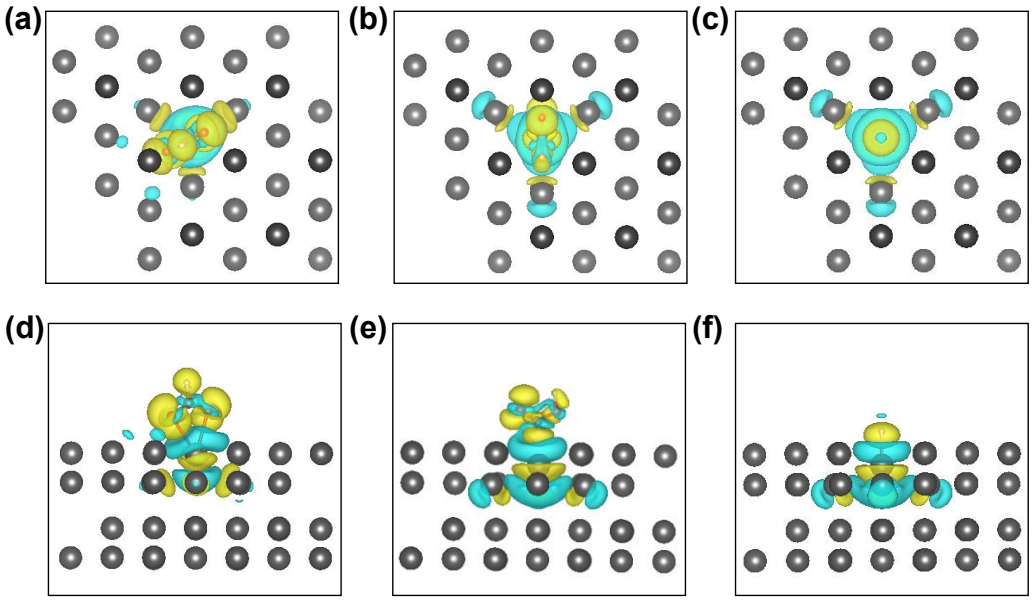

Figure 2.24. Isosurfaces of adsorbate-induced charge density difference for adsorbates on Bi (001). **(a), (b),** and **(c)** are top views of *OCHO, *COOH, and *H adsorbates, respectively. **(d), (e),** and **(f)** are front views of *OCHO, *COOH, and *H adsorbates, respectively. Cyan corresponds to an isosurface of −0.001 e $Bohr^{-3}$ and yellow to +0.001 e $Bohr^{-3}$.

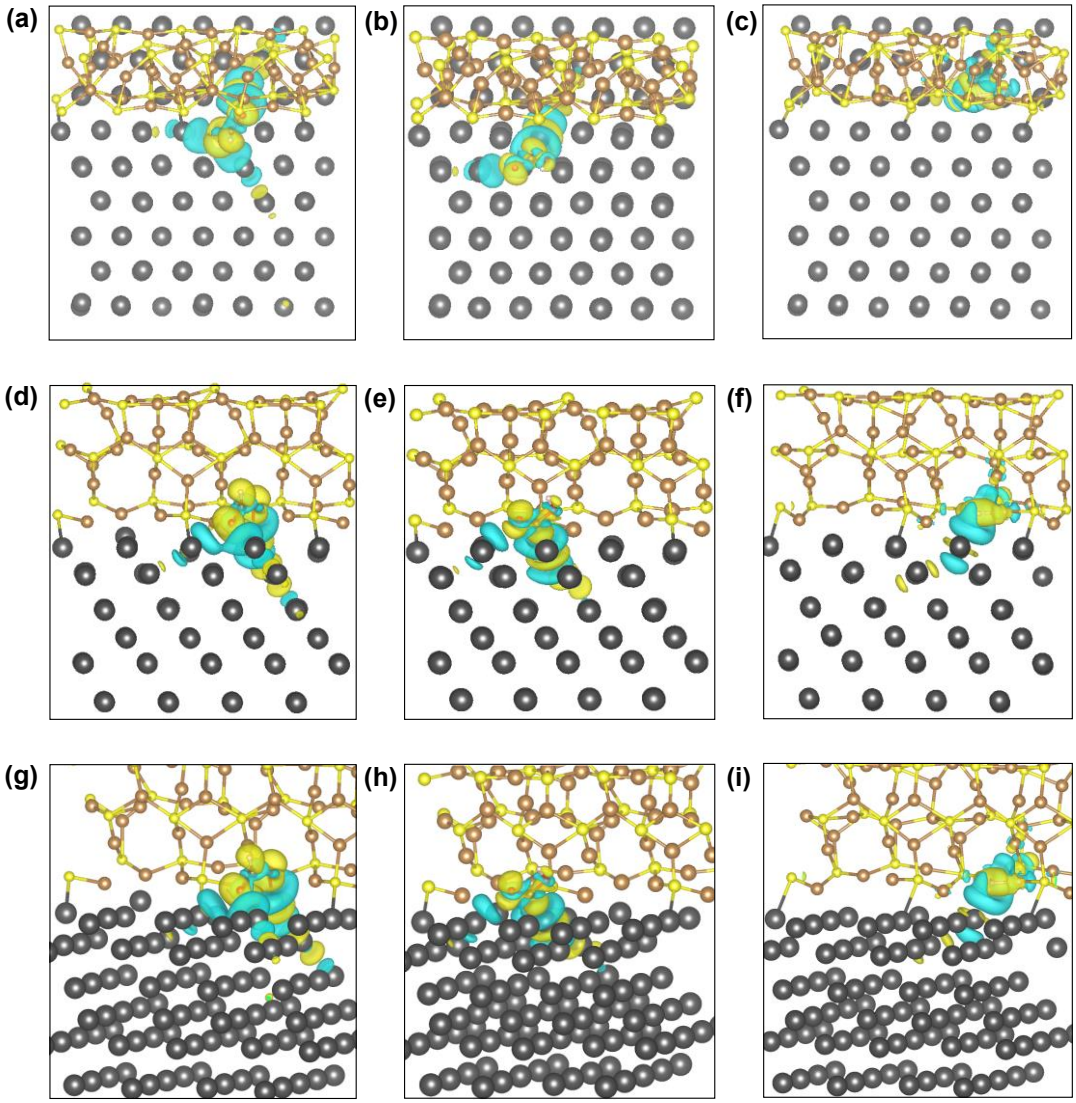

Figure 2.25. Isosurfaces of adsorbate-induced charge density difference for adsorbates on the Bi-Cu_2S interfacial surface. **(a), (b),** and **(c)** are top views of *OCHO, *COOH, and *H adsorbates, respectively. **(d)**, **(e)**, and **(f)** are front views of *OCHO, *COOH, and *H adsorbates, respectively. **(g), (h),** and **(i)** are side views of *OCHO, *COOH, and *H adsorbates, respectively. Cyan corresponds to an isosurface of −0.001 e $Bohr^{-3}$ and yellow to +0.001 e $Bohr^{-3}$.

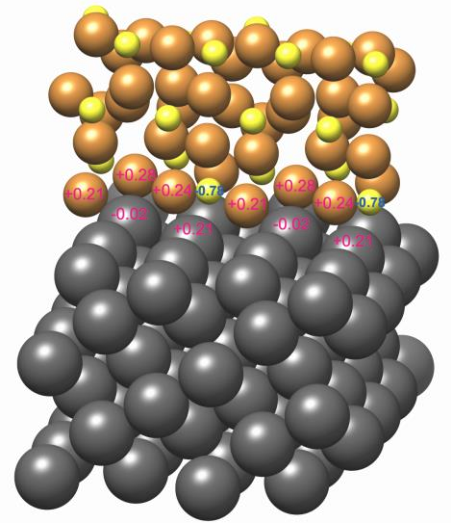

Figure 2.26. Bader charge analysis of the Bi-Cu_2S interfacial structure. Magenta values correspond to positive charges of atoms, and blue values correspond to negative charges of atoms.[57]

2.4 Conclusion

In summary, we have reported a one-pot synthesis of heterostructured Bi-Cu_2S nanocrystals for the ECO_2RR toward formate production. Detailed structural characterizations proved the successful construction of a well-connected, epitaxial interface between Bi and Cu_2S. Systematic electrochemical investigations demonstrated much enhanced ECO_2RR activity without the sacrifice of high selectivity at the interface between Bi and Cu_2S. Compared with Bi NPs, Cu_2S NRs, Bi+Cu_2S physical mixture, Bi-Cu_2S presented the highest FE at all applied potentials toward formate production, with partial current densities increased by 5.2-fold, 2.4-fold, 5.3-fold at -1.0 V vs. RHE, respectively. The onset potential of Bi-Cu_2S is ~240 mV more positive than that of Bi NPs.

These results provide clear evidence that the interfacial synergy in Bi-Cu_2S plays a pivotal role in promoting electrocatalysis. DFT calculations suggest that the electron transfer from Bi to Cu_2S at the interface stabilized the ECO_2RR intermediates, particularly for *OCHO toward $HCOO^-$ evolution compared with *COOH to CO and *H to H_2. This work highlights a unique design strategy of p-block metal and TMC heterostructures to fine tailor active sites for advanced electrocatalysis.

References

1. Zhao, J.; Xue, S.; Barber, J.; Zhou, Y. W.; Meng, J.; Ke, X. B., An overview of Cu-based heterogeneous electrocatalysts for CO_2 reduction. *J. Mater. Chem. A* **2020,** *8* (9), 4700-4734.

2. Wang, J.; Cheng, T.; Fenwick, A. Q.; Baroud, T. N.; Rosas-Hernández, A.; Ko, J. H.; Gan, Q.; Goddard Iii, W. A.; Grubbs, R. H., Selective CO_2 Electrochemical Reduction Enabled by a Tricomponent Copolymer Modifier on a Copper Surface. *J. Am. Chem. Soc.* **2021,** *143* (7), 2857-2865.

3. Liu, A. M.; Gao, M. F.; Ren, X. F.; Meng, F. N.; Yang, Y. N.; Gao, L. G.; Yang, Q. Y.; Ma, T. L., Current progress in electrocatalytic carbon dioxide reduction to fuels on heterogeneous catalysts. *J. Mater. Chem. A* **2020,** *8* (7), 3541-3562.

4. Li, M.; Wang, H.; Luo, W.; Sherrell, P. C.; Chen, J.; Yang, J., Heterogeneous Single-Atom Catalysts for Electrochemical CO_2 Reduction Reaction. *Adv. Mater.* **2020,** *32* (34), e2001848.

5. Garg, S.; Li, M. R.; Weber, A. Z.; Ge, L.; Li, L. Y.; Rudolph, V.; Wang, G. X.; Rufford, T. E., Advances and challenges in electrochemical CO_2 reduction processes: an engineering and design perspective looking beyond new catalyst materials. *J. Mater. Chem. A* **2020,** *8* (4), 1511-1544.

6. Fan, L.; Xia, C.; Yang, F. Q.; Wang, J.; Wang, H. T.; Lu, Y. Y., Strategies in catalysts and electrolyzer design for electrochemical CO_2 reduction toward C_{2+} products. *Sci. Adv.* **2020,** *6* (8).

7. Zhang, W. J.; Hu, Y.; Ma, L. B.; Zhu, G. Y.; Wang, Y. R.; Xue, X. L.; Chen, R. P.; Yang, S. Y.; Jin, Z., Progress and Perspective of Electrocatalytic CO_2 Reduction for Renewable Carbonaceous Fuels and Chemicals. *Adv. Sci.* **2018,** *5* (1).

8. Quan, Y.; Zhu, J.; Zheng, G., Electrocatalytic Reactions for Converting CO_2 to Value-Added Products. *Small Sci.*, 2100043.

9. Han, X.; Gao, Q.; Yan, Z. H.; Ji, M. X.; Long, C.; Zhu, H. Y., Electrocatalysis in confined spaces: interplay between well-defined materials and the microenvironment. *Nanoscale* **2021,** *13* (3), 1515-1528.

10. Wang, Q.; Cai, C.; Dai, M.; Fu, J.; Zhang, X.; Li, H.; Zhang, H.; Chen, K.; Lin, Y.; Li, H.; Hu, J.; Miyauchi, M.; Liu, M., Recent Advances in Strategies for Improving the Performance of CO_2 Reduction Reaction on Single Atom Catalysts. *Small Sci.* **2021,** *1* (2), 2000028.

11. Wu, Z.; Wu, H.; Cai, W.; Wen, Z.; Jia, B.; Wang, L.; Jin, W.; Ma, T., Engineering Bismuth–Tin Interface in Bimetallic Aerogel with a 3D Porous Structure for Highly Selective Electrocatalytic CO_2 Reduction to HCOOH. *Angew. Chem. Int. Ed.* **2021,** *60* (22), 12554-12559.

12. Zhang, Z. Y.; Chi, M. F.; Veith, G. M.; Zhang, P. F.; Lutterman, D. A.; Rosenthal, J.; Overbury, S. H.; Dai, S.; Zhu, H. Y., Rational Design of Bi Nanoparticles for Efficient Electrochemical CO_2 Reduction: The Elucidation of Size and Surface Condition Effects. *ACS Catal.* **2016,** *6* (9), 6255-6264.

13. Franco, F.; Rettenmaier, C.; Jeon, H. S.; Roldan Cuenya, B., Transition metal-based catalysts for the electrochemical CO_2 reduction: from atoms and molecules to nanostructured materials. *Chem. Soc. Rev.* **2020,** *49* (19), 6884-6946.

14. Yu, J. L.; Wang, J.; Ma, Y. B.; Zhou, J. W.; Wang, Y. H.; Lu, P. Y.; Yin, J. W.; Ye, R. Q.; Zhu, Z. L.; Fan, Z. X., Recent Progresses in Electrochemical Carbon Dioxide Reduction on Copper-Based Catalysts toward Multicarbon Products. *Adv. Funct. Mater.* **2021**.

15. Gong, Q. F.; Ding, P.; Xu, M. Q.; Zhu, X. R.; Wang, M. Y.; Deng, J.; Ma, Q.; Han, N.; Zhu, Y.; Lu, J.; Feng, Z. X.; Li, Y. F.; Zhou, W.; Li, Y. G., Structural defects on converted bismuth oxide nanotubes enable highly active electrocatalysis of carbon dioxide reduction. *Nat. Commun.* **2019,** *10*.

16. Gao, Q.; Mou, T.; Liu, S.; Johnson, G.; Han, X.; Yan, Z.; Ji, M.; He, Q.; Zhang, S.; Xin, H.; Zhu, H., Monodisperse PdSn/SnO_x core/shell nanoparticles with superior electrocatalytic ethanol oxidation performance. *J. Mater. Chem. A* **2020,** *8* (40), 20931-20938.

17. Zhang, E. H.; Wang, T.; Yu, K.; Liu, J.; Chen, W. X.; Li, A.; Rong, H. P.; Lin, R.; Ji, S. F.; Zhene, X. S.; Wang, Y.; Zheng, L. R.; Chen, C.; Wang, D. S.; Zhang, J. T.; Li, Y. D., Bismuth Single Atoms Resulting from Transformation of Metal-Organic Frameworks and Their Use as Electrocatalysts for CO_2 Reduction. *J. Am. Chem. Soc.* **2019,** *141* (42), 16569-16573.

18. Yang, F.; Elnabawy, A. O.; Schimmenti, R.; Song, P.; Wang, J. W.; Peng, Z. Q.; Yao, S.; Deng, R. P.; Song, S. Y.; Lin, Y.; Mavrikakis, M.; Xu, W. L., Bismuthene for highly efficient carbon dioxide electroreduction reaction (vol 11, 1088, 2020). *Nat. Commun.* **2020,** *11* (1).

19. Guan, Y. Y.; Liu, M. M.; Rao, X. F.; Liu, Y. Y.; Zhang, J. J., Electrochemical reduction of carbon dioxide (CO_2): bismuth-based electrocatalysts. *J. Mater. Chem. A* **2021,** *9* (24), 13770-13803.

20. Li, Z.; Feng, Y.; Li, Y.; Chen, X.; Li, N.; He, W.; Liu, J., Fabrication of Bi/Sn bimetallic electrode for high-performance electrochemical reduction of carbon dioxide to formate. *Chem. Eng. J.* **2022,** *428*, 130901.

21. Wen, G. B.; Lee, D. U.; Ren, B. H.; Hassan, F. M.; Jiang, G. P.; Cano, Z. P.; Gostick, J.; Croiset, E.; Bai, Z. Y.; Yang, L.; Chen, Z. W., Orbital Interactions in Bi-Sn Bimetallic Electrocatalysts for Highly Selective Electrochemical CO_2 Reduction toward Formate Production. *Adv. Energy Mater.* **2018,** *8* (31).

22. Xing, Y.; Kong, X.; Guo, X.; Liu, Y.; Li, Q.; Zhang, Y.; Sheng, Y.; Yang, X.; Geng, Z.; Zeng, J., Bi@Sn Core–Shell Structure with Compressive Strain Boosts the Electroreduction of CO_2 into Formic Acid. *Adv. Sci.* **2020,** *7* (22), 1902989.

23. Lv, W. X.; Zhou, J.; Bei, J. J.; Zhang, R.; Wang, L.; Xu, Q.; Wang, W., Electrodeposition of nano-sized bismuth on copper foil as electrocatalyst for reduction of CO_2 to formate. *Appl. Surf. Sci.* **2017,** *393*, 191-196.

24. Wang, Z. J.; Yuan, Q.; Shan, J. J.; Jiang, Z. H.; Xu, P.; Hu, Y. F.; Zhou, J. G.; Wu, L. N.; Niu, Z. Z.; Sun, J. M.; Cheng, T.; Goddard, W. A., Highly Selective Electrocatalytic

Reduction of CO_2 into Methane on Cu-Bi Nanoalloys. *J. Phys. Chem. Lett.* **2020,** *11* (17), 7261-7266.

25. Yang, Z.; Wang, H.; Fei, X.; Wang, W.; Zhao, Y.; Wang, X.; Tan, X.; Zhao, Q.; Wang, H.; Zhu, J.; Zhou, L.; Ning, H.; Wu, M., MOF derived bimetallic CuBi catalysts with ultra-wide potential window for high-efficient electrochemical reduction of CO_2 to formate. *Appl. Catal. B* **2021,** *298*, 120571.

26. Sun, X. F.; Zhu, Q. G.; Kang, X. C.; Liu, H. Z.; Qian, Q. L.; Zhang, Z. F.; Han, B. X., Molybdenum-Bismuth Bimetallic Chalcogenide Nanosheets for Highly Efficient Electrocatalytic Reduction of Carbon Dioxide to Methanol. *Angew. Chem. Int. Ed.* **2016,** *55* (23), 6771-6775.

27. Montemore, M. M.; Medlin, J. W., Scaling relations between adsorption energies for computational screening and design of catalysts. *Catalysis Science & Technology* **2014,** *4* (11), 3748-3761.

28. Li, Y. W.; Sun, Q., Recent Advances in Breaking Scaling Relations for Effective Electrochemical Conversion of CO_2. *Adv. Energy Mater.* **2016,** *6* (17).

29. Yan, Z.; Ji, M.; Xia, J.; Zhu, H., Recent Advanced Materials for Electrochemical and Photoelectrochemical Synthesis of Ammonia from Dinitrogen: One Step Closer to a Sustainable Energy Future. *Adv. Energy Mater.* **2019,** *10* (11).

30. Chen, Y.; Chen, K.; Fu, J.; Yamaguchi, A.; Li, H.; Pan, H.; Hu, J.; Miyauchi, M.; Liu, M., Recent advances in the utilization of copper sulfide compounds for electrochemical CO_2 reduction. *Nano Mater. Sci.* **2020,** *2* (3), 235-247.

31. Deng, Y. L.; Huang, Y.; Ren, D.; Handoko, A. D.; Seh, Z. W.; Hirunsit, P.; Yeo, B. S., On the Role of Sulfur for the Selective Electrochemical Reduction of CO_2 to Formate on CuS_x Catalysts. *ACS Appl. Mater. Interfaces* **2018,** *10* (34), 28572-28581.

32. Liu, S. B.; Lu, X. F.; Xiao, J.; Wang, X.; Lou, X. W., Bi_2O_3 Nanosheets Grown on Multi-Channel Carbon Matrix to Catalyze Efficient CO_2 Electroreduction to HCOOH. *Angew. Chem. Int. Ed.* **2019,** *58* (39), 13828-13833.

33. Deng, P. L.; Wang, H. M.; Qi, R. J.; Zhu, J. X.; Chen, S. H.; Yang, F.; Zhou, L.; Qi, K.; Liu, H. F.; Xia, B. Y., Bismuth Oxides with Enhanced Bismuth-Oxygen Structure for Efficient Electrochemical Reduction of Carbon Dioxide to Formate. *ACS Catal.* **2020,** *10* (1), 743-750.

34. Zhang, Y.; Li, F. W.; Zhang, X. L.; Williams, T.; Easton, C. D.; Bond, A. M.; Zhang, J., Electrochemical reduction of CO_2 on defect-rich Bi derived from Bi_2S_3 with enhanced formate selectivity. *J. Mater. Chem. A* **2018,** *6* (11), 4714-4720.

35. Zhang, Z.; Chi, M.; Veith, G. M.; Zhang, P.; Lutterman, D. A.; Rosenthal, J.; Overbury, S. H.; Dai, S.; Zhu, H., Rational Design of Bi Nanoparticles for Efficient Electrochemical CO_2 Reduction: The Elucidation of Size and Surface Condition Effects. *ACS Catal.* **2016,** *6* (9), 6255-6264.

36. Zhai, Y.; Shim, M., Cu_2S/ZnS Heterostructured Nanorods: Cation Exchange vs. Solution-Liquid-Solid-like Growth. *Chemphyschem* **2016,** *17* (5), 741-751.

37. Tan, W.; Cao, B.; Xiao, W.; Zhang, M.; Wang, S.; Xie, S.; Xie, D.; Cheng, F.; Guo, Q.; Liu, P., Electrochemical Reduction of CO_2 on Hollow Cubic Cu2O@Au Nanocomposites. *Nanoscale Research Letters* **2019,** *14* (1), 63.

38. Mun, Y.; Lee, S.; Cho, A.; Kim, S.; Han, J. W.; Lee, J., Cu-Pd alloy nanoparticles as highly selective catalysts for efficient electrochemical reduction of CO_2 to CO. *Appl. Catal. B* **2019,** *246*, 82-88.

39. Davey, W. P., Precision Measurements of the Lattice Constants of Twelve Common Metals. *Physical Review* **1925,** *25* (6), 753-761.

40. Buerger, M. J. a. W., B J, Distribution of Atoms in High Chalcocite, Cu_2S. *Science* **1963,** *141* (3577), 276--277.

41. Peterson, A. A.; Abild-Pedersen, F.; Studt, F.; Rossmeisl, J.; Nørskov, J. K., How copper catalyzes the electroreduction of carbon dioxide into hydrocarbon fuels. *Energy Environ. Sci.* **2010,** *3* (9), 1311-1315.

42. Han, N.; Wang, Y.; Yang, H.; Deng, J.; Wu, J.; Li, Y.; Li, Y., Ultrathin bismuth nanosheets from in situ topotactic transformation for selective electrocatalytic CO_2 reduction to formate. *Nat. Commun.* **2018,** *9* (1), 1320.

43. Rendón-Calle, A.; Builes, S.; Calle-Vallejo, F., Substantial improvement of electrocatalytic predictions by systematic assessment of solvent effects on adsorption energies. *Appl. Catal. B* **2020,** *276*, 119147.

44. Bohra, D.; Ledezma-Yanez, I.; Li, G.; de Jong, W.; Pidko, E. A.; Smith, W. A., Lateral Adsorbate Interactions Inhibit HCOO− while Promoting CO Selectivity for CO_2 Electrocatalysis on Silver. *Angew. Chem. Int. Ed.* **2019,** *58* (5), 1345-1349.

45. Nørskov, J. K.; Rossmeisl, J.; Logadottir, A.; Lindqvist, L.; Kitchin, J. R.; Bligaard, T.; Jónsson, H., Origin of the Overpotential for Oxygen Reduction at a Fuel-Cell Cathode. *The Journal of Physical Chemistry B* **2004,** *108* (46), 17886-17892.

46. Rossmeisl, J.; Chan, K.; Ahmed, R.; Tripković, V.; Björketun, M. E., pH in atomic scale simulations of electrochemical interfaces. *Physical Chemistry Chemical Physics* **2013,** *15* (25), 10321-10325.

47. Halldin Stenlid, J.; dos Santos, E.; Johansson, A.; Pettersson, L., On the Nature of the Cathodic Reaction during Corrosion of Copper in Anoxic Sulfide Solutions. *Journal of The Electrochemical Society* **2019,** *166*, C196-C208.

48. Kashida, S.; Shimosaka, W.; Mori, M.; Yoshimura, D., Valence band photoemission study of the copper chalcogenide compounds, Cu_2S, Cu_2Se and Cu_2Te. *Journal of Physics and Chemistry of Solids* **2003,** *64* (12), 2357-2363.

49. Thao, N. T. P.; Tsuji, S.; Jeon, S.; Park, I.; Tabelin, C. B.; Ito, M.; Hiroyoshi, N., Redox potential-dependent chalcopyrite leaching in acidic ferric chloride solutions: Leaching experiments. *Hydrometallurgy* **2020,** *194*.

50. Zhang, Y.; Yao, D.; Xia, B.; Xu, H.; Tang, Y.; Davey, K.; Ran, J.; Qiao, S.-Z., ReS_2 Nanosheets with In Situ Formed Sulfur Vacancies for Efficient and Highly Selective Photocatalytic CO_2 Reduction. *Small Sci.* **2021,** *1* (2), 2000052.

51. Persson, K. A.; Waldwick, B.; Lazic, P.; Ceder, G., Prediction of solid-aqueous equilibria: Scheme to combine first-principles calculations of solids with experimental aqueous states. *Phys. Rev. B* **2012,** *85* (23).

52. Pillai, H. S.; Xin, H. L., New Insights into Electrochemical Ammonia Oxidation on Pt(100) from First Principles. *Industrial & Engineering Chemistry Research* **2019,** *58* (25), 10819-10828.

53. Han, N.; Wang, Y.; Yang, H.; Deng, J.; Wu, J. H.; Li, Y. F.; Li, Y. G., Ultrathin bismuth nanosheets from in situ topotactic transformation for selective electrocatalytic CO_2 reduction to formate. *Nat. Commun.* **2018,** *9*.

54. Tang, W.; Sanville, E.; Henkelman, G., A grid-based Bader analysis algorithm without lattice bias. *J. Phys.: Condens. Matter* **2009,** *21* (8), 084204.

55. Zhang, Y.; Qiu, Y.; Ma, Z.; Wang, Y.; Zhang, Y.; Ying, Y.; Jiang, Y.; Zhu, Y.; Liu, S., Core-corona Co/CoP clusters strung on carbon nanotubes as a Schottky catalyst for glucose oxidation assisted H2 production. *J. Mater. Chem. A* **2021,** *9* (17), 10893-10908.

56. Ji, X.; Zhang, Y.; Ma, Z.; Qiu, Y., Oxygen Vacancy-rich Ni/NiO@NC Nanosheets with Schottky Heterointerface for Efficient Urea Oxidation Reaction. *ChemSusChem* **2020,** *13* (18), 5004-5014.

57. Tang, W.; Sanville, E.; Henkelman, G., A grid-based Bader analysis algorithm without lattice bias. *J Phys Condens Matter* **2009,** *21* (8), 084204.

CHAPTER 3

Electrocatalysis in confined spaces: interplay between well-defined materials and the microenvironment

3.1 Introduction

Tailoring active sites to stabilize or destabilize reaction intermediates plays a pivotal role in catalysis and thus has been commonly exploited as a powerful strategy to steer catalytic pathways for desired outcomes.[1-2] Nevertheless, energy scaling relations place constraints on optimizing catalytic performances. Consequently, there usually exists a volcano-shaped activity or selectivity trend on various catalyst surfaces.[3-5] For example, in the electrochemical oxygen reduction reaction (ORR), Pt alloys with different compositions demonstrate a 'volcano' relationship between the measured activities and the adsorption energies of key intermediates, e.g., the oxygen-binding energy, along the reaction path.[3, 6-7] Similarly, in the electrochemical CO_2 reduction reaction (CO_2RR), the activity is limited by scaling relations between the binding energy of *CO and its hydrogenated species such as *CHO and *COH.[8-9] The holistic kinetic and transport control to boost catalytic performance has been widely used in the industry. However, this exhaustive sorting of optimum operating conditions remains challenging. Inspired by nature where enzymes can create a protein environment and incorporate multifunctionality to modulate catalytic reactions, the microenvironment, i.e., the confined space in close proximity to the catalytic active site, is now being recognized as equally important as the active site in regulating catalytic results and thus has been attracting extensive attention in recent years.[10]

The confinement effect, especially at nanoscale, denoted as nanoconfinement, has been investigated thoroughly in conventional heterogeneous catalysis. For example, carbon nanotubes (CNTs) are a common class of materials that can establish nanoconfinement effects on active sites.[11-13] Nanoconfinement has also been observed in nanocatalysts under two-dimensional (2D) materials, e.g., graphene and hexagonal boron nitride (*h*-BN), denoted as "catalysis under cover".[14-15] Recently, confined catalysis in emerging porous materials, such as metal-organic frameworks (MOFs), covalent organic frameworks (COFs), and polymer layers has been considered as an effective strategy in modulating the diffusion and transport of reactants to promote catalysis.[10, 16-17] The comprehensive discussion of confinement effects in conventional thermal catalysis can be found elsewhere[15-16, 18], and is beyond the scope of this article.

Electrocatalysis enables the conversion of small molecules, such as CO_2, N_2, and H_2O into high-value chemicals or fuels, paving the road to a sustainable energy future with minimal carbon footprint.[1, 19-21] The rational design of electrocatalysts is therefore of crucial importance in achieving this sustainable future. Compared with the abundant literature of confinement effects in thermal catalysis, electrocatalysis in confined spaces is relatively less discussed. Similar to the case of heterogeneous catalysis, a confinement environment in electrocatalysis embraces mechanical, electronic, and geometric effects[22-23] (**Figure.3.1**), stabilizing important charge-transfer intermediates and promoting reaction kinetics. It may also enable a desired diffusion and transport rate of reactants through the formation of porous nanoreactors.[12, 15] Specifically, mechanical effects induced by the geometric constraint can come into play. For example, a fine-tailored nano-space between CNTs and embedded metals could weaken the interaction between the confined reactants

and metal sites due to the mechanical forces.[22] Electronic effects can also affect the reactivity of electrocatalysis in the confined environment, similar to the case of confined catalysis where electron interactions, charge-transfer, and shifting of d-band of metal centers can occur.[22] Furthermore, geometric effects resulting from the coverage of active sites by CNTs also play a crucial role in affecting the catalytic behavior in confined catalysis. For example, the experimental investigations and atomistic simulations of single- and multi-wall CNTs demonstrated that the number of walls and radius of CNTs could determine their stability, thus potentially affecting their durability and activity during electrochemical reactions.[24]

Here, we summarize the most recent progress in electrocatalysis, especially CO_2RR, in confined spaces with a focus on nanomaterials encapsulated by carbon-based materials. More specifically, we provide a comprehensive perspective of metal-encapsulated CNTs (M@CNTs) employed in electrocatalysis. Various types of M@CNTs mainly focusing on non-precious metal-based materials are presented and discussed. Furthermore, applications of M@CNTs in CO_2RR is summarized and discussed in detail.

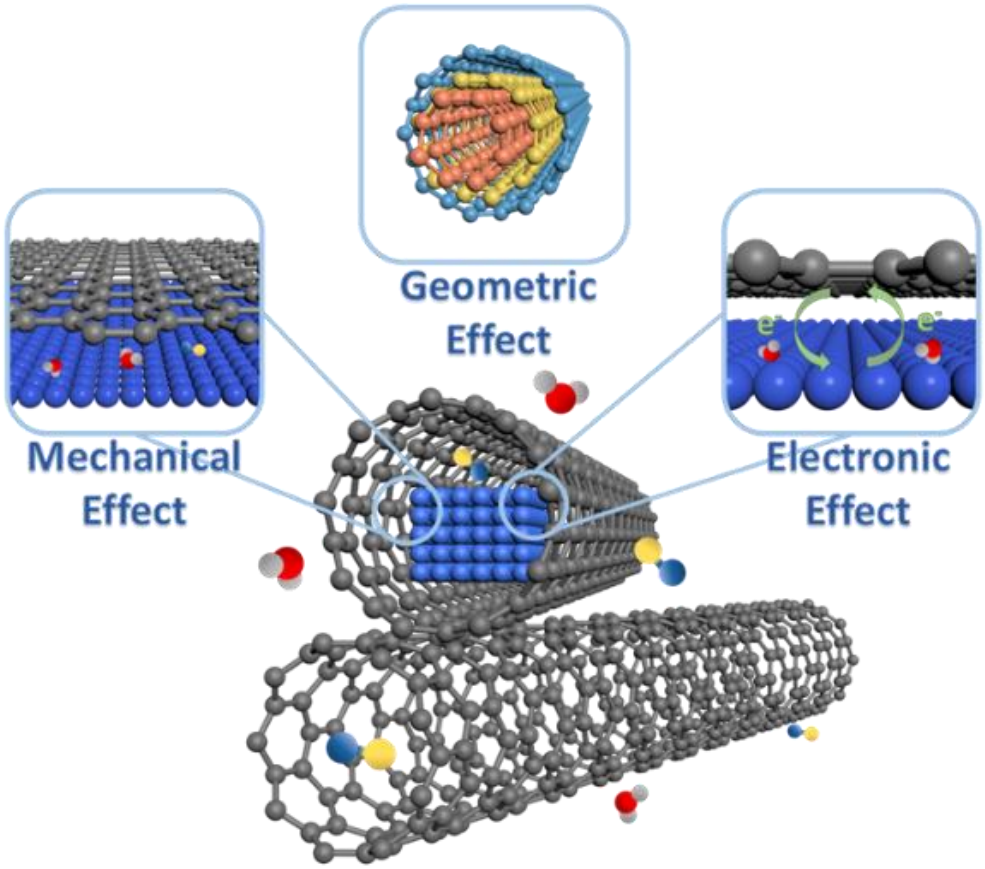

Figure 3.1. Schematic illustration of three important confinement effects using materials confined in CNTs as an example.

3.2 Fundamentals of CNTs in confined catalysis

3.2.1 Background of CNTs and their applications in electrocatalysis

Since the discovery of CNTs by Iijima in 1991, this unique one-dimensional (1D) material with a finite carbon structure and a needle-like tube morphology has attracted increasing research attention in the catalysis community.[25] CNTs can be categorized into two groups. One is the single-walled nanotube (SWNT), which is a single graphite sheet rolled into a cylindrical morphology. The other is multi-walled nanotubes (MWNTs) consisting of multiple rolled graphene layers with a mutual center. CNTs are wrapped into cylinder tubes by graphene layers through sp^2 bonds that hold the carbon atoms into an aromatic ring structure.[26] Such a well-defined structure with the strong π-electron interaction results in outstanding electrical capacitance and intriguing quantum effects of CNTs.[27] Recent research demonstrates that using CNTs as the carbon support in electrocatalysis provides synergistic interactions with metal catalysts and thus improves catalytic activity and selectivity.[28-29] To date, many M@CNTs have been engineered into high-efficiency electrocatalysts in a range of electrocatalytic reactions such as ORR, water-splitting reactions, CO_2RR, and NRR.

3.2.2 Fundamental of confined catalysis

Understanding the fundamentals of the confinement effect has become an essential topic in catalysis fields. The confined environment is usually established at the space between metal surfaces and 2D materials, 1D nanotubes, and zero-dimensional (0D) porous materials, providing an ideal platform to incorporate site and environment cooperativity for enhancing catalytic performance. For example, compared with the metal nanoparticles (NPs) deposited on the exterior wall of CNTs, confined space of metal NPs encapsulated

in CNTs exhibit tailored catalytic activities due to the electronic effects.[11] Further experimental studies showed that the interplay between spatial confinement and electronic structure leads to significant strains and deformations in CNT channels, resulting in the downshift of d-band states and thus weakening the adsorption of molecules such as O_2 and CO.[2, 11, 22] Theoretical efforts in identifying the origin of the quantum confinement effect reveal that the spatially confined environment increases the molecular orbital energy, thus changing the adsorption and activation of confined reactants.[14] To unify the descriptor of the confinement effect and enable the prediction of its role on catalytic activities, the confinement energy (E_{con}) is defined as the adsorption energy difference with and without confinement environment. Specifically, by analyzing the electronic structure, it was found that the strong interaction between the encapsulated metal sites and the interior surface of CNT leads to the downshift of metal d-band states.[11] Such a shift weakens the binding energy of oxygen (E_b(O)). Consequently, the confined metals are more difficult to be oxidized than those on the exterior walls of CNTs. As E_b(O) differs from the interior walls to exterior walls on CNTs, this difference has been defined as the Econ, showing as,

$$E_{con} = E_b(\text{in}) - E_b(\text{out}) \qquad \text{(Eqn. 1)}$$

where E_b(in) and E_b(out) are the binding energies of adsorbates over the confined metal and the same metal deposited on the CNT exterior walls, respectively.[11] A positive E_{con} suggests weakened adsorption of reactants/intermediates, which can be confirmed by surface science experiments.[11, 14] Previous investigations demonstrate that E_{con} can effectively explain the confinement effect inside CNTs where the adsorption energy of intermediates/molecules is reduced compared with that of those metals on the exterior

walls.[11] This concept has a significant impact on tuning the molecule-metal interaction in a confined system and the corresponding confinement effect can be clearly explained by E_{con}.[22]

3.3 Electrocatalysis in confined spaces

The carbon-based materials provide a confined space around the active sites, ultimately affecting the catalytic behavior in various electrocatalytic reactions. In the following session, we highlight the most recent advances in space-confined electrocatalysis with emphasis on the microenvironment created by CNTs. Confinements imposed by other carbon-based materials such as well-defined 2D graphene and oxides are also discussed as an extension of the scope. We present the synthesis, characterization, electrochemical evaluation, and mechanistic investigation of the aforementioned systems and emphasize the importance of understanding the interplay between well-defined materials and the microenvironment in the rational design of efficient electrocatalysts. Moreover, electrocatalysis in confined spaces is discussed in detail of CO_2RR.

3.3.1 CO_2RR in confined spaces

Mastery of the conversion of the excess CO_2 to high value-added carbon-based chemicals is paramount to address the energy crisis. CO_2RR driven by renewable electricity and using water as the proton source provides a possible route to enable a carbon-neutral cycle.[30-32] Currently, noble metals including Au, Pd, and Ag predominately convert CO_2 into CO under electric bias; while the base metals such as Bi, Sn and In, generate formic acid as the major product.[33-38] N-CNTs also demonstrate activity for CO_2RR with a much

lower cost compared with the aforementioned metal systems.[39] Wu et al. found different types of nitrogen in N-CNTs exhibited different selectivity towards CO. The pyridinic nitrogen possessed the higher adsorption energy in the rate-determining step of the first electron-proton transfer to form the intermediate *COOH, thus weakening the binding of *CO.[40] In general, the confinement effect in CNTs can help to reduce the adsorption energy of the intermediates at the active sites, facilitating the dissociation of target products and promoting the reaction kinetics.[11] As a result, recent work has been focused on the non-precious metal NPs encapsulated in N-CNTs to exploit the confinement effect on the adsorption energy to steer the pathway of CO_2RR.

Ni NPs encapsulated in N-CNTs (Ni@N-CNTs) have been synthesized using a one-step pyrolysis method by annealing the mixed dicyandiamide and $NiCl_2$ under the protection of N_2.[41] TEM shows that Ni NPs with a diameter of 50-100 nm were wrapped by layers of N-CNTs (**Figure. 3.2a**). The X-ray absorption fine structure analysis confirmed the metallic state of Ni in Ni@N-CNTs. To shed light on the confinement effect in CO_2RR by confining Ni NPs inside the N-CNTs, Ni NPs deposited on the exterior surface of N-CNTs (Ni-N-CNTs) were prepared as a comparison. Ni@N-CNTs demonstrated the highest Faradic efficiency (FE) of 99.1% towards CO at −0.8 V (vs. RHE), while the maximum FE of Ni-N- CNTs, N-CNTs, and Ni NPs only could reach up to 34.9%, 35.9%, and 0.3%, respectively. The largely enhanced selectivity towards CO in Ni@N-CNTs was attributed to the benefit of confined metallic Ni, which significantly decreased the charge-transfer resistance and boosted the formation of intermediates *CO. Moreover, the FE for CO production was maintained at 96% after a 20 h long-term test. In addition, the calculation results on the different sites inside or outside CNTs and N-CNTs of Ni clusters (**Figure.**

3.2b, c) further verified the Ni clusters confined in CNTs indeed weakened the adsorption *CO on Ni surface, facilitating the dissociation of CO molecules. It is noteworthy that Ni was the active site for CO_2RR in Ni@N-CNTs and the content of Ni was determined up to 26 wt%. Decreasing the size of metal NPs to the single-atom level emerges as an efficient strategy to maximize the atom efficiency. Hou et al. reported a self-sacrifice template method by pyrolysis of core-shell ZnO@ZIF-NiZn nanorods at 800 °C for 5 h to obtain Ni single atoms anchored N-CNTs (Ni SAs@N-CNTs) catalyst, enabling highly exposed active centers to adsorb and activate CO_2 molecules.[42] Nearly 100% FE of CO was obtained at −0.8 V vs. RHE in Ni SAs@N-CNTs system with Ni content confirmed to be 1.68 wt%.

In addition to embedding metal particles in N-CNTs, the construction of M-N-C structure via anchoring metal-based hybrid materials inside the CNTs is effective in advancing the electrocatalytic activity.[43] For example, Jia et al. prepared the Fe/Fe_3C NPs wrapped by N-CNTs, denoted as Fe/Fe_3C@N-CNTs via annealing the mixed dicyandiamide and carbon-coated Fe_3O_4 NPs at 650, 750 and 850 °C, respectively.[44] TEM and HRTEM images in **Figure. 3.2d, 3.2e** show the successful encapsulation of Fe/Fe_3C NPs inside the CNTs. Compared to the samples calcined at 650 and 850 °C, Fe/Fe_3C@N-CNTs calcined at 750 °C showed the lowest onset potential and maximum FE of CO at -0.74 V vs. RHE. Meanwhile, the syngas of H_2/CO ratio could be flexibly regulated in the range from 1:1 to 3:1 (**Figure. 3.2f**). The high selectivity for CO production in Fe/Fe_3C@N-CNTs-750 could be attributed to the abundant pyridinic and pyrrolic nitrogen that facilitates the dissociation of *CO. To sum up, intimate contact between CO_2 molecules and metal NPs can be established thanks to the space confinement in N-CNTs. Moreover, the binding and protonation of intermediates can be tuned by controlling the d-

band states of metal centers. Nevertheless, there are only a few examples of CO_2RR in this research area. We envision that the rational design and synthesis of metallic NPs confined in N-CNTs merits further investigations on generating high value-added products, especially C_{2+} products in CO_2RR.

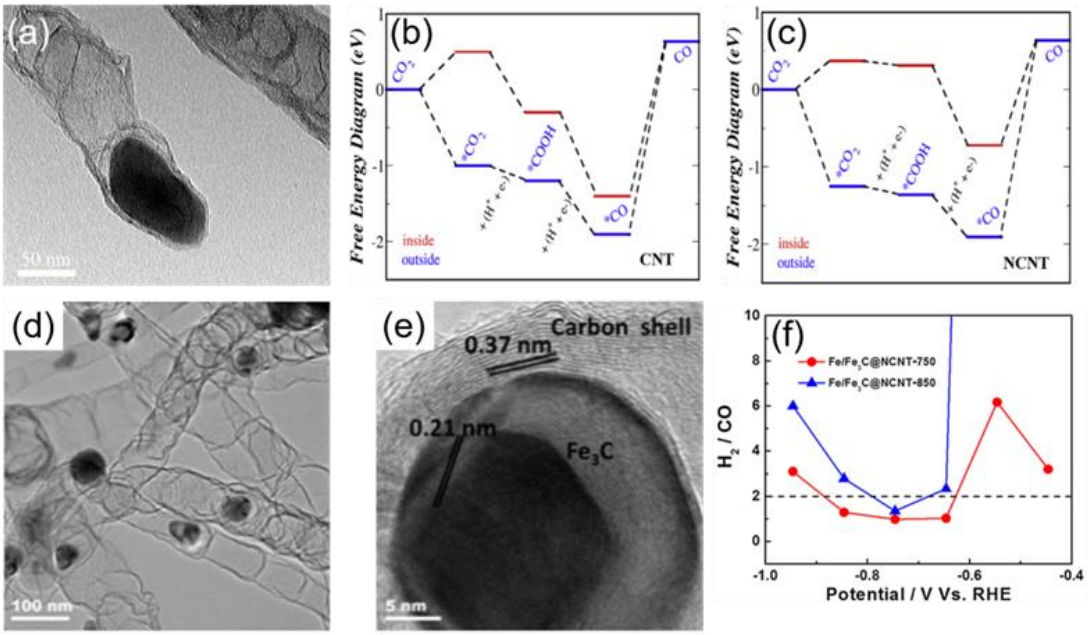

Figure 3.2. (a) TEM image of Ni@N-CNTs; free energy diagram (at 0 V) of CO_2 electroreduction over the confined Ni catalysts (b) inside or outside CNTs and (c) inside or outside N-CNTs. (This figure has been adapted/reproduced from ref 86 with permission from Elsevier, copyright 2019) (d) TEM and (e) HRTEM images of Fe/Fe_3C@N-CNTs-750 sample; (f) The ratio of the FE of H_2 and CO of Fe/Fe_3C@N-CNTs samples at different potentials.

3.4 Conclusion

A critical element in the pursuit of design strategies for advanced electrocatalysts is the simultaneous control of active sites and their surrounding microenvironment. Electrocatalysis in confined spaces is well-suited for this mission and opens enormous opportunities for future catalyst design. One of the crucial concepts here is confinement energy that describes the difference of binding energy with/without the confined space. With this concept, it enables the prediction of confinement effects on electrocatalytic behavior in different reaction systems. The interplay between active sites and their microenvironment provides synergetic electronic, mechanical, and/or geometric effects in directing electrocatalytic outcomes of confined systems. For example, in the nitrogen-doped CNTs system, the interaction between the N dopants and embedded metal catalysts can generate more efficient active centers to further improve their catalytic activity. As discussed in 4.3, the interplay between active centers and CNTs usually leads to the protective environment against electrochemical cycling, shifting of metal centers, charge-transfer, as well as adjusted work functions of CNTs to regulate the adsorption and activation of reactants and intermediates. Furthermore, non-precious metal NPs confined in carbon-based materials demonstrate comparable performance CO_2RR with those precious metal-based state-of-the-art catalysts.

3.5 Challenges and opportunities

Compared with the fundamental investigation of conventional heterogeneous catalysis, the origin of the confinement effect in electrocatalysis has not been fully revealed. Surface science, especially by coupling of electrochemical evaluations with on-line spectroscopy,

such as surface-enhanced IR, Raman, differential electrochemical mass spectroscopy, and X-ray absorption spectroscopy, will play a pivotal role in pinning down the nature of confinement in electrocatalysis.[15, 45-46]

Parallel to the suggested surface chemistry efforts, we also emphasize the importance of a highly integrated framework of theory and experimentation. Although this minireview is mainly focused on the experimental progress, close integration of theoretical and experimental investigation is appealing to pinpoint the mechanistic pathways in confined electrocatalysis. For this reason, we anticipate that the well-defined systems such as monodisperse NPs or single-atom catalysts will lead to in-depth understanding and further development to establish a feedback loop for adaptive modelling and prediction.

Regarding the materials system, metals confined in other materials systems beyond CNTs will open new opportunities in precisely tailoring the interplay between active sites and their microenvironment. For example, CNTs usually demonstrate weak interactions with metal centers, while metal oxides may establish strong-metal support interactions at the interface between oxides and metals,[47] enabling efficient electron transfer. We anticipate that by reducing the size of the microenvironment imposed by the cover, the confinement effect may be amplified. Furthermore, the geometric effect, e.g., the porosity, and the size of coating, and the electronic effect, e.g., the charge transfer direction and degree[48] can be precisely controlled and harnessed for catalysis in these well-defined systems.

In summary, electrocatalysis in confined spaces has far-reaching implications in chemistry, materials science, and sustainable energy applications. We believe that advanced and practical electrocatalysts for next-generation chemical and energy devices

can be developed based on the concept of confinement, calling for the understanding of fundamental aspects and precision chemical synthesis.

References

1. Jin, R.; Li, G.; Sharma, S.; Li, Y.; Du, X., Toward Active-Site Tailoring in Heterogeneous Catalysis by Atomically Precise Metal Nanoclusters with Crystallographic Structures. *Chem. Rev.* **2020**.

2. Shifa, T. A.; Vomiero, A., Confined Catalysis: Progress and Prospects in Energy Conversion. *Adv. Energy Mater.* **2019,** *9* (40), 1902307.

3. Greeley, J.; Stephens, I. E. L.; Bondarenko, A. S.; Johansson, T. P.; Hansen, H. A.; Jaramillo, T. F.; Rossmeisl, J.; Chorkendorff, I.; Nørskov, J. K., Alloys of platinum and early transition metals as oxygen reduction electrocatalysts. *Nat. Chem* **2009,** *1* (7), 552-556.

4. Jiao, Y.; Zheng, Y.; Jaroniec, M.; Qiao, S. Z., Origin of the Electrocatalytic Oxygen Reduction Activity of Graphene-Based Catalysts: A Roadmap to Achieve the Best Performance. *J. Am. Chem. Soc.* **2014,** *136* (11), 4394-4403.

5. Li, J.; Alsudairi, A.; Ma, Z.-F.; Mukerjee, S.; Jia, Q., Asymmetric Volcano Trend in Oxygen Reduction Activity of Pt and Non-Pt Catalysts: In Situ Identification of the Site-Blocking Effect. *J. Am. Chem. Soc.* **2017,** *139* (4), 1384-1387.

6. Guo, S.; Li, D.; Zhu, H.; Zhang, S.; Markovic, N. M.; Stamenkovic, V. R.; Sun, S., FePt and CoPt Nanowires as Efficient Catalysts for the Oxygen Reduction Reaction. *Angew. Chem. Int. Ed.* **2013,** *52* (12), 3465-3468.

7. Zhu, H.; Zhang, S.; Guo, S.; Su, D.; Sun, S., Synthetic Control of FePtM Nanorods (M = Cu, Ni) To Enhance the Oxygen Reduction Reaction. *J. Am. Chem. Soc.* **2013,** *135* (19), 7130-7133.

8. Liu, X.; Xiao, J.; Peng, H.; Hong, X.; Chan, K.; Nørskov, J. K., Understanding trends in electrochemical carbon dioxide reduction rates. *Nat. Commun.* **2017,** *8* (1), 15438.

9. Fan, L.; Xia, C.; Yang, F.; Wang, J.; Wang, H.; Lu, Y., Strategies in catalysts and electrolyzer design for electrochemical CO_2 reduction toward C_2 products. *Sci. Adv.* **2020,** *6* (8), eaay3111.

10. Mouarrawis, V.; Plessius, R.; van der Vlugt, J. I.; Reek, J. N. H., Confinement Effects in Catalysis Using Well-Defined Materials and Cages. *Front Chem* **2018,** *6*, 623-623.

11. Xiao, J.; Pan, X.; Guo, S.; Ren, P.; Bao, X., Toward Fundamentals of Confined Catalysis in Carbon Nanotubes. *J. Am. Chem. Soc.* **2015,** *137* (1), 477-482.

12. Miners, S. A.; Rance, G. A.; Khlobystov, A. N., Chemical reactions confined within carbon nanotubes. *Chem. Soc. Rev.* **2016,** *45* (17), 4727-4746.

13. Pan, X.; Bao, X., The Effects of Confinement inside Carbon Nanotubes on Catalysis. *Acc. Chem. Res.* **2011,** *44* (8), 553-562.

14. Li, H.; Xiao, J.; Fu, Q.; Bao, X., Confined catalysis under two-dimensional materials. *Proc. Natl. Acad. Sci.* **2017,** *114* (23), 5930-5934.

15. Fu, Q.; Bao, X., Surface chemistry and catalysis confined under two-dimensional materials. *Chem. Soc. Rev.* **2017,** *46* (7), 1842-1874.

16. Yang, Q.; Xu, Q.; Jiang, H.-L., Metal–organic frameworks meet metal nanoparticles: synergistic effect for enhanced catalysis. *Chem. Soc. Rev.* **2017,** *46* (15), 4774-4808.

17. Peng, H.; Zhang, X.; Han, X.; You, X.; Lin, S.; Chen, H.; Liu, W.; Wang, X.; Zhang, N.; Wang, Z.; Wu, P.; Zhu, H.; Dai, S., Catalysts in Coronas: A Surface Spatial Confinement Strategy for High-Performance Catalysts in Methane Dry Reforming. *ACS Catal.* **2019,** *9* (10), 9072-9080.

18. Wu, S.-M.; Yang, X.-Y.; Janiak, C., Confinement Effects in Zeolite-Confined Noble Metals. *Angew. Chem. Int. Ed.* **2019,** *58* (36), 12340-12354.

19. Yan, Z.; Ji, M.; Xia, J.; Zhu, H., Recent Advanced Materials for Electrochemical and Photoelectrochemical Synthesis of Ammonia from Dinitrogen: One Step Closer to a Sustainable Energy Future. *Adv. Energy Mater.* **2020,** *10* (11), 1902020.

20. Xia, J.; Yang, S.-Z.; Wang, B.; Wu, P.; Popovs, I.; Li, H.; Irle, S.; Dai, S.; Zhu, H., Boosting electrosynthesis of ammonia on surface-engineered MXene Ti_3C_2. *Nano Energy* **2020,** *72*, 104681.

21. Seh, Z. W.; Kibsgaard, J.; Dickens, C. F.; Chorkendorff, I.; Nørskov, J. K.; Jaramillo, T. F., Combining theory and experiment in electrocatalysis: Insights into materials design. *Science* **2017,** *355* (6321), eaad4998.

22. Wei, F.; Wan, Q.; Lin, S.; Guo, H., Origin of Confined Catalysis in Nanoscale Reactors between Two-Dimensional Covers and Metal Substrates: Mechanical or Electronic? *J. Phys. Chem. C* **2020,** *124* (21), 11564-11573.

23. Kiang, C. H.; Endo, M.; Ajayan, P. M.; Dresselhaus, G.; Dresselhaus, M. S., Size Effects in Carbon Nanotubes. *Phys. Rev. Lett.* **1998,** *81* (9), 1869-1872.

24. Xiao, J.; Liu, B.; Huang, Y.; Zuo, J.; Hwang, K. C.; Yu, M. F., Collapse and stability of single- and multi-wall carbon nanotubes. *Nanotechnology* **2007,** *18* (39), 395703.

25. Iijima, S., Helical microtubules of graphitic carbon. *Nature* **1991,** *354* (6348), 56-58.

26. Vikkisk, M.; Kruusenberg, I.; Ratso, S.; Joost, U.; Shulga, E.; Kink, I.; Rauwel, P.; Tammeveski, K., Enhanced electrocatalytic activity of nitrogen-doped multi-walled carbon nanotubes towards the oxygen reduction reaction in alkaline media. *RSC Adv.* **2015,** *5* (73), 59495-59505.

27. Alali, K. T.; Liu, J.; Liu, Q.; Li, R.; Aljebawi, K.; Wang, J., Grown Carbon Nanotubes on Electrospun Carbon Nanofibers as a 3D Carbon Nanomaterial for High Energy Storage Performance. *ChemistrySelect* **2019,** *4* (19), 5437-5458.

28. Kang, J.; Zhang, H.; Duan, X.; Sun, H.; Tan, X.; Liu, S.; Wang, S., Magnetic Ni-Co alloy encapsulated N-doped carbon nanotubes for catalytic membrane degradation of emerging contaminants. *Chem. Eng. J.* **2019,** *362*, 251-261.

29. Oluigbo, C. J.; Xie, M.; Ullah, N.; Yang, S.; Zhao, W.; Zhang, M.; Lv, X.; Xu, Y.; Xie, J., Novel one-step synthesis of nickel encapsulated carbon nanotubes as efficient electrocatalyst for hydrogen evolution reaction. *Int. J. Hydrog. Energy* **2019,** *44* (5), 2685-2693.

30. Ma, W.; Xie, S.; Liu, T.; Fan, Q.; Ye, J.; Sun, F.; Jiang, Z.; Zhang, Q.; Cheng, J.; Wang, Y., Electrocatalytic reduction of CO_2 to ethylene and ethanol through hydrogen-assisted C–C coupling over fluorine-modified copper. *Nat. Catal* **2020,** *3* (6), 478-487.

31. Zhang, Z.; Chi, M.; Veith, G. M.; Zhang, P.; Lutterman, D. A.; Rosenthal, J.; Overbury, S. H.; Dai, S.; Zhu, H., Rational Design of Bi Nanoparticles for Efficient Electrochemical CO_2 Reduction: The Elucidation of Size and Surface Condition Effects. *ACS Catal.* **2016,** *6* (9), 6255-6264.

32. Wang, B.; Yang, S.-Z.; Chen, H.; Gao, Q.; Weng, Y.-X.; Zhu, W.; Liu, G.; Zhang, Y.; Ye, Y.; Zhu, H.; Li, H.; Xia, J., Revealing the role of oxygen vacancies in bimetallic PbBiO2Br atomic layers for boosting photocatalytic CO_2 conversion. *Appl. Catal. B* **2020,** *277*, 119170.

33. Liu, S.; Sun, C.; Xiao, J.; Luo, J.-L., Unraveling Structure Sensitivity in CO_2 Electroreduction to Near-Unity CO on Silver Nanocubes. *ACS Catal.* **2020,** *10* (5), 3158-3163.

34. Zhu, S.; Wang, Q.; Qin, X.; Gu, M.; Tao, R.; Lee, B. P.; Zhang, L.; Yao, Y.; Li, T.; Shao, M., Tuning Structural and Compositional Effects in Pd–Au Nanowires for Highly Selective and Active CO_2 Electrochemical Reduction Reaction. *Adv. Energy Mater.* **2018,** *8* (32), 1802238.

35. Yang, F.; Elnabawy, A. O.; Schimmenti, R.; Song, P.; Wang, J.; Peng, Z.; Yao, S.; Deng, R.; Song, S.; Lin, Y.; Mavrikakis, M.; Xu, W., Bismuthene for highly efficient carbon dioxide electroreduction reaction. *Nat. Commun.* **2020,** *11* (1), 1088.

36. Cui, M.; Johnson, G.; Zhang, Z.; Li, S.; Hwang, S.; Zhang, X.; Zhang, S., AgPd nanoparticles for electrocatalytic CO_2 reduction: bimetallic composition-dependent ligand and ensemble effects. *Nanoscale* **2020,** *12* (26), 14068-14075.

37. Yin, Z.; Palmore, G. T. R.; Sun, S., Electrochemical Reduction of CO_2 Catalyzed by Metal Nanocatalysts. *Trends Chem.* **2019,** *1* (8), 739-750.

38. Zhu, W.; Zhang, Y.-J.; Zhang, H.; Lv, H.; Li, Q.; Michalsky, R.; Peterson, A. A.; Sun, S., Active and Selective Conversion of CO_2 to CO on Ultrathin Au Nanowires. *J. Am. Chem. Soc.* **2014,** *136* (46), 16132-16135.

39. Sharma, P. P.; Wu, J.; Yadav, R. M.; Liu, M.; Wright, C. J.; Tiwary, C. S.; Yakobson, B. I.; Lou, J.; Ajayan, P. M.; Zhou, X.-D., Nitrogen-Doped Carbon Nanotube Arrays for High-Efficiency Electrochemical Reduction of CO_2: On the Understanding of Defects, Defect Density, and Selectivity. *Angew. Chem. Int. Ed.* **2015,** *54* (46), 13701-13705.

40. Wu, J.; Yadav, R. M.; Liu, M.; Sharma, P. P.; Tiwary, C. S.; Ma, L.; Zou, X.; Zhou, X.-D.; Yakobson, B. I.; Lou, J.; Ajayan, P. M., Achieving Highly Efficient, Selective, and Stable CO_2 Reduction on Nitrogen-Doped Carbon Nanotubes. *ACS Nano* **2015,** *9* (5), 5364-5371.

41. Zheng, W.; Guo, C.; Yang, J.; He, F.; Yang, B.; Li, Z.; Lei, L.; Xiao, J.; Wu, G.; Hou, Y., Highly active metallic nickel sites confined in N-doped carbon nanotubes toward significantly enhanced activity of CO_2 electroreduction. *Carbon* **2019,** *150*, 52-59.

42. Hou, Y.; Liang, Y.-L.; Shi, P.-C.; Huang, Y.-B.; Cao, R., Atomically dispersed Ni species on N-doped carbon nanotubes for electroreduction of CO_2 with nearly 100% CO selectivity. *Appl. Catal. B* **2020,** *271*, 118929.

43. Wen, Z.; Ci, S.; Zhang, F.; Feng, X.; Cui, S.; Mao, S.; Luo, S.; He, Z.; Chen, J., Nitrogen-enriched core-shell structured Fe/Fe(3)C-C nanorods as advanced electrocatalysts for oxygen reduction reaction. *Adv. Mater.* **2012,** *24* (11), 1399-1404.

44. Jia, J.; Yang, H.; Wang, G.; Huang, P.; Cai, P.; Wen, Z., Fe/Fe3C Nanoparticles Embedded in Nitrogen-Doped Carbon Nanotubes as Multifunctional Electrocatalysts for Oxygen Catalysis and CO_2 Reduction. *ChemElectroChem* **2018,** *5* (3), 471-477.

45. Gao, Q.; Mou, T.; Liu, S.; Johnson, G.; Han, X.; Yan, Z.; Ji, M.; He, Q.; Zhang, S.; Xin, H.; Zhu, H., Monodisperse PdSn/SnOx core/shell nanoparticles with superior electrocatalytic ethanol oxidation performance. *J. Mater. Chem. A* **2020,** *8* (40), 20931-20938.

46. Dai, H., Carbon nanotubes: opportunities and challenges. *Surf. Sci.* **2002,** *500* (1), 218-241.

47. Wu, P.; Tan, S.; Moon, J.; Yan, Z.; Fung, V.; Li, N.; Yang, S.-Z.; Cheng, Y.; Abney, C. W.; Wu, Z.; Savara, A.; Momen, A. M.; Jiang, D.-e.; Su, D.; Li, H.; Zhu, W.; Dai, S.; Zhu, H., Harnessing strong metal–support interactions via a reverse route. *Nat. Commun.* **2020,** *11* (1), 3042.

48. Wu, P.; Wu, Z.; Mullins, D. R.; Yang, S.-Z.; Han, X.; Zhang, Y.; Foo, G. S.; Li, H.; Zhu, W.; Dai, S.; Zhu, H., Promoting Pt catalysis for CO oxidation via the Mott–Schottky effect. *Nanoscale* **2019,** *11* (40), 18568-18574.

CHAPTER 4

Ag-modified Cu nanocubes for CO_2 electroreduction

4.1 Introduction

In Chapter 2, we emphasized our work on electrochemical CO_2 reduction reaction to C_1 products. We synthesized heterostructured Bi-Cu_2S nanocrystals for enhancing electrocatalytic performance toward formate. However, we are always keeping a question in mind: how to go beyond the C_1 products. The most attractive goal of electrochemical CO_2 reduction is to generate C_2 and C_{2+} products, such as ethylene, ethanol, n-propanol, etc. Among these CO_2 reduction products, alcohols are highly desirable because of their high industrial value and ease of transportation and storage.

Previous studies showed that Cu had shown promising catalytic performance toward CO_2 reduction to C_2 products. However, it is shown that CO_2 reduction on Cu has poor selectivity and stability, leading to an open question for catalyst design that can improve performance. In recent years, a rising topic called "tandem catalysis" has attracted researchers' attention. Tandem catalysis is a type of alloy that combines multiple metal species in the catalyst, which utilizes the promising property of these metals. This idea can also be applied to the reaction of CO_2 reduction. Chen et al. designed Cu-Ag tandem catalysts that can enhance C_2 production rate by first reducing CO_2 to CO on Ag and then forming the C-C bonds on Cu.[1] Another recent work showed that Au/Cu is in favor of ethanol production.[2] This catalyst exhibits higher synergistic activity and selectivity on C2 production than either Au or Cu compartment, indicating that tandem catalysis plays a key role in Au/Cu system.

Moreover, it has been widely accepted that *CO (* denotes surface adsorbate) and *CO related intermediates are crucial for CO_2RR toward multicarbons. Cu is known to have moderate adsorption of *CO based intermediates, which is good for keeping *CO on the surface and enabling further reduction. However, the reduction of CO_2 to CO on Cu is weak due to the poor ability of activation of CO_2, leading to a less *CO reservoir for C-C coupling to produce C_2 products. In contrast, Ag and Au, which are coinage metals, show a strong ability to reduce CO_2 to CO, typically with very high activity and selectivity, due to the strong ability to activate CO_2 under electrochemical reaction conditions. Thus, Cu-based bimetallic tandem platforms have been invoked for CO_2RR, which utilizes Ag or Au as one of the metal species to activate CO_2 and reduce it to *CO, and couple with Cu for the strong ability of C-C coupling to further produce C_2 products.

4.2 Catalyst design

The catalyst was developed a controllable way to dope the Ag into Cu lattice by using a wet-chemical method. By controlling the Ag ratio and reaction temperature, we are able to obtain different structures of CuAg bimetallic catalysts. First, we add the solvent, reducing agent, and Cu precursors into a reactor, then increase to a certain temperature to get Cu nanocubes. After that, the Ag precursor is injected into the reactor. With a low Ag ratio, we can get Cu/CuAg core-shell structure which means Ag doped into Cu lattice. As the Ag doping ratio increases, it can form the ordered intermetallic Cu/CuAg SSA. By using this wet-chemistry synthetic method, we are able to achieve two different structures of CuAg nanocubes (**Figure 4.1**). We are still waiting for the characterization results of Cu/CuAg ordered SAA. In this case, I'll mainly focus on Cu/CuAg core-shell nanocubes.

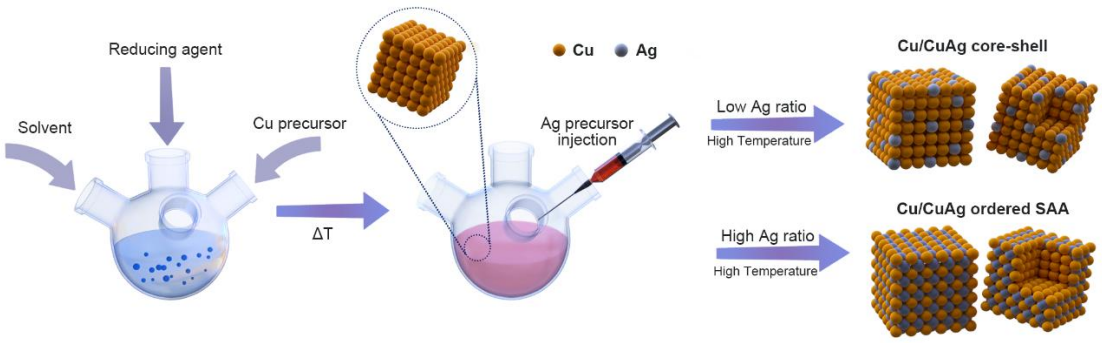

Figure 4.1 Synthesizing method of single atom Ag doped into Cu lattice.

The TEM images of the as-synthesized Cu/CuAg core-shell nanocubes (**Figure 4.2, and Figure 4.3a**) show that Cu/CuAg core-shells are cubic morphology with the size of 35-40 nm. To get further insight into the distribution of Ag and Cu in the as-synthesized Cu/CuAg nanocubes, elemental analysis was carried out with scanning transmission electron microscopy (STEM). **Figure 4.3b** shows a high-angle annular dark-field scanning transmission electron microscopy (HAADF-STEM) image and the elemental mapping of a representative Cu/CuAg nanocube. We observed that Cu mainly enriches in the core while Ag distributes on the surface of Cu, forming a CuAg shell. A clear interfacial boundary was observed in a bright-field (BF) STEM image (**Figure 4.3c**), suggesting the CuAg layers cover the Cu nanocube core. The X-ray diffraction (XRD) pattern (**Figure 4.4**) of the Cu/CuAg core-shell nanocubes demonstrates diffraction peaks that match well with the Cu *fcc* phase.

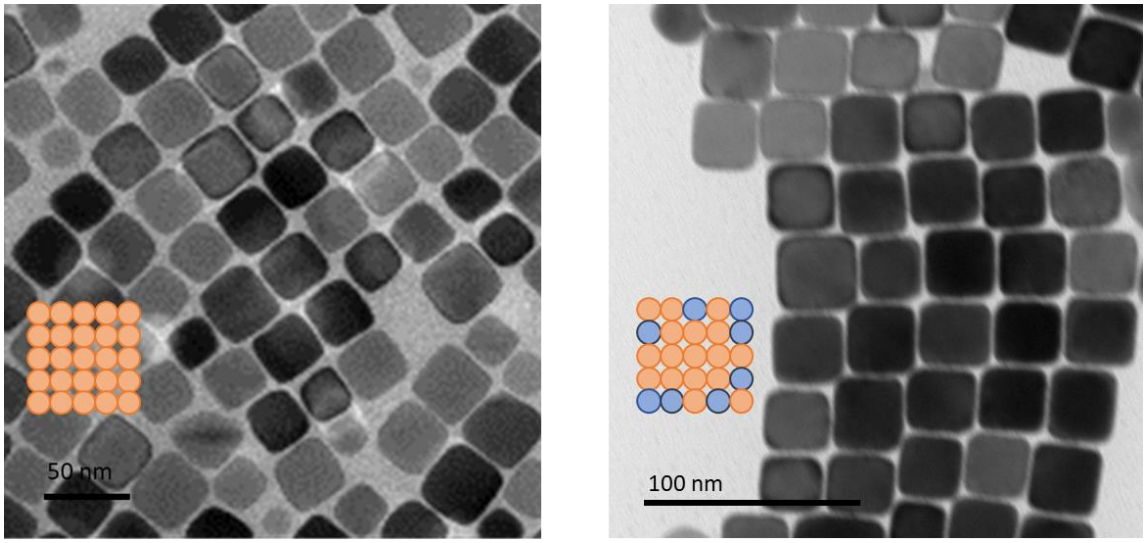

Figure 4.2 TEM images of a) Cu nanocubes. b) Cu/CuAg core-shell structure.

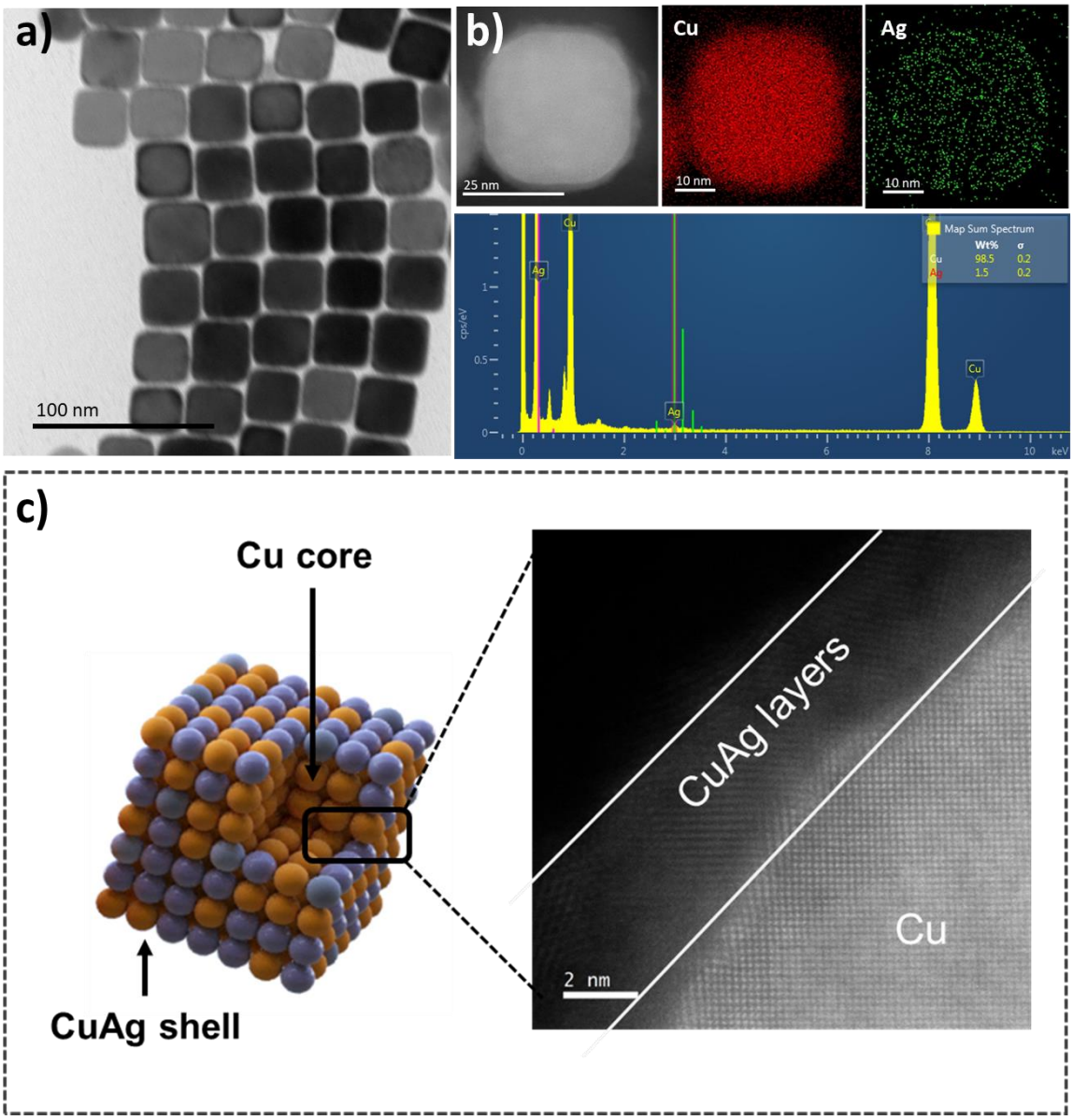

Figure 4.3 (a) Structural characterizations of Cu/CuAg core-shell nanocrystals. (a) TEM images; (b) The STEM-HAADF image and the corresponding X-EDS mappings of Cu/CuAg core-shell. (c) Schematic illustration of the CuAg shell covered on Cu core.

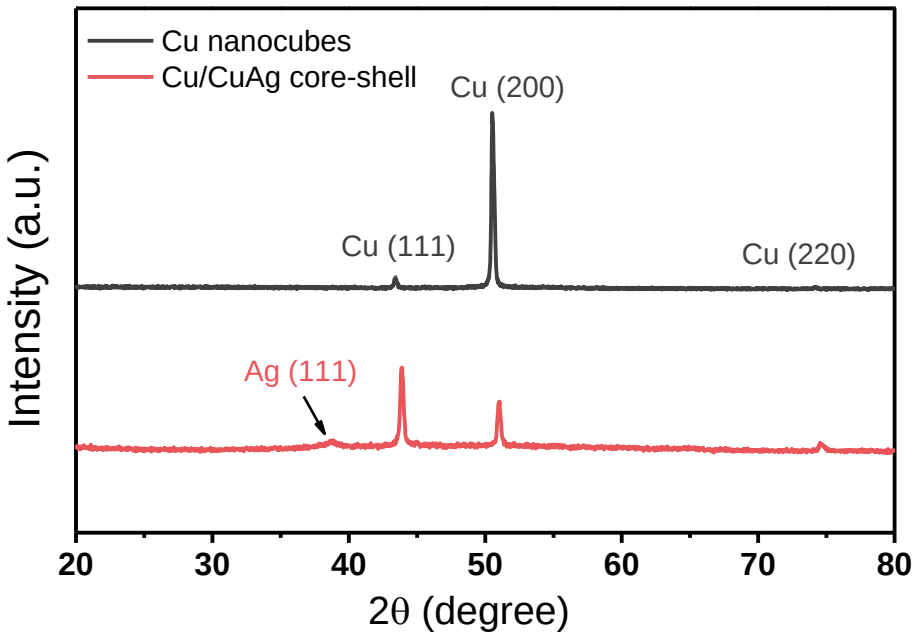

Figure 4.4 XRD patterns of Cu nanocubes and synthesized Cu/CuAg core-shell nanocubes.

4.3 Electrocatalytic performance of Cu/CuAg core-shell catalysts

Electrochemical CO_2 reduction reaction was conducted in 0.1 M $KHCO_3$ in a H-type cell. In this report, we tested Cu/CuAg core-shell catalysts compared to the Cu nanocubes (NCs) reference. Cu/CuAg core-shell catalysts demonstrated higher ethylene and ethanol selectivity at lower overpotential. **In Figure 4.5a**, compared to Cu NCs, Cu/CuAg core-shell catalysts generate more CO at the same potential, indicating Ag could facilitate to create a CO-rich environment in the electrolysis system. And the Cu/CuAg core-shell catalysts begin to generate C_2H_4 at the potential of -1.1 V vs. RHE, while there is no C_2 formation on Cu NCs at the same potential. By increasing the applied potential to -1.2 V, C_2H_4 is detected in Cu NCs system. Meanwhile, Cu/CuAg core-shell could enhance the electrocatalytic activity on ethanol production. It can achieve 7.9% of FE of ethanol at -1.4 V, which is about a three-fold ethanol yield on Cu NCs. In **Figure 4.5b**, the higher FE of C_2 products on Cu/CuAg core-shell at a wide range of potential windows indicates that Ag doped into Cu lattice shows the tandem effects for promoting C_2 formation in electrochemical CO_2 reduction.

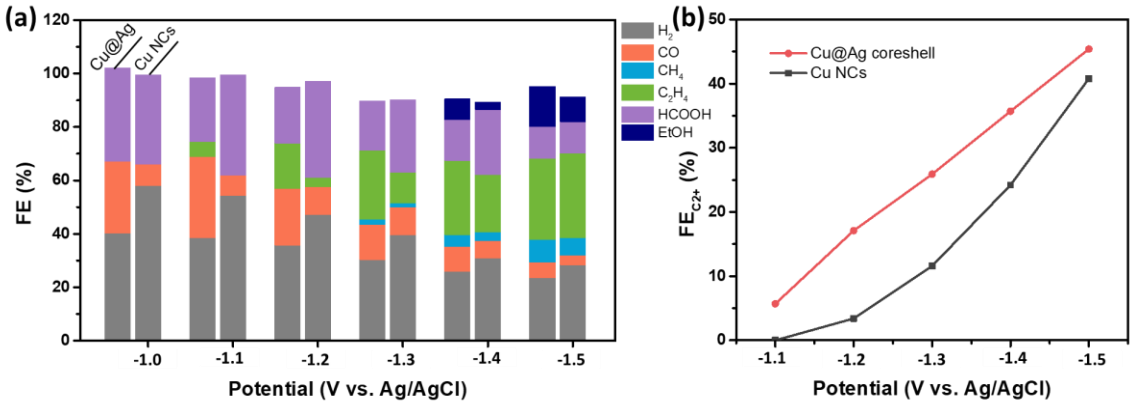

Figure 4.5 ECO_2RR performance on Cu nanocubes catalyst and CuAg core-shell catalyst: a) FE for ECO_2RR. b) FE of C_2 formation at various applied potentials.

4.4 Investigation of Ag stabilized Cu lattice

To investigate the structural evolution of Cu/CuAg core-shell catalyst during the CO_2 reduction process, in situ XAFS was performed. **Figure 4.6a** shows the Cu K-edge X-ray absorption near-edge structure (XANES) spectra of Cu/CuAg core-shell nanocubes and the reference (Cu foil). When the potential from -0.6 to -0.9 V was applied, XANES shifted toward lower energy and the intensity of white lines decreased, indicating the oxidized Cu is reduced to metallic Cu. Ag L_3-edge spectra **Figure 4.6b** show no oxidation state change as Ag is very stable and always maintains the metallic Ag. Furthermore, the extended-XAFS spectra (**Figure 4.7**) that show the same changes that the Cu-O bond disappeared with an intensifying metallic Cu-Cu bond. Besides, The EXAFS fitting shows the presence of metallic Cu at -0.8 V and -0.9 V, indicating that the metallic Cu serves as catalytic active sites for CO_2RR.

To further elucidate whether the incorporation of Ag into Cu could chemically improve the structural stability of Cu lattice, we tested 5 hours of stability at -1.2 V (**Figure 4.8**). The results showed that Cu NCs need 150 min activation time to reach stable FE toward C_2H_4. But there is no activation step needed for Cu/CuAg core-shell in the electroreduction of CO_2 to C_2H_4. It can reach a maximum C_2H_4 yield at the beginning and no degradation during the reaction. When increasing the potential to -1.4 V, Cu NCs need less time to activate the catalyst surface, and it reaches a stable C_2H_4 production after 1.5 h. Combining the XAFS results that metallic Cu is the active site of CO_2RR, Cu nanocubes need more activation time to reduce to metallic Cu to generate ethylene. These results indicate that Ag doped into Cu could stabilize the Cu lattice and prevent the oxidation of Cu.

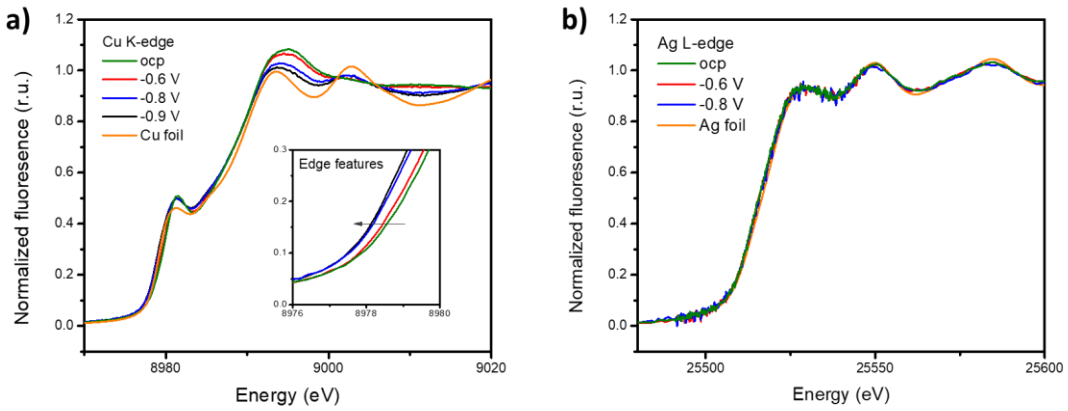

Figure 4.6 Structural characterizations of the Cu/CuAg core-shell nanocubes. a) Cu K-edge in situ XANES spectra of Cu/CuAg nanocubes and Cu foil reference, with a zoomed view of the Cu K-edge as inset. b) Ag L_3-edge in situ XANES spectra of Cu/CuAg nanocubes and Ag foil reference.

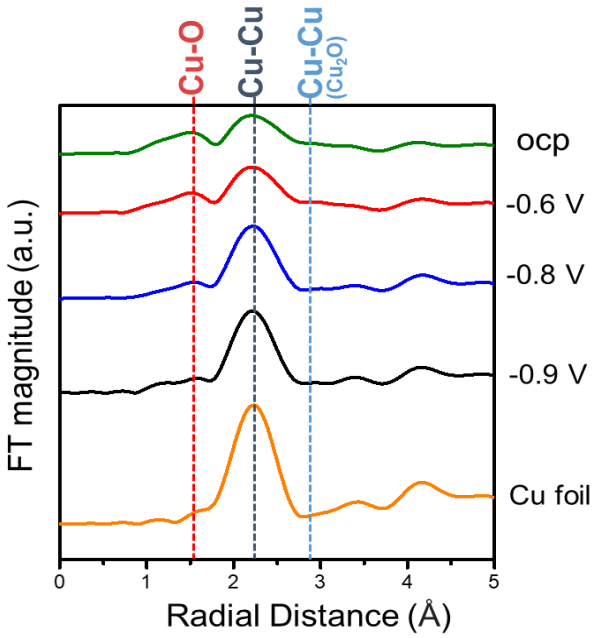

Figure 4.7 EXAFS Fourier transformed k_3-weighted $\chi(k)$ function spectra of Cu/CuAg nanocubes and Cu foil reference..

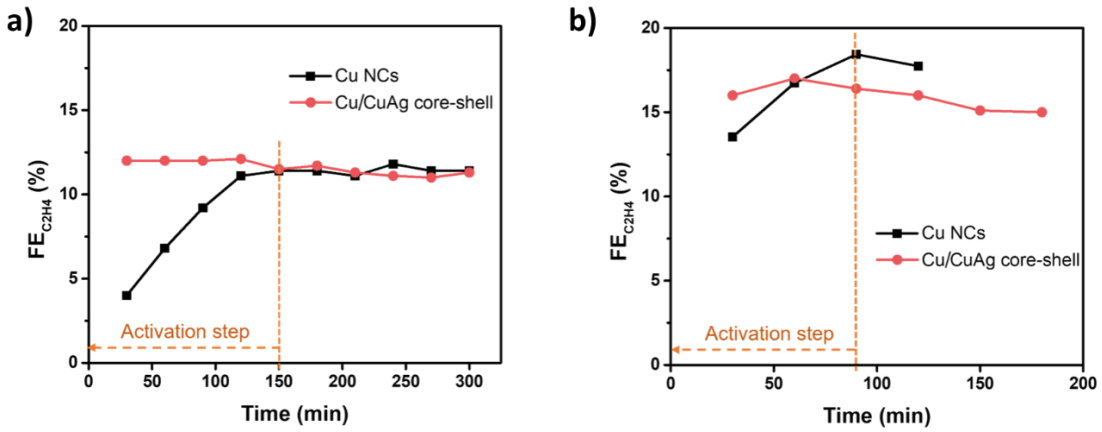

Figure 4.8 Faradic efficiency toward C_2H_4 on Cu/CuAg core-shell catalyst and Cu NCs at a) -1.2 V (b) -1.4 V.

References

1. Chen, C.; Li, Y.; Yu, S.; Louisia, S.; Jin, J.; Li, M.; Ross, M. B.; Yang, P., Cu-Ag Tandem Catalysts for High-Rate CO_2 Electrolysis toward Multicarbons. *Joule* **2020,** *4* (8), 1688-1699.

2. Morales-Guio, C. G.; Cave, E. R.; Nitopi, S. A.; Feaster, J. T.; Wang, L.; Kuhl, K. P.; Jackson, A.; Johnson, N. C.; Abram, D. N.; Hatsukade, T.; Hahn, C.; Jaramillo, T. F., Improved CO_2 reduction activity towards C_{2+} alcohols on a tandem gold on copper electrocatalyst. *Nat. Catal* **2018,** *1* (10), 764-771.

CHAPTER 5

Machine learning of lateral adsorbate interactions in surface reaction kinetics

5.1 Introduction

Lateral adsorbate inte ractions on solid surfaces play a crucial role in heterogeneous catalysis, self-assembly, nucleation and growth, and many interfacial phenomena governed by molecular processes [1]. For instance, the outcome of a surface-catalyzed reaction can be greatly influenced by introducing chemical additives as coadsorbed modifiers which promote or inhibit the transformation of kinetically significant intermediates. As being increasingly recognized, intrinsic reaction intermediates at noticeable coverages often synergistically regulate the catalytic cycle with active sites in a self-adjusting manner [2,3]. At the most fundamental level, an ensemble of adsorbate-adsorbate configurations collectively renders the local environment of reacting species by substrate-mediated electronic couplings and through-space electrostatic interactions [4,5], or direct orbital overlaps in some cases [6]. Experimentally, it is possible but remains challenging to measure interaction energies of adsorbates on single-crystal surfaces under ultrahigh vacuum conditions. However, the so-called pressure and materials gaps prevent the generalization of attained knowledge to industrial operating conditions [7]. In this regard, computational chemistry with a vast array of sophisticated tools is invaluable in describing the structure and energetics of complex systems [8]. Particularly, density functional theory (DFT) has proved to be reasonably accurate for capturing kinetic parameters of elementary steps occurring at active sites while considering lateral adsorbate interactions in an ad hoc fashion. The practicability and maturity of this approach have reached such a level that

rudimentary energy analyses of reaction pathways can often tell us whether a material candidate can selectively catalyze desired chemical transformations.

To provide truly actionable insights for guiding the design of high-performance catalytic systems, rigorous kinetic analysis is required. With recent advances in computing infrastructures and numerical algorithms, kinetic modeling of surface reactions has gained popularity because it directly links atomistic processes with macroscopic observables under relevant conditions [9]. Among various practiced techniques, microkinetic modeling (MKM) with the Brønsted-Evans-Polanyi (BEP) and linear adsorption-energy scaling relationships is widely used in heterogeneous catalysis by mapping the catalytic outcome of surface reactions onto reactivity descriptors, e.g., adsorption energies of key intermediates or their derivatives [10]. It has been shown that when applying the adsorbate interactions to kinetic studies, catalytic reaction pathways and microkinetic predictions like turnover frequency, selectivity and apparent activation energies are different, highlighting the generic consequences of lateral interactions [11]. Although lateral adsorbate interactions can be included in energetics, the spatial distribution of adsorbates on a catalytic surface is not explicitly considered because of the inherent mean-field approximation [12,13]. To go beyond the mean-field treatment [14,15], one of the common approaches is solving a stochastic Markov process within a lattice-based kinetic Monte Carlo (kMC) framework. However, it is not feasible to directly compute energetics of every MC step from quantum mechanics across experimentally relevant time and length scales [16]. To address this dilemma, developing surrogate models by learning from ab initio data has become an emerging research frontier of fundamental catalysis [17,18]. Herein, we survey the machine learning (ML) algorithms for predicting lateral adsorbate interactions on solid surfaces, e.g.,

transition metals, ranging from analytic linear relationships, to ML-parameterized cluster expansions, and to highly nonlinear deep learning models (Figure 1). We will also discuss prospects and foreseeable challenges in implementing generalizable ML techniques in operando computational modeling of surface reaction kinetics.

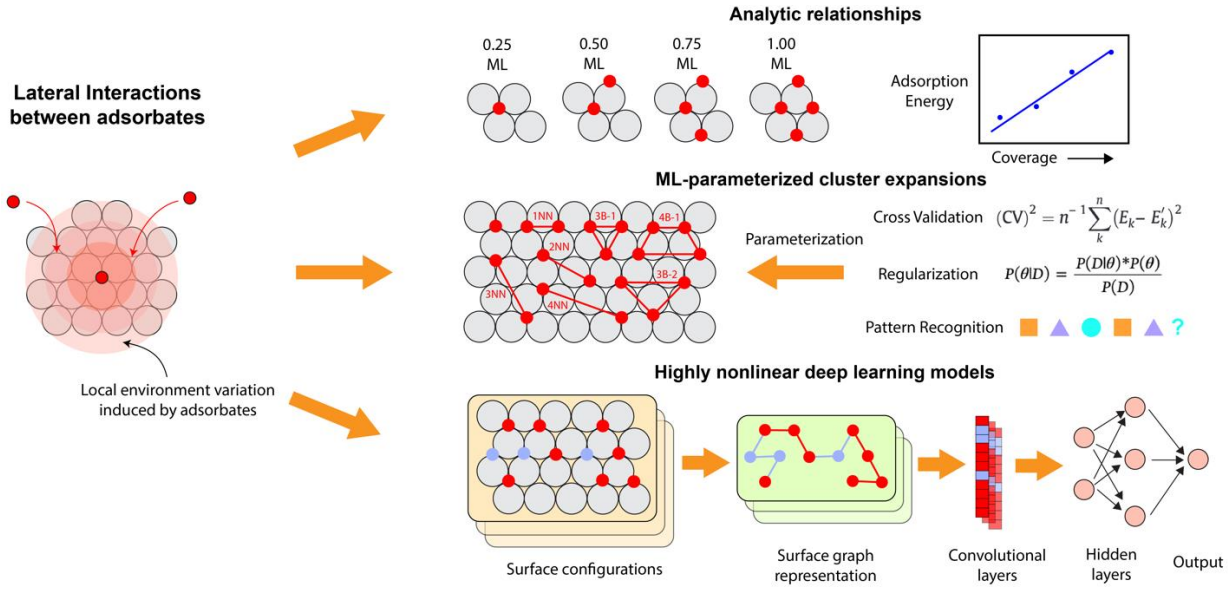

Figure 5.1. Lateral adsorbate interactions can be considered as the change of the binding energy for a given adsorbate in response to a perturbation of its local environment by co-adsorbates. Analytic relationships between the average (or differential) adsorption energies and the coverage have been employed to determine lateral adsorbate interactions in simple scenarios. Another way that has been widely used is ML-parameterized (cross validation, regularization, pattern recognition, etc.) cluster expansions (CEs). An emerging approach is using highly nonlinear deep learning models, e.g., graph convolutional neural networks (GCNNs), to predict adsorption energies after seeing a large amount of surface configurations by the algorithms.

5.2 Analytic relationships

To include adsorbate coverage effects in microkinetic modeling, analytic relationships have been developed to describe adsorption energies and reaction barriers as a function of coverages [19–23]. The analytic relationships do not contain any machine learning aspects but serve as the initial idea of ways to consider the adsorbate interactions. Grabow et al. [20] found that the differential binding energy changes linearly with the coverage after a certain threshold and applied the piecewise linear model to the kinetic studies of CO oxidation (Figure 2a and b). The activity volcano plot as a function of O and CO binding energies at the low coverage limit is shown in Figure 2c. It was concluded that adsorbate-adsorbate interactions significantly increase the activity of strong binding metals (the bottom left corner of the volcano), but the interactions do not change the relative activity of different metals and have a very small influence on top right corner of the volcano, that is, on which one is the best elemental metal catalyst. Liu et al. [23] studied the coverage effect of *CO for CO_2 electroreduction on Pd surfaces. The differential CO adsorption energy has a linear relationship with the CO coverage (Figure 2d). With the consideration of the adsorbate-adsorbate interactions, the experimentally measured activity trend of four surface terminations, i.e., Pd(111), Pd(100), Pd(110), and Pd(211), can be well captured by theoretical onset potentials (Figure 2e and f). Formulations of coverage and binding energy beyond linear relationships have also been previously employed in microkinetic models [24,25], emphasizing the importance of considering the linear or beyond linear coverage effects in surface reaction kinetics.

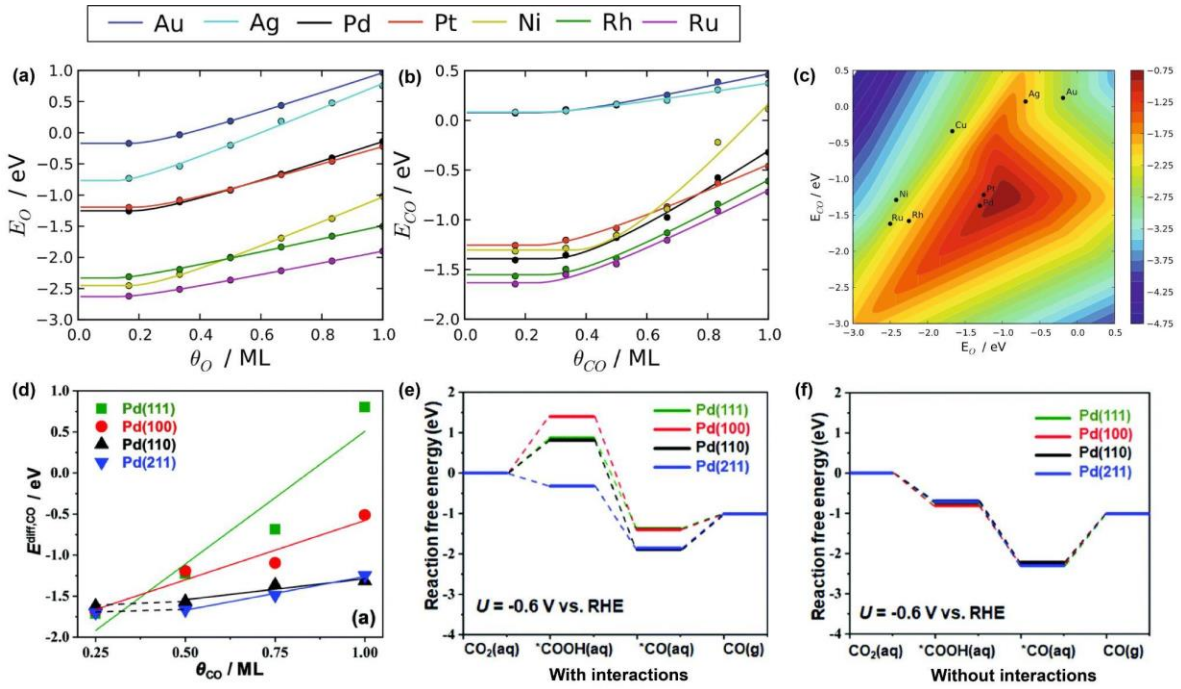

Figure 5.2. Coverage-dependent binding energies for O and CO on fcc(111) of seven transition metals are shown in (a) and (b), respectively [20]. (c) It shows the contour plot of the CO oxidation activity (defined as $k_B T \cdot ln(r/\nu)$, $\nu = k_B T/h$) under high-temperature conditions (T = 600 K, P_{O_2}= 0.33 bar, P_{CO}= 0.67 bar, P_{CO_2}= 1 bar) as a function of the O and CO adsorption energies at the low coverage limit [23]. The differential adsorption energies of CO on Pd(111), Pt(100), Pt(110) and Pt(211) surfaces as a function of the coverage of CO [23]. The reaction pathways of CO_2 electroreduction to CO at the applied potential (-0.6 V vs. RHE) with and without the consideration of adsorbate-adsorbate interactions are shown in (e) and (f), respectively [23].

5.3 ML-parameterized cluster expansions

Lateral adsorbate interactions can be considered in kMC simulations by employing cluster expansions (CEs), one common type of lattice-gas models with parameterized Hamiltonians. The CE based models are physical models and not ML methods but determining Hamiltonians in CE based models employs ML methods for fast and accurate parameterization. Wu et al. [26] first applied CEs in kinetic models to estimate the catalytic rates, and CEs gained popularity with different frameworks (ATAT, UNCLE, ICET, Zacros, kmos, etc.) [27–30] developed and applied to surface catalytic reactions, e.g., NO oxidation reaction, CO oxidation, and Fischer-Tropsch synthesis [12,26,31–34]. CEs have advantages over simplified linear models since they can predict energetics of elementary steps with the consideration of the spatial environment of surface species on lattice sites [35]. The origin of cluster expansions can be traced back to the early 1950s, when Kikuchi [36] developed an Ising model-based cluster variation method to study order-disorder phenomena. In 1984, Sanchez et al. [37] developed a general formalism for the description of configurational cluster expansions in terms of a complete basis set expansion. In simple terms, CE decomposes the energy of a configuration into one-body, two-body, and higher-order interaction terms (‘clusters’), and each term has a corresponding weight called effective cluster interaction (ECI) analogous to the interaction strength [38]. The energy can be exactly reproduced only if all clusters are included in the CE. However, the ECIs for clusters that contain a large number of sites or a large distance between sites are usually negligible. Therefore, the CEs can be truncated to a sum over finite numbers of cluster functions with little loss of accuracy.

The construction of CEs includes data generation by DFT calculations, structure selection and cluster selection. When referring to surface reactions, the training becomes more challenging due to the loss of translational symmetry at the interface and the increase of the complexity of adsorbate interactions and the number of surface species. While DFT calculations typically require a large number of computational resources, it has become more or less standardized in catalysis research. In contrast, the algorithms driving structure selection and cluster selection are arguably more critical to the overall accuracy of the CEs. Therefore, significant efforts have been put into developing approaches to generate effective clusters for a given training set. The goal of the selection algorithm is to find the clusters that have physical contributions to lateral interactions. Early CEs relied on heuristic methods to manually select clusters, while recent approaches incorporate automated ML approaches to systematically optimize the selection process. Multiple automated selection algorithms have been developed for CEs including MIT Ab-initio Phase Stability (MAPS) [27], genetic algorithm (GA) [39,40], and steepest descent (SD) [41], which incorporate various well-established ML approaches such as cross validation [27,42], feature selection, pattern recognition [43], and regularization [44–46]. Pattern recognition has been employed by Vignola et al. [43] to develop a set of ML tools to produce unbiased cluster expansions. They developed an approach which is based on the pattern recognition algorithm to automatically determine model Hamiltonians for a given system. Bayesian optimization, as one of the regularization approaches, has been widely applied to CE models [44–46].

5.4 Deep learning models

When aiming for kinetic studies of more complex surface reactions such as CO methanation, partial methane oxidation, or the Fischer-Tropsch reaction with diverse surface species and adsorption modes, the cluster expansion approach is fundamentally limited by the number of required calculations, since the number of surface configurations grows exponentially with the number of adsorbate species. Even a simple case with *NO and *O adsorbates on Pt(111) have enormous configurations [33]. For low symmetry surfaces with various types of active sites, such as kinks and steps [12,13,47,48], and multi-elemental alloys [49], the loss of translational symmetry causes a drastic increase of configurations and clusters needed to determine model Hamiltonians. The problem is exacerbated when multidentate species adsorb on surfaces, since current CEs applications are only limited to simple adsorbates that can be directly mapped to individual active sites. Thus, researchers introduced surrogate models by using machine learning methods, which rely on flexible and often non-linear models that are trained from reference material data to predict desired material properties. Many machine learning models employing neural networks and various algorithms have been developed to estimate adsorbate interactions [50–52]. As a subset of machine learning models, graph-based convolutional neural network frameworks can directly learn material properties from crystal structures. The reference structures are converted into crystal graph features, and then connected with convolution, pooling layers, and the fully-connected network to predict the target properties. Graph-based deep learning methods have huge advantages when dealing with low symmetry surfaces and multidentate adsorbates compared to CEs, since the featurization automatically learns the structural information, and the nature of non-linearity improves the accuracy.

5.5 Prospects and future challenges

Although ML of lateral adsorbate interactions has proved to be useful in modeling surface reaction kinetics, there are important challenges toward the development of highly accurate, data-driven models that can be flexibly generalized across the chemistry and materials space. For surface reactions involving simple adsorbates, e.g., monatomic or diatomic species, CEs are highly promising for parameterizing interaction energies of effective clusters with limited training data. However, the use of deep learning as a generic framework in modeling complex surface interactions is clear for moving the catalysis field forward. The challenge of data generation can be partially alleviated by strategic sampling algorithms, e.g., active learning [53]. In this aspect, uncertainty quantification of model predictions [54] is particularly important for not only refining model predictions but also providing meaningful statistics in kinetic modeling. While the purely data-driven models have advantages when tackling diverse surface configurations, they lose interpretability of adsorbate-adsorbate interactions which are valuable for rationally designing catalysts with promoters or surface modifiers. In this aspect, physical models have some merits by considering the electronic structure of adsorbates and adsorption sites to obtain an analytic expression, which can reduce the number of data samples needed for parameterization [55]. Physical understanding of adsorbate-adsorbate interactions often starts from the change of surface *d*-band characteristics upon the perturbation from adsorbate frontier orbitals [56]. Xin and Linic [5] interpreted complex interactions on metal surfaces in terms of tractable energy contributions, i.e., one-electron interaction, electrostatic interaction, and polarization, all of which can be evaluated independently to identify the dominating mode of interactions that governs surface reactivity trends. Hoffmann et al. [55] developed a general framework

that predicts the magnitude of adsorbate-adsorbate interactions based on the precalculated electronic structure properties, such as the *d*-band center and the Bader charge. The framework is able to predict differential adsorption energies of an adsorbate at different coverages without explicitly sampling a large amount of surface configurations, which makes the kinetic studies feasible even with multiple adsorbate species. Although these studies provide valuable insights toward understanding lateral interactions, physical models have limited accuracy and typically need electronic structure information that adds to the computational overhead. Improving the interpretability of purely data-driven models by the consideration of physically meaningful interactions [57] could be a potential solution to accurately predict lateral adsorbate interactions in surface reaction kinetics. Leveraging physics-based models and knowledge in deep learning might prove to be fruitful but appears difficult at this stage because of the complexity of adsorbate-adsorbate interactions across the chemistry and materials space. Its realization will likely need new developments of the high-level featurization of surface configurations [58], integrated architecture design of deep neural networks [57], and theoretical advances of chemical interactions at solid surfaces [59].

References

1. Chorkendorff, I. & Niemantsverdriet, J. W. *Concepts of Modern Catalysis and Kinetics*. **2007**.

2. Demir, B. *et al.* A self-adjusting platinum surface for acetone hydrogenation. *Proc. Natl. Acad. Sci. U. S. A.* **2020,** *117*, 3446–3450.

3. Wang, Y., Tang, Y.-J. & Zhou, K. Self-Adjusting Activity Induced by Intrinsic Reaction Intermediate in Fe-N-C Single-Atom Catalysts. *J. Am. Chem. Soc.* **2019,** *141*, 14115–14119.

4. Mortensen, J. J., Hammer, B. & Nørskov, J. K. Alkali Promotion of N_2 Dissociation over Ru(0001). *Phys. Rev. Lett.* **1998**, *80*, 4333.

5. Xin, H. & Linic, S. Analyzing relationships between surface perturbations and local chemical reactivity of metal sites: Alkali promotion of O_2 dissociation on Ag (111). *J. Chem. Phys.* **2016**, *144*, 234704.

6. Liu, Z.-P. & Hu, P. An Insight into Alkali Promotion: A Density Functional Theory Study of CO Dissociation on K/Rh (111). *J. Am. Chem. Soc.* **2001**, *123*, 12596–12604.

7. Stampfl, C., Veronica Ganduglia-Pirovano, M., Reuter, K. & Scheffler, M. Catalysis and corrosion: the theoretical surface-science context. *Surf. Sci.* **2002**, *500*, 368–394.

8. Grajciar, L. *et al.* Towards operando computational modeling in heterogeneous catalysis. *Chem. Soc. Rev.***2018**, *47*, 8307–8348.

9. Matera, S., Schneider, W. F., Heyden, A. & Savara, A. Progress in Accurate Chemical Kinetic Modeling, Simulations, and Parameter Estimation for Heterogeneous Catalysis. *ACS Catal.***2019**, *9*, 6624–6647.

10. Nørskov, J. K., Abild-Pedersen, F., Studt, F. & Bligaard, T. Density functional theory in surface chemistry and catalysis. *Proc. Natl. Acad. Sci. U. S. A.* **2011**, *108*, 937–943.

11. Goswami, A., Ma, H. & Schneider, W. F. Consequences of adsorbate-adsorbate interactions for apparent kinetics of surface catalytic reactions. *J. Catal.* **2022**, *405*, 410–418.

12. Matera, S., Meskine, H. & Reuter, K. Adlayer inhomogeneity without lateral interactions: rationalizing correlation effects in CO oxidation at RuO_2(110) with first-principles kinetic Monte Carlo. *J. Chem. Phys.* **2011**, *134*, 064713.

13. Hess, F. & Over, H. Rate-Determining Step or Rate-Determining Configuration? The Deacon Reaction over RuO_2(110) Studied by DFT-Based KMC Simulations. *ACS Catal.* **2017**, *7*, 128–138.

14. Liu, D.-J., Zahariev, F., Gordon, M. S. & Evans, J. W. Predictive Beyond-Mean-Field Rate Equations for Multisite Lattice–Gas Models of Catalytic Surface Reactions: CO Oxidation on Pd (100). *The Journal of Physical Chemistry C.* **2016**, *120* 28639–28653.

15. Pineda, M. & Stamatakis, M. Beyond mean-field approximations for accurate and computationally efficient models of on-lattice chemical kinetics. *J. Chem. Phys.* **2017**, *147*,

024105.

16. Hess, F. Efficient implementation of cluster expansion models in surface kinetic Monte Carlo simulations with lateral interactions: Subtraction schemes, supersites, and the supercluster contraction. *J. Comput. Chem.* **2019,** *40,* 2664–2676.

17. Kitchin, J. R. Machine learning in catalysis. *Nat. Catal.* **2018**, *1*, 230–232.

18. Schlexer Lamoureux, P. *et al.* Machine learning for computational heterogeneous catalysis. *ChemCatChem* **2019**, *11*, 3581–3601.

19. Miller, S. D. & Kitchin, J. R. Relating the coverage dependence of oxygen adsorption on Au and Pt fcc(111) surfaces through adsorbate-induced surface electronic structure effects. *Surf. Sci.* **2009**, *603*, 794–801.

20. Grabow, L. C., Hvolbæk, B. & Nørskov, J. K. Understanding Trends in Catalytic Activity: The Effect of Adsorbate–Adsorbate Interactions for CO Oxidation Over Transition Metals. *Top. Catal.* **2010**, *53*, 298–310.

21. Getman, R. B. & Schneider, W. F. DFT-based coverage-dependent model of pt-catalyzed NO oxidation. *ChemCatChem.* **2010**, *2*, 1450–1460.

22. Xu, Z. & Kitchin, J. R. Probing the Coverage Dependence of Site and Adsorbate Configurational Correlations on (111) Surfaces of Late Transition Metals. *J. Phys. Chem. C* **2014,** *118*, 25597–25602.

23. Liu, H., Liu, J. & Yang, B. Modeling the effect of surface CO coverage on the electrocatalytic reduction of CO_2 to CO on Pd surfaces. *Phys. Chem. Chem. Phys.* **2019**, *21* 9876–9882.

24. Yang, N. *et al.* Intrinsic Selectivity and Structure Sensitivity of Rhodium Catalysts for $C_{(2+)}$ Oxygenate Production. *J. Am. Chem. Soc.* **2016**, *138*, 3705–3714.

25. Ding, Y., Xu, Y., Song, Y., Guo, C. & Hu, P. Quantitative Studies of the Coverage Effects on Microkinetic Simulations for NO Oxidation on Pt(111). *J. Phys. Chem. C* **2019**, *123*, 27594–27602.

26. Wu, C., Schmidt, D. J., Wolverton, C. & Schneider, W. F. Accurate coverage-dependence incorporated into first-principles kinetic models: Catalytic NO oxidation on Pt (111). *J. Catal.* **2012**, *286*, 88–94.

27. Van de Walle, A. & Ceder, G. Automating first-principles phase diagram calculations. *J. Phase Equilib. Diffus.* **2002**, *23*, 348.

28. Lerch, D., Wieckhorst, O., Hart, G. L. W., Forcade, R. W. & Müller, S. UNCLE: a code for constructing cluster expansions for arbitrary lattices with minimal user-input. *Modell. Simul. Mater. Sci. Eng.* **2009**, *17*, 055003.

29. Nielsen, J., d'Avezac, M., Hetherington, J. & Stamatakis, M. Parallel kinetic Monte Carlo simulation framework incorporating accurate models of adsorbate lateral interactions. *J. Chem. Phys.* **2013**, *139*, 224706.

30. Ångqvist, M. *et al.* ICET – A Python Library for Constructing and Sampling Alloy Cluster Expansions. *Advanced Theory and Simulations*. **2019**, *2* 1900015.

31. Frey, K., Schmidt, D. J., Wolverton, C. & Schneider, W. F. Implications of

coverage-dependent O adsorption for catalytic NO oxidation on the late transition metals. *Catalysis Science & Technology* **2014**, *4*, 4356–4365.

32. Schmidt, D. J., Chen, W., Wolverton, C. & Schneider, W. F. Performance of cluster expansions of coverage-dependent adsorption of atomic oxygen on Pt (111). *J. Chem. Theory Comput.* **2012**, *8*, 264–273.

33. Bajpai, A., Frey, K. & Schneider, W. F. Binary Approach to Ternary Cluster Expansions: NO–O–Vacancy System on Pt (111). *The Journal of Physical Chemistry C* **2017**, *121* 7344–7354.

34. Hensley, A. J. R., Collinge, G., Wang, Y. & McEwen, J.-S. Coverage-dependent adsorption of hydrogen on Fe(100): Determining catalytically relevant surface structures via lattice gas models. *J. Phys. Chem. C Nanomater. Interfaces* **2020**, *124*, 7254–7266.

35. Li, X. & Grabow, L. C. Evaluating the benefits of kinetic Monte Carlo and microkinetic modeling for catalyst design studies in the presence of lateral interactions. *Catal. Today*. **2021** doi:10.1016/j.cattod.2021.03.010.

36. Kikuchi, R. A Theory of Cooperative Phenomena. *Phys. Rev.* **1951**, *81*, 988–1003.

37. Sanchez, J. M., Ducastelle, F. & Gratias, D. Generalized cluster description of multicomponent systems. *Physica A: Statistical Mechanics and its Applications* **1984**, *128*, 334–350.

38. Sanchez, J. M. Cluster expansion and the configurational theory of alloys. *Phys. Rev. B Condens. Matter* **2010,** *81*, 224202.

39. Blum, V., Hart, G. L. W., Walorski, M. J. & Zunger, A. Using genetic algorithms to map first-principles results to model Hamiltonians: Application to the generalized Ising model for alloys. *Phys. Rev. B Condens. Matter* **2005**, *72*, 165113.

40. Chen, W., Dalach, P., Schneider, W. F. & Wolverton, C. Interplay between Subsurface Ordering, Surface Segregation, and Adsorption on Pt–Ti (111) Near-Surface Alloys. *Langmuir* **2012**, *28*, 4683–4693.

41. Herder, L. M., Bray, J. M. & Schneider, W. F. Comparison of cluster expansion fitting algorithms for interactions at surfaces. *Surf. Sci.* **2015,** *640*, 104–111.

42. Miller, S. D. & Kitchin, J. R. Uncertainty and figure selection for DFT based cluster expansions for oxygen adsorption on Au and Pt (111) surfaces. *Mol. Simul.* **2009,** *35*, 920–927.

43. Vignola, E. *et al.* A machine learning approach to graph-theoretical cluster expansions of the energy of adsorbate layers. *J. Chem. Phys.* **2017**, *147*, 054106.

44. Mueller, T. & Ceder, G. Bayesian approach to cluster expansions. *Phys. Rev. B Condens. Matter* **2009**, *80*, 024103.

45. Cockayne, E. & van de Walle, A. Building effective models from sparse but precise data: Application to an alloy cluster expansion model. *Phys. Rev. B Condens. Matter* **2010**, *81*, 012104.

46. Mueller, T. Ab initio determination of structure-property relationships in alloy nanoparticles. *Phys. Rev. B Condens. Matter* **2012**, *86*, 144201.

47. Bray, J. M., Smith, J. L. & Schneider, W. F. Coverage-Dependent Adsorption at a Low Symmetry Surface: DFT and Statistical Analysis of Oxygen Chemistry on Kinked Pt (321). *Topics in Catalysis*. **2014**, 57 89–105.

48. Bray, J. M. & Schneider, W. F. First-Principles Analysis of Structure Sensitivity in NO Oxidation on Pt. *ACS Catal.* **2015**, *5*, 1087–1099.

49. Cao, L. & Mueller, T. Rational Design of Pt3Ni Surface Structures for the Oxygen Reduction Reaction. *J. Phys. Chem. C* **2015**, *119*, 17735–17747.

50. Ma, X., Li, Z., Achenie, L. E. K. & Xin, H. Machine-Learning-Augmented Chemisorption Model for CO2 Electroreduction Catalyst Screening. *J. Phys. Chem. Lett.* **2015**, *6*, 3528–3533.

51. Liu, F., Yang, S. & Medford, A. J. Scalable approach to high coverages on oxides via iterative training of a machine-learning algorithm. *ChemCatChem* **2020,** *12*, 4317–4330.

52. Boes, J. R. & Kitchin, J. R. Neural network predictions of oxygen interactions on a dynamic Pd surface. *Mol. Simul.* **2017,** *3*, 346–354.

53. Shao, J., Wang, Q. & Liu, F. Learning to Sample: an Active Learning Framework. *arXiv [cs.LG]*. **2019.**

54. Tran, K. *et al.* Methods for comparing uncertainty quantifications for material property predictions. *Mach. Learn.: Sci. Technol.* **2020**, *1*, 025006.

55. Hoffmann, M. J., Medford, A. J. & Bligaard, T. Framework for Scalable Adsorbate–Adsorbate Interaction Models. *J. Phys. Chem. C* **2016**, *120*, 13087–13094.

56. İnoğlu, N. & Kitchin, J. R. Simple model explaining and predicting coverage-dependent atomic adsorption energies on transition metal surfaces. *Phys. Rev. B Condens. Matter* **2010**, *82*, 045414.

57. Wang, S.-H., Pillai, H. S., Wang, S., Achenie, L. E. K. & Xin, H. Infusing theory into deep learning for interpretable reactivity prediction. *Nat. Commun.* **2021**, *12*, 5288.

58. Lei, X. & Medford, A. J. A Universal Framework for Featurization of Atomistic Systems. *arXiv [physics.chem-ph]*. **2021**.

59. Wang, S., Pillai, H. S. & Xin, H. Bayesian learning of chemisorption for bridging the complexity of electronic descriptors. *Nat. Commun.* **2020,** *11*, 6132.